Structure and electrical response of GaAs nanowires

Looking for a correlation at the nano-scale

DISSERTATION
zur Erlangung des Grades eines Doktors
der Naturwissenschaften

vorgelegt von
M. Sc. Genziana Bussone-Grifone (geb. Bussone)

eingereicht bei der Naturwissenschaftlich-Technischen Fakultät
der Universität Siegen

Siegen 2014

Gutachter:

Prof. Dr. Dr. Ullrich Pietsch

Prof. Dr. Julian Stangl

Co-Betreuer:

Dr. habil. Tobias Schülli

Tag der mündlichen Prüfung:

06. Februar 2015

Gedruckt auf alterungsbestigem holz- und sefreiem Papier.

To my father Massimo

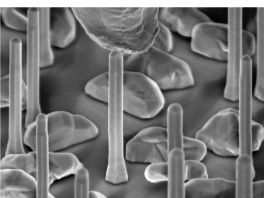

Abstract

For applications of nanowires in optoelectronic devices their controlled positioning onto substrates during growth is often required, as well as the control of their polytype mixture and strain state. Therefore a deep comprehension of the growth and preparation mechanisms is essential. Multiple investigation techniques at the nano-scale have been developed nowadays with the goal to correlate the structure and the physical response of nanostructures.

The first aim of this work is the structural investigation of *individual* nanowires grown on GaAs substrates by *molecular beam epitaxy*. The specific positioning of the nanowires during growth has been achieved by Au-implantation into the substrate. X-ray nano-diffraction in *grazing incidence diffraction* geometry was used to investigate the in-plane strain at different positions, along the growth axis of individual nanowires. It was found that the nanowires are twisted about their growth axis with respect to the substrate. As expected, the crystal lattice of the nanowires is totally relaxed. Under surface diffraction conditions, the upper most layers of the growth substrate could be investigated at the same time. Here, regions at different distances from the Au-implanted area revealed the presence of a compressive strain, decreasing further away from the nanowire base.

In prior studies of semiconductor nanowires it has been shown that the value of specific physical parameters strongly differ from bulk materials. For example, the high aspect ratio and the mixture of polytypes can significantly influence electrical and optical properties of GaAs nanowires. Moreover, nanowires standing in upright position onto their growth substrate revealed their importance in modern devices. The second aim of this thesis is to correlate the electrical and structural parameters of *individual as-grown* nanowires onto their growth substrate. This was achieved by measuring the electrical characteristics of single nanowires in a *focused ion beam* chamber; and by determining their polytype composition using coplanar X-ray nano-diffraction. The nanowires measured showed differing electrical

characteristics. These differences have been successfully correlated with the number of zinc-blende and twinned zinc-blende units detected within single nanowires. The combination of the described techniques represents the main challenge of this work. Besides the difficulties of identifying individual nanowires in different experimental configurations; all electrical characteristics, linked to the contacting procedure of the nanowire, had to be understood and controlled.

Electronic and optoelectronic applications often require specific sample preparations. Those may include the embedding of the nanostructures in a *polymer matrix* and the application of a top contact. As a third aim, symmetric and asymmetric X-ray diffraction revealed indirectly the presence of a preparation-induced average initial strain in the Benzocyclobutene polymer, by measuring an ensemble of embedded GaAs nanowires. This resulted in uniaxial strained embedded nanostructures, and was found to originate from the thermal processing of the polymer. The detected compression was shown to decrease under X-ray illumination and application of an external static electric field, which lead to the formation and reorientation of polar sub-molecules in the polymer.

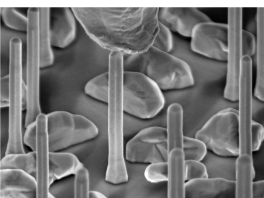

Zusammenfassung

Um Nanodrähte gezielt für optoelektronische Schaltungen anzuwenden, muss bereits beim Wachstum auf deren genaue Positionierung auf dem Substrat, auf die Polytype Verteilung im Nanodraht und auf dessen Verzerrungszustand geachtet werden. Deshalb ist ein tieferes Verständis der Wachstums und Präparationsmechanismen erforderlich. Der Einsatz einer Reihe von Untersuchungstechniken auf der Nanosskala wurden entwickelt, um physikalische Eigenschaften der Nanoobjekte mit deren Struktur zu korrelieren.

Das erste Ziel der vorliegenden Arbeit liegt daher in der strukturellen Untersuchung *einzelner*, mittels *Molekular Strahl Epitaxie* auf GaAs Substraten gewachsener, Nanodrähte. In diesem Fall wurde die Positionierung der Drähte über eine räumlich selektive Implantation von Gold Atomen im Substrat erreicht. Röntgenbeugung unter streifendem Einfall mittels eines Nanostrahls wurde eingesetzt, um den Verzerrungszustand in der Substratebene an verschiedenen Positionen auf dem Substrat und entlang des Drahtes zu bestimmen. Dabei wurde festgestellt, dass die Nanodrähte entlang der Wachstumsrichtung leicht verdreht gegenüber dem Substrat wachsen. Wie erwartet ist dabei das Kristallgitter der Nanodrähte verzerrungsfrei. Infolge der extremen Oberflächensensitivität konnten gleichzeitig die obersten Gitterebenen des Substrats untersucht werden. Hierbei zeigte sich eine mit größer werdendem Abstand zum Au implantierten Gebiet kleiner werdende kompressible Deformation.

Aus früheren Untersuchungen an Halbleiter Nanodrähten ist bekannt, dass die Größe vieler physikalischer Eigenschaften von der des Volumenmaterials abweicht. Zum Beispiel beeinflußt das große Seitenverhältnis und die strukturelle Mischung verschiedener Polytypen signifikant die elektrischen und optischen Eigenschaften von GaAs Nanodrähten. Weiterhin spielt die Tatsache, dass die Drähte in aufrechter Position auf dem Substrate verbleiben können, eine große Rolle für deren Anwendung in modernen Bauelementen. Das zweite Ziel dieser Arbeit besteht in der Korrelation von elektrischen und strukturellen Eigenschaften *einzelner* Nanodrähte *in*

ihrer Position auf dem Substrat. Diese Korrelation wurde erreicht, indem die elektrische Charakteristik ausgewählter Nanodrähte in einer *Fokussierten Ionenstrahl* Kammer gemessen und die Polytypzusammensetzung der gleichen Drähte mittels Röntgennanodiffraktion bestimmt wurde. Die gemessenen Nanodrähte zeigen eine unterschiedliche elektrische Charakteristik. Diese Unterschiede konnten erfolgreich mit der unterschiedlichen Zahl von Zinkblende und verzwillingter Zinkblende Struktureinheiten innerhalb der Nanodrähte korreliert werden. Die Kombination dieser beiden Techniken stellte die größte Herausforderung dieser Arbeit dar. Neben der Schwierigkeit der Identifizierung individueller Nanodrähte in unterschiedlichen experimentellen Konfigurationen, mußten die Einflußparameter der elektrischen Charakteristik, einschießlich der Kontaktierungsprobleme, verstanden und kontrolliert werden.
Elektronische und optoelektronische Anwednungen fordern sehr oft eine spezielle Probenpräparation. Das schließt die Einbettung von Nanostrukturen in eine *Polymermatrix* und die Kontaktierung derselben mit ein. Als drittes Ziel dieser Arbeit wurde mit Hilfe der symmetrischen und asymmetrischen Röntgenbeugung nachgewiesen, dass Benzocyclobutene im Resultat des Einbettungsprozesses gegenüber dem eingebetteten GaAs Nanodrähten elastisch verzerrt ist. Das Auftreten dieser einachsig deformierten eingebetten Nanostruktur wurde auf den thermischen Prozessschritt bei der Einbettung zurückgeführt. Es zeigte sich, dass die festgestellte Kompression unter Bestrahlung mit Röntgenlicht und bei gleichzeitig angelegtem elektrischen Feld zurückging. Dieser Effekt konnte mit der Formierung und Reoriertierung von polaren Sub-Molekülen im Polymer erklärt werden.

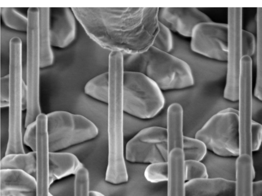

Contents

Abstract (English/Deutsch) **v**

Contents **xi**

Acronyms **xiii**

List of figures **xviii**

List of tables **xix**

1 Introduction **1**

2 GaAs nanowires **7**

2.1 Crystal structure of GaAs nanowires 7

2.1.1 Structural polytypisms: wurtzite in GaAs 8

2.2 MBE growth and details on VLS growth mechanism 9

2.2.1 Polytype growth selection 11

2.3 Physics at the nano-scale 12

2.3.1 Characterization at the nano-scale 13

2.3.2 Electrical and optical properties: the band structure 14

2.3.3 Thermal properties 16

2.4 Applications 17

2.4.1 Electronic, photonic and optoelectronic applications 17

2.4.2 Piezo-electric applications 21

2.5 Selected techniques for structural characterizations 21

3 X-ray kinematic diffraction and synchrotron radiation **25**

3.1 Reciprocal lattice and crystal planes . . . 25

3.2 Basics of X-ray kinematic diffraction . . . 27

3.2.1 Signals from nanostructures in reciprocal space . . . 29

3.3 A synchrotron beamline: ESRF-ID01 . . . 31

3.4 Diffraction geometries . . . 33

3.4.1 Coplanar symmetric and asymmetric geometries . . . 33

3.4.2 Non coplanar grazing incidence geometry . . . 34

3.4.3 Maps in reciprocal space . . . 36

3.4.4 Specific sample configuration in the diffraction from a single nanowire 36

4 Grazing incidence X-ray diffraction of single GaAs nanowires **39**

4.1 Probing the in-plane strain in single GaAs nanowires . . . 39

4.2 GaAs nanowires at locations defined by focused-ion beams . . . 40

4.3 The details about the experimental configuration . . . 42

4.4 Determination of the in-plane strain . . . 44

4.5 Summary . . . 46

5 Correlation of electrical and structural properties in single GaAs nanowires **49**

5.1 Electrical measurement: the first attempts with an AFM . . . 49

5.2 The electrical and structural characterization of the same nanowire: samples and methods . . . 51

5.3 The electrical characterization: theory and models . . . 52

5.3.1 Contacts to a single nanowire . . . 52

5.3.2 Multiple regimes in a NW characteristic . . . 53

5.3.3 Thermoionic emission theory and Schottky model . . . 55

5.4 Back-to-back Schottky model: the data analysis (method A) . . . 58

5.5 Space Charge Limited Current model: the data analysis (method B) . . . 64

5.6 Total series resistance, effective mobility and charge carrier density . . . 65

5.7 The structural characterization . . . 66

5.7.1 The effect of the tip contact on the NW structure . . . 68

5.8 The correlation . . . 71
5.9 Discussion on the present results and summary . . . 72
5.10 The last attempts with STM . . . 73

6 Strain impact of BCB polymer curing on embedded semiconductor nanostructures 77
6.1 BCB, an organic polymer for the planarization of nanostructures . . . 77
6.2 Samples and experimental method . . . 78
6.3 Elastic strain inherent to the thermal history of the fabrication method . . . 80
6.4 Thermal expansion coefficients and polymer curing: the FEM simulation . . . 82
6.5 Application of an external static electric field . . . 84
6.6 Summary . . . 86

7 Conclusions 87

Acknowledgements 105

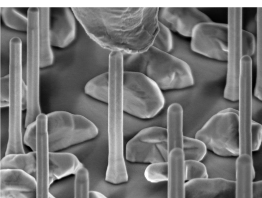

Acronyms

μ-PL Micro-Photoluminescence

AFM Atomic Force Microscopy

BCB Benzocyclobutene

CTR Crystal Truncation Rod

CVD Chemical Vapor Deposition

DFT Density Functional Theory

EDS Energy Dispersive X-ray Spectroscopy

ESRF European Synchrotron Research Facility

fcc face centered cubic

FE Field Emission theory

FEM Finite Element Modelling

FIB Focused Ion Beam

FWHM full width at half maximum

FZP Fresnel Zone Plate

GID Grazing Incidence Diffraction

HRTEM High Resolution Transmission Electron Microscopy

JFET Junction gate Field-Effect Transistor

K-map quicK-mapping

LINAC Linear Accelerator

MBE Molecular Beam Epitaxy

MESFET Metal-Semiconductor Field-Effect Transistor

MISFET Metal–Insulation–Semiconductor Field-Effect Transistor

MOSFET Metal-Oxide-Semiconductor Field Effect Transistor

MS metal/semiconductor

MUSST Multipurpose Unit for Synchronisation, Sequencing and Triggering

n-XRD X-ray nano-Diffraction

NW nanowire

OSA Order Sorting Aperture

PCB Printed Circuit Board

PL Photoluminescence

PMMA poly(methyl) methacrylate

RSM Reciprocal Space Map

RT Room Temperature

SCLC Space Charge Limited Current

SEM Scanning Electron Microscopy

SF stacking fault

SPM Scanning Probe Microscopy

SRIM The Stopping and Range of Ions in Matter

SSL Surface Science Laboratory

STM Scanning Tunneling Microscopy

TEM Transmission Electron Microscopy

TF tuning fork

TFE Thermoionic Field Emission theory

TFLC Trap Filled Limited Conduction

TZB twinned zinc-blende

V-I Voltage-Current

VLS Vapor-Liquid-Solid

VS Vapor-Solid

WZ wurtzite

XEOL X-ray Excited Optical Luminescence

XRD X-ray Diffraction

XRF X-ray Fluorescence

ZB zinc-blende

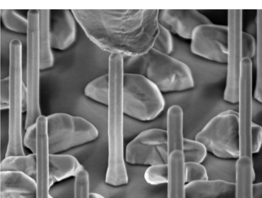

List of Figures

2.1 Zinc-blende and wurtzite unit cells. 8
2.2 Atomic closed packed layers. 9
2.3 Au-assisted and self-assisted MBE growth. 11
2.4 Selected techniques for structural characterization. 23

3.1 ID01 diffractometer. 30
3.2 The nano-focus setup available at beamline ID01 (ESRF). 33
3.3 Coplanar symmetric and asymmetric geometries. 34
3.4 Non coplanar GID geometry. 35
3.5 Radial and transverse scan in XRD on a single NW. 36

4.1 SEM image of a single NW and the sample surface. 41
4.2 TEM image of the atomic stacking in a single NW. 42
4.3 K-map of a line of NWs. 43
4.4 GID reciprocal space maps of a single NW. 44
4.5 Intensity profiles in GID geometry. 47

5.1 Comparison of an AFM and SEM image of two NWs on the same samples, collected before the electrical characterization. 50
5.2 A SEM image and a sketch of the contacted nanowire. 52
5.3 Log-log plot of one V-I curve. 55
5.4 Sketch of the back-to-back diode band configuration. 59
5.5 Voltage-Current characteristics of several NWs. 60
5.6 Back-to-back Schottky diode model: the fit. 61
5.7 Modelled electrical characteristics for different sizes of the bottom contact. . . 63

5.8 Simulated V-I curve with SCLC model. 65
5.9 The dispersion graph of R_s as a function of the effective μ. 66
5.10 3D reciprocal space map of a NW for reflection (331). 67
5.11 Phase structure of NW3. 70
5.12 3D reciprocal space map of a NW for reflection (422). 71
5.13 Correlation of the electrical and structural parameters. 72
5.14 V-I curves collected with STM and in a FIB chamber. 74

6.1 SEM image of embedded GaAs NWs. 78
6.2 Teflon sample holder. 80
6.3 Comparison of reciprocal space intensity maps. 81
6.4 Strain values extracted from the X-ray diffraction data in three different areas on the sample. 82
6.5 Strain distribution, along the growth axis of the NW, obtained by FEM simulations. 84
6.6 GaAs NWs emerging from the BCB polymer layer and the metal contact. 85
6.7 Application of a static electric field under X-ray illumination. 86

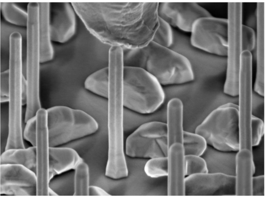

List of Tables

5.1 Electrical parameters. 65
5.2 Structural parameters. 69

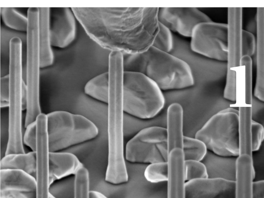

1 Introduction

Among III-V semiconducting compounds, direct band-gap GaAs has a high potential for modern optoelectronic applications. Compared to common thin film technologies, the growth and integration of GaAs nanowires (NWs) in real devices [155, 146, 28, 61] has proven to be very advantageous [20]. This is due to the exceptional physical response of nanowires in terms of mechanical, elastic, electrical, optical and many other properties. They are related to the high aspect ratio, the shape and size, and the composition of the structural *polytypes*, which have an impact on the configuration of the semiconductor band structure, and consequently on their characteristic physical properties. The typical geometry of NWs makes them suitable candidates for integration on Si and Ge substrates, where the mismatch of lattice constants is reduced by elastic strain relaxation at the interface substrate/nanowire, enhanced compared to thin films [20]. The structure of the nanowires depends strongly on the growth and preparation methods. A common growth method is Molecular Beam Epitaxy (MBE) in metal catalysed [149] or self-assisted [29] configurations. Integration into real devices often requires a control of the position and size of the nanowires on the substrate. In addition, specific sample preparation, such as the embedding of the NWs in a polymer matrix [80] and the application of metal contacts is essential. This implies a full understanding of the growth and preparation mechanisms, which are still open questions.

The combination of different characterization techniques, to probe both the structure and the physical response at the nano-scale, is crucial for understanding the origin of the outstanding

properties of the NWs.

A large variety of structural characterization techniques is available nowadays, among them X-ray Diffraction (XRD), which has proved very useful for the investigation of nano-objects without removal from their substrate. XRD reveals the composition and the strain state of ensemble of nanowires, where the use of broad beams (>100 μm scale) provides average properties over a larger area of the samples under analysis. The availability of sub-micron-sized X-ray beams at synchrotron facilities opened up the investigation of objects at the nano-scale [39]. This allows the identification of the exact crystal structure and strain state in single nanowires [12].
Techniques such as nano-indentation [52] and bending and tensile tests are applied in the investigation of the elastic, plastic and mechanical properties of single NWs [22] and micro-sized objects [76], using Atomic Force Microscopy (AFM) or specifically-designed clamping devices. Several studies relate the structural composition and size with optical and electrical responses in both ensemble [138] and single nano-objects. In the literature, the optical response has been probed in single NWs using for example Micro-Photoluminescence (μ-PL), X-ray Excited Optical Luminescence (XEOL) [99] and Raman Spectroscopy [91]. The different electrical responses of single as-grown NWs were correlated by Timm [145] and Talin [143] with the sizes of the diameters, using micro-contacting in a Scanning Tunneling Microscopy (STM) and a Focused Ion Beam (FIB) chamber, respectively.

The first aim of this thesis was to investigate the structure of GaAs nanowires in their growth position on the substrate using X-ray diffraction, in order to determine the crystalline quality and their strain state originating from the growth and/or the sample preparation. The structure of single nanowires was characterized with a nano-focused beam of synchrotron radiation in order to determine their out-of-plane and in-plane strain states and their polytype composition. The second aim was to investigate the electrical response of single selected nanowires and correlate the observed differences with their structural composition. Here, the investigation of the electrical response and the structural composition *of the same* as-grown nanowire constituted a remarkable challenge.

The thesis is organized in seven chapters. After the Introduction, Chapter 2 treats the main applications of GaAs semiconducting nanowires, with particular attention paid to the electrical properties, and describes the MBE growth technique. Chapter 3 presents the principles of the kinematical theory of X-ray diffraction, together with the experimental technique and geometries used, and a description of the experimental apparatus. Chapter 4 describes the investigation of the in-plane strain in single GaAs nanowires on their growth substrate in non-coplanar Grazing Incidence Diffraction (GID) geometry. The implantation of Au in the GaAs substrate with a FIB was confirmed to be an effective method for defining the position of single nanowires. The in-plane strain state was probed for the first time in X-ray nano-Diffraction (n-XRD) in non-coplanar GID geometry. The technique made the identification of single NWs in the unstrained condition possible, and allowed quantification of the strain state affecting the growth substrate due to the metal implantation. Chapter 5 describes the characterization of electrical and structural properties of single GaAs nanowires and provides their correlation. N-XRD in asymmetric coplanar geometry allowed the measurement of the structural composition of GaAs nanowires grown on a Si substrate pre-patterned by e-beam lithography. Those measurements revealed the presence of vertically stacked units of pure zinc-blende and twinned zinc-blende structures, the numbers of which have been compared with the electrical response measured for the same single NWs. Chapter 6 reports the strain state of ensemble nanowires embedded in a Benzocyclobutene (BCB) matrix, related to the thermal processing of the polymer layer. The result presented was obtained after a specific sample preparation, performed to contact the ensemble NWs, with the initial aim of measuring the piezo-electric response to an applied static electric field. The result shows the influence that the sample manipulation and contacting can have on the actual performance of real devices.

The results are then summarized in chapter 7.

Published manuscripts

Most of the results (text and figures) presented in this thesis have been published in separate scientific manuscripts, which are listed here.

G. Bussone, R. Schott, A. Biermanns, A. Davydok, D. Reuter, G. Carbone, T. U. Schülli, A. D. Wieck and U. Pietsch.
Grazing-incidence X-ray diffraction of single GaAs nanowires at locations defined by focused ion beams.
Journal of Applied Crystallography, 46:887, 2013.

in chapter 4;

G. Bussone, H. Schäfer-Eberwein, E. Dimakis, A. Biermanns, D. Carbone, A. Tahraoui, L. Geelhaar, P. Haring Bolívar, T. U. Schülli and U. Pietsch.
Correlation of electrical and structural properties of single as-grown GaAs nanowires on Si (111) substrates.
Nano Letters, 15(2):981, 2015.

in chapter 5;

G. Bussone, E. Dimakis, R. Grifone, A. Biermanns, A. Tahraoui, D. Carbone, L. Geelhaar, T. U. Schülli and U. Pietsch.
Impact of strain induced by polymer curing in benzocyclobutene embedded semiconductor nanostructures.
Physica Status Solidi RRL, 8(12):1007, 2014.

in chapter 6.

Other publications are:

C. Somaschini, A. Biermanns, S. Bietti, **G. Bussone**, A. Trampert, S. Sanguinetti, H. Riechert, U. Pietsch and L. Geelhaar.
Axial InAs/GaAs heterostructures on silicon in a nanowire geometry.
Nanotechnology, 25(48):485602, 2014.

D. Carbone, A. Pateras, **G. Bussone**, P. G. Evans, T. Cornelius, M. Bousquet, A. Boulle, B. Gautier, J.-R. Duclere.
Structural observation of piezoelectric inhomogeneity in a mixed-orientation $Na_{0.5}Bi_{0.5}TiO_3$ perovskite thin film.
Applied Physics Letters, 105:242901, 2014.

A. Biermanns, T. Rieger, **G. Bussone**, U. Pietsch D. Grützmacher and M. I. Lepsa.
Axial strain in GaAs/InAs core-shell nanowires.
Applied Physics Letters, 102:043109, 2013.

G. Bussone, T. A. Lafford, F. Masiello, A. Gibaud, G. Carbone, T. U. Schülli, S. H. Connell, A. Vivo Rommeveaux, M. Wormington and J. Härtwig.
Investigation of surface and sub-surface damage in high quality synthetic diamonds by X-ray reflectivity and grazing incidence in-plane diffraction.
Physica Status Solidi A, 208(11):2612, 2011.

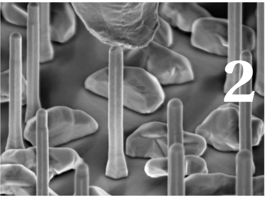

2 GaAs nanowires

In chapter 2, the crystal structure of GaAs nanowires is described, together with the MBE technique, which allows the growth of GaAs NWs. Furthermore, attention is given to the physics of GaAs at the nanoscale: how and why the properties do change if the size of the object lies in the sub-micron scale? The fields of application of semiconductor nanowires are presented, with examples of existing devices and with particular attention to those based on GaAs. In the end, the methodical background of diverse structural characterization techniques, such as Transmission Electron Microscopy (TEM), Atomic Force Microscopy (AFM), Scanning Tunneling Microscopy (STM) and Scanning Electron Microscopy (SEM), is described.

2.1 Crystal structure of GaAs nanowires

GaAs (symmetry group F43m) belongs to the group of III-V semiconductors. Bulk GaAs has zinc-blende (ZB) structure; which is formed by covalent bonded Ga and As atoms, arranged in two face centered cubic (fcc) cells, translated by one quarter of the cube diagonal along the [111] direction. The cubic lattice parameters [94] are $a_{cubic} = b_{cubic} = c_{cubic} = 5.65$ Å with $\alpha = \beta = \gamma = 90°$. In addition, a hexagonal structure can be introduced to describe the atomic stacking, where the lattice parameters are $a_{hexagonal} = 3.99$ Å and $c_{hexagonal} = 9.79$ Å [94]. In GaAs nanowires the crystal structure adopts other atomic configurations, known as polytypes.

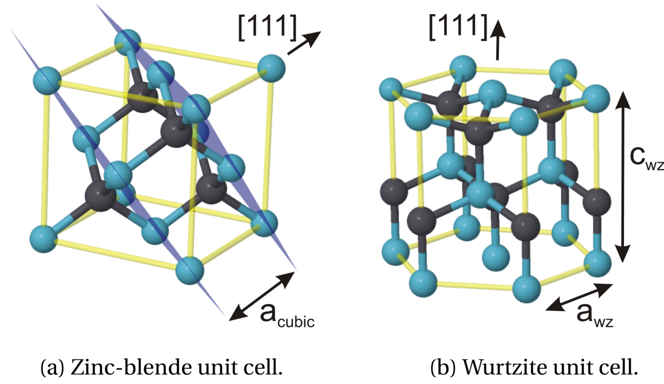

(a) Zinc-blende unit cell. (b) Wurtzite unit cell.

Figure 2.1: Ga atoms (in black) and As atoms (in blue) are visible in the cubic ZB (a) and the hexagonal WZ (b) unit cells.

2.1.1 Structural polytypisms: wurtzite in GaAs

In semiconductor NWs growth along [111] direction, *polytypes* (or *crystal phases*) with the same in-plane structure but different stacking sequences with respect to bulk are quite often observed. Several polytypisms have been observed in III-V semiconductor NWs [79], and among them the cubic zinc-blende and the hexagonal wurtzite (WZ) and 4H structure are well known. The GaAs ZB and WZ unit cells are shown in Figure 2.1. ZB, 4H and WZ have different stacking sequence along the growth direction: ABCABC, ABCBABCB and ABABAB, respectively; where the A, B and C planes (figure 2.2) are constituted by bilayers of Ga and As atoms. Kriegner [79] observed in InAs and InSb NWs that the presence of hexagonal bilayers increases the interplanar distance of the layers along the [111] growth axis (~ 0.25% for InAs), and reduces the in-plane lattice distance (~ 0.12% for InAs) compared to ZB. In addition, he found a linear proportionality between the changes in lattice parameter and the fraction of hexagonal bilayers within the unit cell [116], named *hexagonality* of the polytype. According to this definition, ZB, 4H and WZ have an hexagonality of 0%, 50% and 100%, respectively. During the growth, *stacking faults* and *rotational twins* may form. In particular, a rotational twin is observed when the ZB stacking is mirrored at a *twin boundary* along the growth direction. The resulting twinned zinc-blende (TZB) structure differs in azimuth angle by 180° with respect to ZB. This leads to the stacking ABC**ABA**CBA. In the specific case of this thesis, GaAs nanowires may crystallize either in the cubic ZB and the TZB structure, or in the hexagonal WZ phase [96].

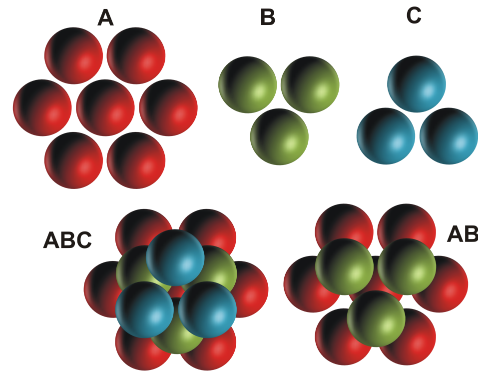

Figure 2.2: Top view of atomic *closed packed* layers (A, B and C) stacked along the [111] direction as ABC and AB.

2.2 MBE growth and details on VLS growth mechanism

Semiconductor and metallic nanowires can be obtained both via top-down etching or bottom up approach. The latter makes use of common epitaxial growth techniques, such as Chemical Vapor Deposition (CVD) and Molecular Beam Epitaxy (MBE), which allow a good control of the crystalline structure. MBE is one of the most common growth methods for III-V semiconductor NWs. Here, the MBE growth will be presented, as the technique used for growing all the GaAs NW samples measured and presented in this thesis. The typical fabrication methods for NWs are the catalyst-assisted [149] and the self-assisted methods [29] (Figure 2.3).

In the first case, the NWs are grown using a catalyst material (such as metals, in particular Au). The growth elements, Ga and As, supplied in the vapour phase are diluted in a liquid Au droplet and grow as solid GaAs at its bottom. Therefore, this growth mode is named Vapor-Liquid-Solid (VLS) mechanism. In more detail, the method makes use of a pre-deposited thin Au film, forming liquid droplets after annealing [57], which act as the preferable sites for the nucleation of the NW growth. The growth rate of the nanowires, together with the growth rate of parasitic islands on the substrate surface, is determined by the contributions of the evaporated material reaching directly the Au droplet or impinging on the substrate at non catalysed sites. In the latter case, the material reaches the top of the NW through diffusion along the side facets. The III-V NW growth is catalysed, because both the Ga and As components become over-saturated in the liquid droplet. At this point, the condensation of the vapour species and the precipitation of a solid phase at the particle-substrate interface takes place. In mononuclear

approximation [45], the nucleation process occurs at the boundary between the droplet and the NW top. This can start in two different positions: at the centre or close to the outer surface of the droplet (known as *triple phase line*). The diameter of the resulting NWs directly depends on the size of the catalyst droplet.

In the second case, the self-assisted growth, one constituent of the NW material replaces the foreign metal in the seed function. The growth takes place in presence of a liquid droplet of the group III element onto a SiO_2 layer, with thickness of tens of nm, previously deposited on the growth wafer. Natural or patterned pinholes in the oxide layer act as nucleation centres for the liquid droplet and interact with the reactive vapour component, resulting in the nucleation of the NWs growth.

The VLS mechanism, mentioned above, can be explained according to thermodynamics. Hereafter the leading concept is presented briefly. A phase transition takes place when the system tends towards the thermodynamic equilibrium through minimization of the total energy [147]. The Gibbs free energy

$$G^{\alpha}(p, T, N_a) \tag{2.1}$$

can be introduced for the element a and the phase α, in an *open* system which has an exchange of material and entropy with the environment. The term 2.1 shows a dependence on the pressure p, temperature T and number of moles N_a. The chemical potential μ_a^{α}, for element a in phase α, can be defined as

$$\mu_a^{\alpha}(p, T) = \frac{\partial G^{\alpha}(p, t, N_a)}{\partial N_a}. \tag{2.2}$$

The equilibrium is reached when the total Gibbs free energy is minimized with respect to the number of atoms of element a changing from phase α to another phase. This corresponds to equal chemical potentials for the elements and phases present in the system. The difference in chemical potentials is the driving force towards the equilibrium, as long as the mentioned condition is not satisfied. The same concept holds in complex systems, such as during the growth of GaAs nanowires. Here, the chemical potentials of the vapour, the substrate, the atoms on the substrate surface (adatoms), the liquid droplet and the NW itself, have to be

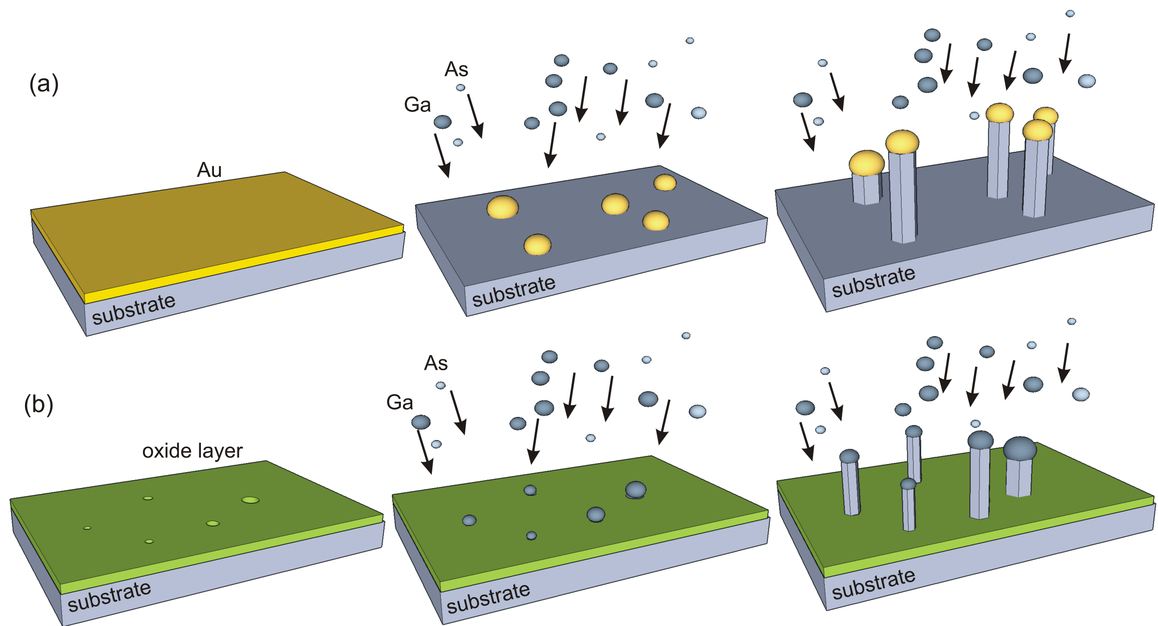

Figure 2.3: (a) Sketch of the Au-assisted MBE growth. A Au film is deposited on the substrate surface, and after annealing the formation of Au droplets takes place. The growth starts when Ga and As are supplied. (b) Sketch of the self-assisted MBE growth. In this case the growth takes place in presence of an oxide layer. When Ga and As are supplied, Ga droplets form in correspondence of natural or artificial pinholes in the oxide layer, and the NW growth takes place in those positions.

taken into account.

It has been shown in literature [4], that local fluctuations of the number of Ga and As atoms and the temperature during the growth may induce a change in the growth mechanism; and may lead to the Vapor-Solid (VS) regime. The latter takes place when the catalyst liquid droplet is consumed or replaced by a solid particle. It was observed that the orientation of the epitaxially grown nanowires (NWs) follows the [111] crystallographic direction, corresponding to the surface normal of (111) oriented substrates. The [111] direction is preferentially maintained in the NWs growth, also in the case of substrates with different surface orientation [138].

2.2.1 Polytype growth selection

NWs grown by MBE usually show a random crystallographic composition, where an intermixing of the two ZB and WZ polytypes is observed. Phase-pure NWs can be obtained under specific growth conditions only [81], but usually stacking faults and twin planes modify the

crystal structure [40]. Bonding arrangement and surface stoichiometry were found to play an important role in the phase transition between ZB and WZ. Indeed, in bulk the ZB polytype is favoured compared to WZ because of its lower cohesive energy ($\Delta E_{cohesive} = 24 meV$ per pair for GaAs [158]). This condition is modified in NWs, due to the high number of unsaturated bonds (or *dangling bonds*) at the NW surface. The content of ZB and WZ polytypes in NWs has been related to the contribution of the NW side facets to the total energy [88]. For hexagonal WZ bonding, there is an additional contribution to cohesive energy, increasing linearly with the diameter of the wire. In addition, surface orientation and passivation of dangling bonds turned out to be energetically significant comparing the WZ with the cubic stacking. On the other hand, in the Au assisted MBE growth of GaAs NWs on a GaAs substrate, Glas [51] observed the presence of ZB mainly during the initial stage and at the end of the NW growth. WZ appears when the supersaturation of Ga (and possibly As) is higher than the one of the transient sections of the growth. This leads to the switching between ZB and WZ polytypes. In the mentioned study, the inverse proportionality of the critical size of the nucleation sites with the supersaturation suggests a preferential WZ growth for small nuclei, as it takes place at the triple phase line. The growth of ZB and WZ depends on both the energy of the side facets forming in the NW and the contact angle of the liquid droplet. Theoretical studies [138, 33, 69] predict different electronic band structures for different crystal phases of the same material, which may cause band offset at the polytype interfaces. Therefore, the control of the polytype mixture is crucial to tune the structure [40], the strain state and consequently the physical properties of the grown NWs.

Growth parameters of III-V semiconductor NWs, such as temperature (normally ~ 870 K for GaAs), pressure and composite flux, play an important role in the growth process. Their precise control is required to obtain specific heterostructures [40]. Fluctuations of the mentioned parameters may be responsible for a change of the NWs diameter during the growth, often resulting in tapered structures.

2.3 Physics at the nano-scale

A few physical properties of semiconductor nanowires may differ from those known from bulk material. *What does make nanowires exceptional?* This is the motivation of present research

projects in nanoscience. Measurements have been extensively reported in literature [14] for a large variety of properties: ranging from mechanical, elastic and vibrational, to electrical and thermal properties. Due to the high aspect ratio of nanowires, the surface to volume ratio acquires great importance, as well as the size [90, 136] and shape of the object. As the surface constitutes a break of the perfect crystal order, it is rich of defects, which originate electronic states within the band gap of the material. This modifies the band structure; which is directly related to the electronic properties of semiconductors.

Furthermore, the band configuration is modified by the structural composition of the nanowires; for example, due to the presence of polytypes and twin defects. It was observed, that the interface between different polytypes sections can affect the electronic and thermal transport [155, 157].

The knowledge of the relation between structure and functionality is crucial to control and tailor physical properties. However, it is very challenging to quantify the mentioned relationship; and this usually requires the handling and measurement of single NWs.

2.3.1 Characterization at the nano-scale

Here, a few examples of techniques extracted from literature are presented. Particular attention is given to techniques combining two or more characterization methods on one object. Nano-indentation [130], bending and tensile tests [22, 76], and resonant excitation [151] have been performed on a large variety of nano-materials. Chen [22] presented a study of individual InP nanowires bent by an AFM tip (see section 2.5). Simultaneously, Raman spectroscopy [22, 91] revealed a broadening of the measured signals, which was attributed to changes of the NW strain state. The elastic deformation of single SiGe islands was investigated by Scheler [130] with an AFM combined with in-situ X-ray Diffraction (XRD) (see section 2.5). This showed a decrease of the probed lattice parameter of 0.6% under compression. Wang [151] investigated the nano-mechanical response of carbon nanotubes and silica based NWs in combination with in-situ TEM (see section 2.5). In that case, TEM revealed the exact composition of the measured object. The elastic and bending moduli were obtained via mechanical resonance, induced by the application of an alternating electric field with a

frequency close to the resonance frequency of the system. Additional studies made use of techniques, such as μ-PL [36, 34] and cathodoluminescence spectroscopy [41]. The authors revealed the importance of the structural control of semiconductor nanowires. Indeed, the emission wavelenght can be controlled via the tuning of chemical composition and strain of the single nano-object. Combination of structural and optical characterizations were performed on single nano-objects, using XEOL [99, 100] and X-ray Fluorescence (XRF) [134]. Segura-Ruiz [134] evidenced a radial phase separation at the bottom of single MBE grown InGaN nanowires using XRD. This was related to the different In content measured by XRF in the same areas. Moreover, investigations have been reported on the electrical properties of as-grown NWs and their correlation with the NW dimensions (diameter and length) [145, 90, 86]. Talin [90] published a study on the electrical characterization of as grown Ge nanowires. In the mentioned paper, a dependence of the electrical characteristics on the diameter of the nanowires has been described. The significance of *surface effects*, such as the recombination time, is shown to be dependent on the diameters of the NWs, and reflects an increase of the current at zero bias for decreasing diameters.

In the following sections, electrical, optical and thermal properties of GaAs nanowires will be treated in detail; as they are important for the studies presented in chapter 5 and chapter 6.

2.3.2 Electrical and optical properties: the band structure

ZB GaAs is a direct band semiconductor with a nominal band gap of E_g=1.42 eV at room temperature. In intrinsic bulk GaAs, the following electronic parameters have been reported [66]: dielectric constant 12.9; intrinsic carrier concentration 2.1 $10^6 cm^{-3}$, intrinsic resistivity 3.3 10^8 Ωcm, breakdown field 4 10^5 Vcm^{-1}, mobility of electrons 8500 $cm^2V^{-1}s^{-1}$ and mobility of holes 400 $cm^2V^{-1}s^{-1}$. In NWs, the values of these parameters may vary by several orders of magnitude according to polytype composition, defect density, and NWs volume-to-surface ratio. As already stated, literature reports about the direct influence of the band structure on the electrical and optical properties of the material [138].

The value of the band gap of the WZ polytype has been extensively investigated in the past years [75, 21, 135, 82]. An agreement has not been reached so far, because of the strong

dependence of the values extracted on the experimental parameters; and on uncertainties related to the computational process. For example, Kusch [82] reported of an energy gap of ∼ 1.460 eV for WZ GaAs at room temperature. This value is very close to the one of ZB GaAs. In addition, he observed a vertical offset of both the conduction and valence band of ∼35 meV compared to ZB GaAs.

From an electrical point of view, the high aspect ratio of the NWs compared to bulk has a strong impact on the electrical parameters. The surface is a source of *surface states*, which are localized within the band gap and are responsible for a pinning of the Fermi level. In practice, those states narrow the actual conduction channel in the NW for the charge carriers, as they induce the formation of a depletion shell. The effect of surface states was studied by Casadei [17]. He underlined the importance of surface passivation on highly doped GaAs NWs (doping 1.3 10^{18}cm^{-3}), in order to increase the value of the effective mobility of the charge carriers.

From the optical point of view, De [32] reported on the dependence of the polarization angle (parallel or perpendicular to the growth axis) of the Photoluminescence (PL) emitted light on the anisotropic character of the dielectric function of the WZ polytype, in free standing III-V NWs. More in details, Hoang [7] determined the type of linear polarization of the emitted light: it was mainly perpendicular to the growth axis for WZ and parallel to the growth axis for ZB. Complementary, the same study [7] confirmed a staggered-type II band alignment at the ZB/WZ heterointerfaces. That means that the minimum energy of the conduction band and the maximum of the valence band are located in the two different polytypes; implying a longer recombination time and a reduced exciton binding energy [58]. Therefore, the interface of ZB and WZ is of particular interest for understanding electrical and optical properties. Recent studies reported on the influence of the polytypes mixture on the band configuration. Spirkoska [138] studied the symmetry and the energy structure of the valence band in WZ, and developed a theory to explain the difference in terms of shape and polarization detected in the PL spectra of ZB and mixed ZB/WZ NWs. From the PL measurements of pure ZB NWs, a single peak at ∼ 1.515 eV represents the free exciton energy of bulk [112]. From the PL of mixed ZB/WZ NWs, additional emission lines appear at lower energies. They are related to the presence of the ZB/WZ heterointerfaces, where a recombination of the 'indirect' excitons at lower energies takes place.

In pure WZ nanowires the presence of two states in the conduction band was experimentally observed [135]. The first, the *bright* band, corresponds to the nominal conduction band of ZB. The second, the *dark* band, is related to the states found in ZB along the [111] direction [135]. In GaAs, the vicinity of the two conduction states in terms of energy makes it possible to reduce the energy of one or the other band for example by strain changes. Signorello [135] reported on the tuning of the photoluminescence signal through a strain induced transition (minimum $\pm 0.12\%$) from a direct to a pseudodirect configuration. He used a tensile strain to lower the bright conduction band, and a compressive strain to lower the dark conduction band.

Demichel [35] studied the influence of the surface states on the optical properties. Non passivated and passivated GaAs NWs (with a AlGaAs shell) were compared, and revealed different transport mechanisms. In the first case, the defective surface states acted as charged traps (charge trap density of 10^{12}cm^{-2}) and caused a pinning of the Fermi level [131], with consequent reduction of the width of the transport channel. In the second case, the surface states were recombination centres for the free charge carriers [54].

2.3.3 Thermal properties

Important thermal parameters for bulk GaAs are the melting point 1500 K, the specific heat 0.33 $\text{Jg}^{-1}\text{K}^{-1}$ and the thermal expansion coefficient α 5.73 10^{-6}K^{-1}. From the thermoelectric point of view [23], GaAs NWs represent a good investment. Their higher boundary scattering at the NW surface decreases the thermal conductivity compared to bulk, maintaining a constant electrical conductivity. Soini [136] determined a lower thermal conductivity (between 8 and 36 $\text{Wm}^{-1}\text{K}^{-1}$) compared to bulk (55 $\text{Wm}^{-1}\text{K}^{-1}$), and the dependence on NWs diameter, analysing tapered NWs (see section 2.2). As reported later (in chapter 6), particular attention has to be accorded to the thermal expansion coefficient of the materials for electronic applications, to allow the integration of the nanostructures without affecting the capability of the device.

2.4 Applications

Semiconductor nanowires are crucial for the conception of integrated electronic and photonic nanoscale devices. Possible applications belong to the fields of electronics, photonics and optoelectronics. A few examples for GaAs-based NWs will be presented in order to emphasise the need of tuning their structure and properties.

2.4.1 Electronic, photonic and optoelectronic applications

In recent years, the growth methods have been improved to grow axial [37] and radial heterostructures [123], and to tune the doping level of semiconductor nanostructures. They combine materials with different properties (for example In, As and Ga composites), with different lattice parameters or with different doping levels. This allows to tune the band structure of the final device, and produce the so called quantum wells and quantum dots structures, to achieve quantum confinement [16]. Therefore semiconductor nanowires became important in modern electronics, photonics and optoelectronics [155]. Hereafter four selected examples are presented: transistor, laser, light emitting diode and solar cell.

Transistor

A remarkable application is the nanowire transistor. A transistor is a three terminal device, which can act as a switch or an amplifier. It is commonly realized in a sandwich structure, made of layers with different doping type (n-p-n and p-n-p) and/or different materials. In those configurations, the change of the potential in each region will determine the rate of charge carriers flowing across the device. Traditionally, two main types of planar transistor exist: the Bipolar Junction Transistor (BJT) and the Field Effect Transistor (FET). The BJT is constituted by a forward biased and a reverse biased junction, designed as a three layered sandwich structure with two external doped regions (emitter and collector) a shared slightly doped central area (base). The current flowing from emitter to collector is controlled by the current in the emitter-base forward diode. The FET controls the intrinsic charge carrier concentration within an internal conduction channel between a source and drain electrodes at the extremities, by tuning the polarity of the central gate electrode on the top of the channel.

The channel can originate from a p-n junction under inverse bias (Junction gate Field-Effect Transistor (JFET)), a metal/semiconductor (MS) junction (Metal-Semiconductor Field-Effect Transistor (MESFET)), or a capacitor (Metal–Insulation–Semiconductor Field-Effect Transistor (MISFET) and Metal-Oxide-Semiconductor Field Effect Transistor (MOSFET)). An important parameter, for the characterization of those devices, is the transconductance G_m. It is the change of the source-drain current I_D for a fixed drain voltage V_D, as a function of the voltage on the gate V_G:

$$G_m = \left(\frac{\partial I_D}{\partial V_G}\right)_{V_D=const}. \tag{2.3}$$

Tomioka [146] developed a high performance *surrounding-gate* vertical NW FET transistor. The NW geometry revealed to be crucial to keep an optimal control on the gate, which is provided from the wrapping of the InGaAs NW channel with a InP/InAlAs/InGaAs gate shell. In addition, an increase of the transconductance (eq. 2.3) up to $G_m \sim 1.6 mS\mu m^{-1}$ is observed in the core-multi-shell structures, compared to a simple InGaAs NWs device with $G_m \sim 0.1 mS\mu m^{-1}$; as well as the reduction of the occupied area compared to planar transistor [141].

Laser

III-V semiconductor NWs show a surface emitting lasing activity under optical excitation. They are potentially miniaturized natural laser cavities with two natural hexagonal end facets acting as reflecting mirrors. Lasers work on the principle of the stimulated emission, where the transition of electrons is allowed among discrete energy levels and results in the emission of electromagnetic radiation with a common phase relationship. Laser's emission is characterized by spatial coherence, collimation and temporal coherence, resulting in a narrow emission line. Depending on the material chosen, different emissions wavelength can be obtained: in a spectrum extend from the ultraviolet to the visible region. Since the first applications of ZnO [64] nanowires, other materials, such as nitrides and III-V semiconductors were successfully prepared. Mayer [103] reports on lasing in the infrared region with vertical emission from detached GaAs nanowires at room temperature. The GaAs active region was passivated with an AlGaAs shell, in order to inhibit the non-radiative surface recombination due to the high

density of defects state at the surface.
Moreover, the combination of photonics and electronics in the same device is possible thanks to the application of III-V NWs, and their integration with common materials in electronics (such as Si and Ge) [20]. The NW geometry is suitable for this integration both in terms of lattice mismatch and of different thermal expansion coefficients. Recently Lu [92] reported on the integration of InGaAs lasing nanopillars on a MOSFET. In that specific case the growth took place at low temperature (680 K), in order to prevent damages in the device and keep its performance un-effected.

Light emitting diode

Haraguchi [56] reports on the properties of GaAs nanowiskers, as light emitting diodes, with intrinsic p-n junctions and the dependence of their infrared emission on the polarization. As an example, light emitting diodes [118] are constituted by a p-n junction, where the excitation energy of an electron from the valence band to the conduction band depends on the value of the band gap E_g. Similarly, the combination of an electron from the conduction band with a hole of the valence band will produce a photon with the same energy. When a current flows through the device, the high recombination rate will lead to an emission with E_g energy. In addition, in a direct band gap material, such as GaAs, the probability of transition is higher compared to an indirect band gap material, where an additional phonon (lattice vibration) is required. The interatomic bond distance of the constituents directly determines the width of the band gap, this underlines the impact of the quality of the crystal lattice on the emission wavelength. In recent years, diverse p-n junction configurations, such as core-shell and axial heterostructures, have been developed. Those new geometrical configurations are shown to influence the performance of the devices. Rigutti [124] reported on the correlation of optical and structural properties of GaN/AlN core-shell NWs. In their case the core underwent an uniaxial strain along the growth direction, which was responsible for a blue shift of the photoluminescence, increasing with the shell thickness.

Solar cell

Combination of materials of the III-V groups is common for photovoltaic applications [87]. In particular, materials in nanowire geometry are of great interest because of their large surface area, the high aspect ratio and the possibility of creating ordered position-controlled arrays. In many practical devices, for example solar cells [156], an arrangement of the NWs at intentional sites may be required. Techniques based on the pre-growth patterning of a catalyst mask material by electron beam lithography [109] and nano-imprinting lithography [110] have been successfully applied in order to control the position of the wires accurately. In addition, a method has been developed to define the positions of the single NWs by the direct implantation of Au in the substrate, using a FIB system [50].
A solar cell works through the absorption of light and the production of excitons (electron-hole pairs), the separation of the charge carriers, and the external extraction of the separated carriers. Several geometrical configurations have been conceived for photovoltaic applications up to now. The core-shell geometry is of particular interest, as it allows the light absorption and the carrier separation to be decoupled axially and radially, respectively. This has the final objective to obtain the same efficiency with less material. Colombo [28] published an example of p-i-n GaAs NWs for the production of solar cell devices, which has been recently characterized by Krogstrup [80]. The latter reported an apparent efficiency up to 40%. This is due to an exceptional high light absorption, related to the vertical geometry of the NW, and the increase of the absorption cross section at wavelengths close to the band gap.

From the previous information, it becomes obvious that the lattice mismatch with the growth substrate and the high growth temperature are crucial for the integration of NWs in real devices. Another important issue, due to the inhomogeneous structure compared to thin films, is the metal contacting at the top of the nanowires. In the last few years, organic polymers, BCB, poly(methyl) methacrylate (PMMA), and SU-8, have been commonly used as embedding media for NWs devices [97]. The as-grown NWs are embedded in a polymer matrix onto the substrate, in order to fill the empty spaces, and to contact the NWs top with a thin metal layer [80, 146].

2.4.2 Piezo-electric applications

Piezoelectric materials are perfect candidates for energy harvesting applications, because of their ability to generate electric charge in response to a mechanical deformation. NWs, showing a piezoelectric response, are promising building blocks for the fabrication of nano-generators [59], and despite of the limits of such devices in terms of power output, strong advancements are possible. In group III-V semiconductors, the inverse piezoelectric effect arises from the lack of centro-symmetry along the [111] direction in the zinc-blende and [0001] wurtzite crystal structures. Remarkable differences have been observed in comparison to bulk materials. Minary-Jolandan [106] made use of Scanning Probe Microscopy (SPM) to determine the piezo-electric coefficients of single GaN NWs. The result showed an increase of up to six time the effect known from bulk. Moreover the impact of strain and composition has been shown to influence the piezoelectric effect in alloys, such as InGaAs [105], often used to structure quantum wells, wires and dots. In this context, Hocevar [61] reported on the observation of a photoemission red shift (up to 14 meV) in GaAs/AlGaAs core-shell NWs. He identified the tensile strain in the core along the [111] direction as the main origin; in agreement with the dependence on the shell thickness. In addition, he speculated on the piezoelectric effect due to an inhomogeneous Al composition in the shell. This lead to band fluctuations along the NW axis, causing local shifts of the emission line. The determination of the piezo coefficient in GaAs NWs revealed to be extremely challenging. Soshnikov [137] reported on the measurement of the piezoelectric coefficient of ensemble GaAs NWs. He related the unexpected high value compared to bulk, possibly to the high WZ content ($d_{33NW} = 26$ pC/N and $d_{14bulk} = 2.7$ pC/N [5] with $d_{33} = \frac{d_{14}}{\sqrt{3}}$ according to ref. [111]).

2.5 Selected techniques for structural characterizations

Application of NWs in real devices (presented in section 2.4) demands a homogeneous crystalline structure, free of defects, and tunable physical properties. Therefore, a large variety of structural characterization techniques have been developed (figure 2.4). They are commonly used for structural, elemental and morphological characterizations of single and ensemble NWs. Among them examples of characterizations via TEM, XRD, AFM, STM and SEM will be

reported.

Transmission Electron Microscopy (TEM) and High Resolution Transmission Electron Microscopy (HRTEM) [10] are widely used for determining the crystalline structure of single NWs. In both cases the NWs have to be removed from the substrate and placed onto a specific TEM grid (holey carbon cupper grid), after mechanical removal or sonication [41] and the subsequent dispersion in a solution (e.g. in isopropanol). HRTEM can be performed on samples with thickness between 5 nm and 50 nm [93] in plan-view and cross-sectional configuration, providing atomic resolution. It allows to determine with precision the position of the single atoms in the crystal lattice, to visualize the atomic stacking and to identify the diverse polytypes in the single NW structure. An example of a HRTEM and a TEM images is presented in figure 2.4 (d). In combination with TEM, Energy Dispersive X-ray Spectroscopy (EDS) can be performed to determine the elemental composition through the analysis of the EDS spectrum and its characteristic X-ray fluorescence peaks. In first approximation, the intensity can be related to the volume of the element inside the NW.

X-ray Diffraction (XRD) is a non destructive structural characterization technique. It allows the determination of the polytype content in ensemble and single NWs, of the interplanar distance and of the related strain state in crystalline materials. The technique will be presented in detail in chapter 3.

Atomic Force Microscopy (AFM) [153] can provide the surface profile of the measured samples with nano-scale resolution. It measures the force between a probing AFM-tip suspended on a cantilever and the surface under analysis. It monitors the cantilever deflection due to the inter-molecular force exerted between probe and sample. According to the sample-to-probe distance tree operation modes can be distinguished. In the contact mode (probe to sample distance < 0.5 nm), the close contact of tip and surface is driven by the repulsive inter-molecular force. The tapping mode (probe to sample distance from 0.5 to 2 nm) is characterized by an intermittent contact. In the non-contact mode (probe to sample distance from 0.1 to 10 nm), the distance leads the inter-molecular force in the attractive regime. A notable limitation of this technique is the tip convolution. It takes place when the radius of curvature of the AFM-tip is comparable to the size of the imaged feature and influences

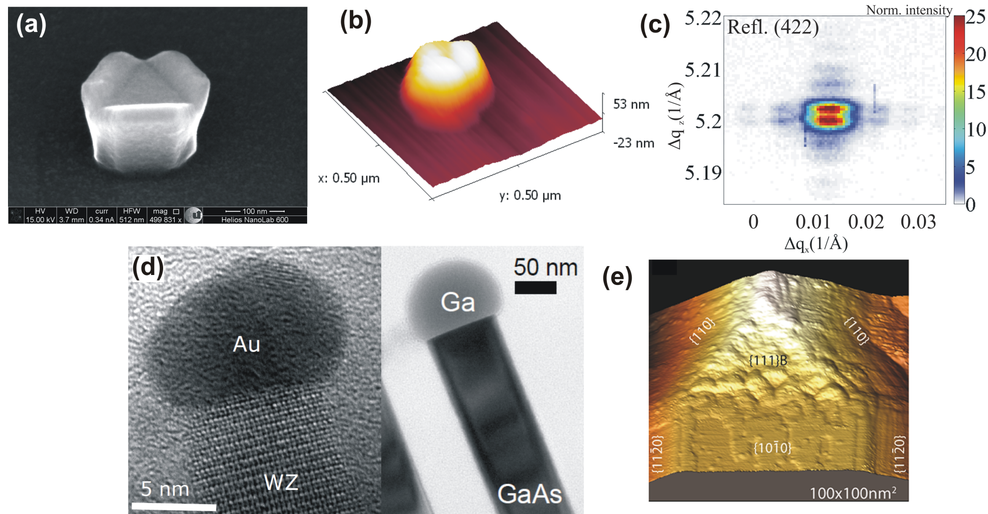

Figure 2.4: Selected techniques for structural characterization. A ~80 nm long GaAs NW is imaged with SEM (a) and AFM (b). Figure (c) shows the XRD diffraction pattern of reflection (422) from a single GaAs nanowire measured with a nano-focused X-ray beam. The extraction of structural parameters requires a specific data treatment. Figure (d) shows on the left a HRTEM image of a single GaAs NW (wurtzite (WZ)) with a gold droplet, and on the right a TEM image of a single GaAs NW with a Ga droplet. The shown images are published in ref. [15]. Figure (e) shows the STM image of a single GaAs NW. The image is courtesy of Rainer Timm and Martin Hjort and it is published in ref. [60].

the final sample image. AFM became a powerful tool in combination with other in-situ characterization techniques, e.g. XRD. The unique combination allows mechanical properties of single nano-structures to be studied. For example, a special designed AFM (X-AFM) has been used by Scheler [130] with XRD, to probe the in-situ elastic properties of individual SiGe self-assembled islands.

Scanning Tunneling Microscopy (STM) allows conductive surfaces to be imaged with atomic resolution. It makes use of a conductive tip, brought close to the surface. The application of a voltage difference, between probe and sample, allows the flowing tunnelling current to be measured. During the scanning of the tip on the surface, the changes in surface height and state density produce modifications in the measured current. STM with sub-nanometer resolution was successfully applied by Timm [145] to characterize electrically individual InP and InAs NWs, and showed a dependence on the NW diameter.

Scanning Electron Microscopy (SEM) provides the composition and topography of the measured samples. It makes use of an electron microscope, which collects the secondary electrons

emitted from the interaction of a focused electron beam with the sample surface. The technique is widely used for imaging ensemble and single NWs. It allows, for example, the three dimensional visualization of the NW side facets (figure 2.4 (a)).

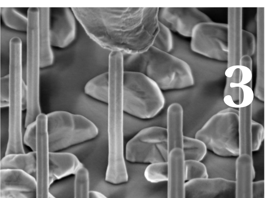

3 X-ray kinematic diffraction and synchrotron radiation

Chapter 3 gives an overview on the reciprocal lattice of crystals and a description of the basics of X-ray kinematic diffraction. Crucial for the success of the experiments presented in this thesis is the investigation of single NWs. The particular method of characterization will be described hereafter with details about the experimental apparatus and the sample configuration.

3.1 Reciprocal lattice and crystal planes

After discovery of quasicrystals, *crystals* are defined as any solids producing a discrete diffraction signal [67]. However, for introducing crystal planes and reciprocal lattice, the former definition of a crystal lattice, as the three dimensional periodic repetition of a *basic structural unit*, is a valuable starting point. The basic structural unit is the smallest unit, the primitive unit cell, defined by the basis $\vec{a}_1$, $\vec{a}_2$, $\vec{a}_3$, formed by the three vectors (primitive crystal axes) and hosting one lattice point only. It is necessary to introduce more complex units, in order to better describe the symmetric character of the crystal. In a unit cell containing n points, the position compared to the cell origin is given by the vectors $\vec{r}_n$. To define a mth unit cell with a certain distance from the crystal origin, the cell can be associated with three integer numbers m_1, m_2, m_3 giving the distance $m_1\vec{a}_1 + m_2\vec{a}_2 + m_3\vec{a}_3$ from the crystal origin. The nth atom position in this unit cell is given by $\vec{R}^n_m = m_1\vec{a}_1 + m_2\vec{a}_2 + m_3\vec{a}_3 + \vec{r}_n$ [152]. The 3D periodic arrangement of atoms in a crystal makes the identification of crystal planes possible,

with names and orientation specified by the Miller indices (h k l). Parallel lattice planes of the same density of atoms and distance, belong to the same family, having notation {h k l}. The symmetry of a hexagonal crystal can be as well expressed by denoting the planes with four indices (h k i l), where i=(-h+k). The knowledge of the lattice constant and the Bravais lattice [152] of the material allows the calculation of the interplanar distance d_{hkl}, which is

$$d_{hkl}^{cubic} = \frac{a}{\sqrt{h^2 + k^2 + l^2}} \tag{3.1}$$

and

$$d_{hkl}^{hexagonal} = \frac{a}{\sqrt{\frac{4}{3}(h^2 + hk + k^2) + (\frac{a}{c})^2 l^2}} \tag{3.2}$$

respectively for a cubic and a hexagonal crystal (those are the two types of crystal considered in this thesis). Brackets as [h k l] indicate the direction normal to the specific sets of planes indexed by (h k l). For X-ray diffraction, it is important to introduce the reciprocal lattice of a crystal [3]. For a crystal lattice with vectors $\vec{R}$ in real space, a set of vectors $\vec{G}$ in reciprocal space can be defined, such as $e^{i\vec{G}\cdot\vec{R}}$, which is satisfied if the product is an integer multiple of 2π. The reciprocal space vectors

$$\vec{b}_1 = 2\pi \frac{\vec{a}_2 \times \vec{a}_3}{\vec{a}_1 \cdot (\vec{a}_2 \times \vec{a}_3)}, \qquad \vec{b}_2 = 2\pi \frac{\vec{a}_3 \times \vec{a}_1}{\vec{a}_1 \cdot (\vec{a}_2 \times \vec{a}_3)}, \qquad \vec{b}_3 = 2\pi \frac{\vec{a}_1 \times \vec{a}_2}{\vec{a}_1 \cdot (\vec{a}_2 \times \vec{a}_3)} \tag{3.3}$$

can be combined to express

$$\vec{G} = h\vec{b}_1 + k\vec{b}_2 + l\vec{b}_3, \tag{3.4}$$

which is perpendicular to the planes {h k l} and whose magnitude is related to the inverse of the interplanar distance

$$G_{hkl} = \frac{2\pi}{d_{hkl}}. \tag{3.5}$$

3.2 Basics of X-ray kinematic diffraction

The kinematical theory [3] will be used to explain the mechanisms of X-ray diffraction from nanostructures. It makes use of the weak scattering approximation, neglecting multiple scattering effects. Only for large crystals with a high degree of perfection, the mentioned approximation is invalid and the so called dynamical theory steps in [6, 47]. In case of small crystals, within micrometer size, the following approximations are valid: absorption is neglected and the incident intensity is uniform for all atoms [53]. Based on the equation for the scattering of X-rays from a single electron [152]; the total amplitude of the scattered X-rays for a small solid crystal is given by

$$A(\vec{R}) = A_0 r_0 p \frac{e^{ikR}}{R} \int \rho(\vec{r}) e^{i\vec{q}\cdot\vec{r}} d\vec{r} \tag{3.6}$$

where $\vec{R}$ is the distance between sample and detector, A_0 is the initial amplitude, r_0 is the classical electron radius, P is a polarization factor which depends on the scattering geometry, k is the wavenumber equal to $\frac{2\pi}{\lambda}$ for elastic scattering, $\rho(\vec{r})$ is the electron density of the solid crystal, and $\vec{q}$ is the scattering vector $\vec{q} = \vec{k_f} - \vec{k_i}$, with $\vec{k_f}$ and $\vec{k_i}$ wave vectors of the incident and scattered waves. This expression neglects multiple scattering effects and includes the Fraunhofer approximation. In this approximation, both the primary and scattered waves can be considered as plane waves, due to the small size of the crystal compared to the distance of the X-ray source and the distance to the point of observation of the system. The integrated intensity scattered by a small crystal is proportional to the total number of scatterers (electrons) it contains. Measurable intensity in a specific region of the reciprocal space is observed in case of

$$\vec{q} = \vec{G}_{hkl} \tag{3.7}$$

(Laue conditions), forming a Bragg peak. In other words, the condition mentioned is fulfilled if the components of the wave vector transfer equal the corresponding components of a reciprocal lattice vector. In this case, the phase of the scattered waves sums up coherently and produce an intense signal. The Bragg law, equivalent to the Laue conditions can be expressed

as

$$n_{integer}\lambda = 2d_{hkl}sin\theta_B, \tag{3.8}$$

where $n_{integer}$ is an integer number indicating the diffraction order and θ_B (or θ) is the Bragg angle. In a crystal of finite size, a sum over all the electrons can be calculated by making use of the translational symmetry to express $\vec{r}$ as

$$\vec{r} = \vec{r}_{cell} + \vec{r}_n + \vec{r}_n^{\,'}, \tag{3.9}$$

with the use of $\vec{r}_{cell}$, $\vec{r}_n$ and $\vec{r}_n^{\,'}$, which indicate respectively the position of the unit cells, of the atoms in the single cell and the electron distribution around the n atom. The mentioned sum is

$$A(\vec{q}) \propto \sum_n (\int \rho(\vec{r}_n^{\,'}) e^{i\vec{q}\cdot\vec{r}_n^{\,'}} d\vec{r}_n^{\,'}) e^{i\vec{q}\cdot\vec{r}_n} \sum_{cells} e^{i\vec{q}\cdot\vec{r}_{cell}} \tag{3.10}$$

where the integral of the electron density is the atomic form factor $f_n(\vec{q})$, tabulated in ref. [120]. The equation can be rewritten as

$$A(\vec{q}) \propto \sum_n f_n(\vec{q}) e^{i\vec{q}\cdot\vec{r}_n} \sum_{cells} e^{i\vec{q}\cdot\vec{r}_{cell}} \tag{3.11}$$

where the two sums are the structure factor $F(\vec{q})$ and the *lattice sum*. The structure factor is the Fourier transform of the electron density distribution in the unit cell. As it is multiplied with the *lattice sum*, it represents the envelop function of all Bragg peaks in reciprocal space. As a consequence, recording intensity of multiple Bragg peaks in reciprocal space yields information on the atomic arrangement in the unit cell. In the case of GaAs, the unit cell is composed by two fcc cells occupied by two different types of atoms, displaced by one quarter along the cube diagonal. Here the structure factor is calculated by taking into account the atomic scattering factors of Ga and As. This calculation determines whether the waves interfere constructively or destructively at different atoms within the unit cell along a specific crystallographic direction. The *lattice sum* is the sum over all the cells in the lattice and is

related to the shape of the diffracting object. The diffracted intensity I is finally given by [53]

$$I = A(\vec{q}) \cdot A^*(\vec{q}). \tag{3.12}$$

3.2.1 Signals from nanostructures in reciprocal space

As shown before, the scattering amplitude contains the Fourier transform of the object shape [53]. This information is present in the diffraction signal, which has a characteristic shape and is inverse proportional to the size of the object. For a crystal in two dimension (a surface), the signal will adopt a rod-like shape, called Crystal Truncation Rod (CTR), pointing along the surface normal. As a surface in a real case corresponds to the termination of a three dimensional volume, the signal measured will correspond to the convolution between the CTR and the diffraction signal originated by the crystal volume [126]. The high surface-to-volume ratio of nanowires implies a strong presence of CTRs, which dominate the diffraction pattern. The latter is characterized by the presence of thickness oscillations, carrying information about the size of the object in the direction normal to the surface.

In real crystals, aberrations of the perfect order are generally observed; it is therefore useful to introduce the concept of strain ϵ. It can be expressed in the generalized form of Hooke's law [113] as

$$\epsilon_{ij} = S_{ijkl}\sigma_{kl} \tag{3.13}$$

where ϵ_{ij} are the strain components; S_{ijkl} are the compliance coefficients of the crystal; and σ_{kl} are the components of the stress applied to the crystal. Equation 3.13 can be also expressed as

$$\sigma_{ij} = C_{ijkl}\epsilon_{kl} \tag{3.14}$$

where C_{ijkl} (or elasticity matrix) is a fourth-rank tensor including the stiffness constants.

In order to extract the value of strain along a specific direction of the crystal, it is convenient to consider the variation of the interplanar distance with respect to the unstrained reference

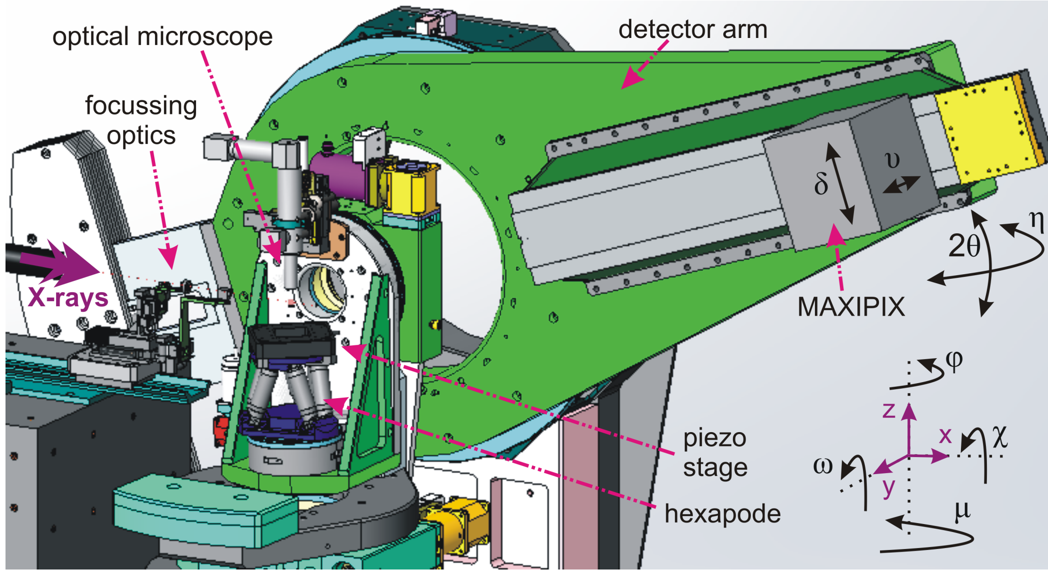

Figure 3.1: ID01 diffractometer. The original image is courtesy of Hamid Djazouli, ID01 (ESRF).

value $d_{unstrained}$. Thus strain can be defined along a specific direction in the crystal [hkl] as

$$\epsilon[\%]_{hkl} = \frac{d_{hkl,strained} - d_{hkl,unstrained}}{d_{hkl,unstrained}} \cdot 100. \tag{3.15}$$

The presence of strain will modify the appearance of the diffracted signal: it will result in an angular displacement in the case of homogeneous strain; and in a peak broadening in presence of inhomogeneities, as dislocations, vacancies, inclusions and elastic relaxation.

A reconstruction of the crystal structure from the diffraction signal has to take into account the *phase problem*. Indeed, only the amplitude of the scattered waves can be extracted from the XRD profile, while no information is given about the phase. In order to overcome the lack of information, specific reconstruction algorithms have been developed. They allow the retrieval of the amplitude and phase of the original shape of the object [125]. In this particular cases, enhanced visibility and high resolution of the diffraction signal can be obtained by ensuring that all the scattered photons have a well defined phase relation. One pre-condition for reconstructing the object from the scattering pattern is the illumination of the sample with coherent X-ray light. Synchrotron facilities provide partially coherent radiation. Here, the coherent part of the incoming beam can be extended by an aperture, whose dimension matches the coherence length of the beam [139].

3.3 A synchrotron beamline: ESRF-ID01

All the experiments presented were performed at the synchrotron beamline ID01 at the European Synchrotron Research Facility (ESRF) in Grenoble, France. Synchrotron radiation is produced by acceleration of electrons via the bending of their path. In this specific case, electrons are produced by a 100 keV triode gun and accelerated in a Linear Accelerator (LINAC) up to an energy of 200 MeV. The subsequent injection in a circular accelerator with 300 m circumference brings them up to an energy of 6 GeV. They are then transferred into the storage ring (844 m circumference), which contains bending and linear straight sections, respectively such as bending magnets, and insertion devices (undulators and wigglers) [9] where the X-ray radiation is actually produced. Then the X-ray beam produced is delivered to the respective experimental stations. Beamline ID01 at the ESRF has a dedicated experimental configuration for nano-diffraction experiments. Hereafter the main elements along the beam path in the optics and experimental hutches will be described, from the insertion devices to the sample position. Three undulators in series (two U35 with a 35 mm period (with band width peak $\frac{\Delta E}{E}$=0.01) and one U42, with 42 mm period, used to reach the lowest energies), deliver a beam with possible energy ranging between 2.1 keV and 40 keV. All the presented experiments have been performed with the instrumentation and capabilities available at ID01 until December 2013. At that time, the X-ray beam delivered in the optics hutch impinged on a double bounce Si (111) channel cut monochromator, with an energy resolution $\frac{\Delta E}{E}$=10^{-4} [38]. This selected the specific range of wavelength of the radiation. According to Diaz [38] the available transverse coherence length at ID01 has been estimated as 60 μm x 20 μm (vertical x horizontal); by considering a distance from source to sample of 50 m and a source size of 30 x 125 μm^2 (vertical and horizontal respectively). The shape of the beam was modified using slits apertures. In addition beam monitors and attenuators were introduced along the beam path. The monochromatic beam arrived at the sample position mounted on a diffractometer in the experimental hutch (figure 3.1). On the diffractometer, the sample can be translated in the x,y and z direction and rotated about the ω, φ and χ axes: all these movements are used to align the sample and for the data collection. A detector arm has a 2θ rotation in the vertical direction, and a η rotation in the horizontal plane. It is decoupled from the sample stage in order to avoid the transfer of vibrations to the sample, caused by detector movements. The sample is

mounted on a hexapod stage (Symetrie) for translations of the order of mm or sub-mm and tilt alignments. In addition a *direct driven piezo-translation stage* or PI (P-563 PIMars XYZ Piezo System, PI GmbH and Co.) is available on the hexapod for sample translations in the nm range. In the case of X-ray nano-diffraction experiments, the beam was focused with the use of Fresnel Zone Plates (FZPs), with typical diameter of 300 μm and an outermost zone width of 80 nm. This diffractive focusing device [70] yields a focus on the order of 200 x 400 nm^2 (vertical x horizontal). The final size depends on the used energy, the incoming beam coherence and divergence, and it can be affected by downstream optical elements and small vibrations of the experimental apparatus. A circular central beam stop (60 μm diameter) and a circular Order Sorting Aperture (OSA) (typical 50 μm diameter), positioned as close as possible to the sample, were used to block the direct beam transmitted and to clean the higher diffraction orders respectively. A two-dimensional MAXIPIX detector (pixel size of 55 x 55 μm^2, for 516 x 516 pixels^2) [119] was used to map the complete three-dimensional region in reciprocal space around the diffraction peak (figure 3.2). Recent developments at ID01 made use of the high sampling frequency of the MAXIPIX (kHz regime) in the so called quicK-mapping (K-map) method [19]. It is a fast scanning method, which allows the direct buffering, compression and storage of the collected images by a synchronized communication between the MAXIPIX camera and the PI stage during the real scan procedure. This is achieved using a Multipurpose Unit for Synchronisation, Sequencing and Triggering (MUSST) card, which eliminates the communication time between camera and control software (SPEC V6.00.03) during the sample scanning. This results in a significant reduction of the data collection time by two order of magnitudes, and therefore allows the collection of real space maps under diffraction condition in a reduced time (compared to the conventional scan mode) of 100x100 μm^2 areas of the sample.

Nowadays, in 2014, the beamline undergoes one year shut-down, for an extension and technical improvements. Details about this so called Phase I of the ESRF upgrade program can be found in ref. [65].

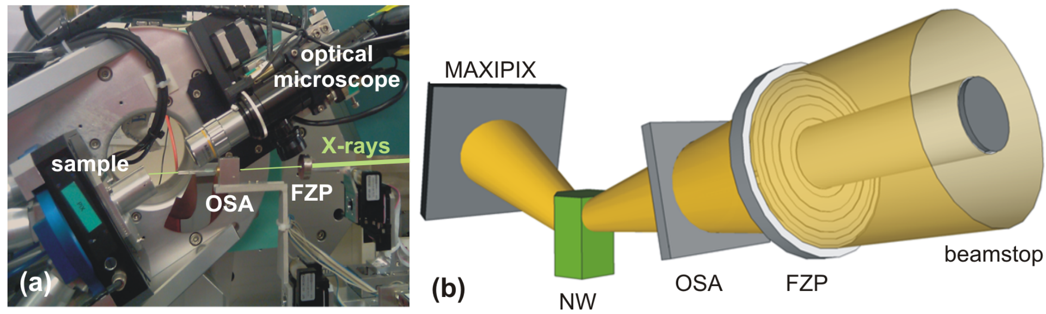

Figure 3.2: Photograph (a) and 3D sketch (b) of the available focusing configuration at beamline ID01. Image (a) is courtesy of Gilbert Chahine, ID01 (ESRF).

3.4 Diffraction geometries

In a typical XRD experiment from a small crystal, the sample is illuminated by the incoming X-ray beam, which gets diffracted by a set of planes for a specific value of the incident angle, depending on the Bragg condition. The specific angle is called ω, and will give a diffracted signal at 2θ position in angular space. Several diffraction geometries can be used; hereafter the coplanar symmetric and asymmetric reflection geometries and the non-coplanar GID geometry will be presented, as they have been used in the experiments performed and presented in the next chapters.

3.4.1 Coplanar symmetric and asymmetric geometries

In the coplanar symmetric geometry, selected sets of planes are ideally parallel to the sample surface: in this case ω is equal to the Bragg angle θ_B. In case of the coplanar asymmetric condition, the selected sets of planes will have an angle φ to the surface. This type of reflections can be accessed only for $\varphi < \theta_B$, for $\omega = \theta_B \pm \varphi$ according to the chosen grazing incidence (-) or grazing exit (+) condition. In this case, a rotation around the surface normal is needed in order to align the set of planes so that they diffract at the selected Bragg angle. The three components of the momentum transfer can be introduced as: q_z is the out of plane component parallel to the surface normal; q_x is the in-plane component parallel to the projection of the X-ray beam on the sample surface; and q_y is the in-plane component perpendicular to q_x. The three components can be derived from the incident and exit angle of the X-ray beam on the sample

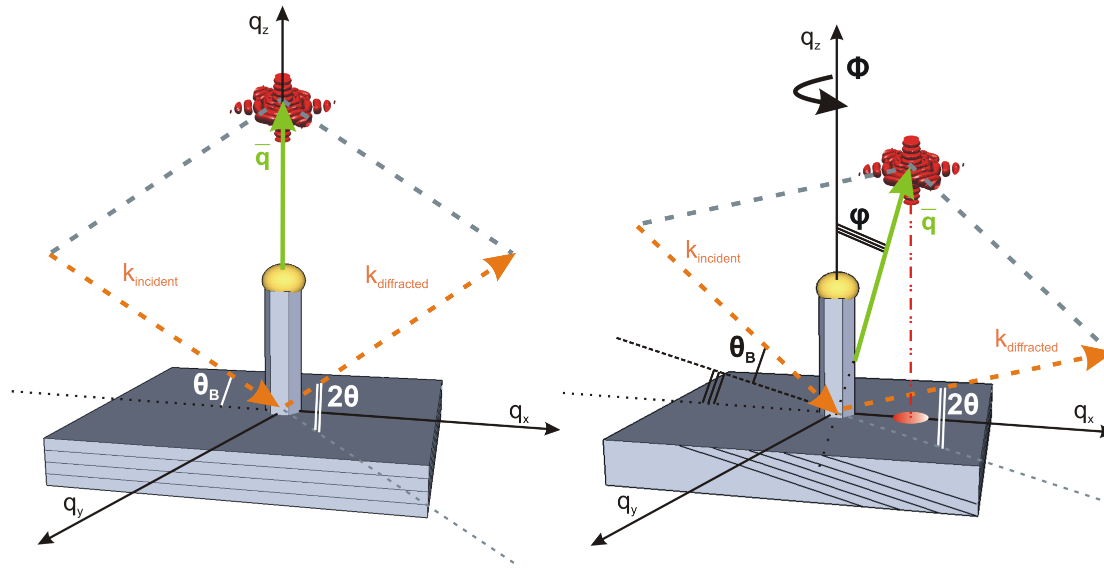

Figure 3.3: From left to right: coplanar symmetric and asymmetric geometries.

surface (ω and 2θ) and the exit angle of the diffracted beam on the detector (ν) [117]:

$$q_x = \frac{2\pi}{\lambda}(cos(2\theta - \omega) \cdot cos(\nu) - cos(\omega)), \tag{3.16}$$

$$q_y = \frac{2\pi}{\lambda} sin(\nu), \tag{3.17}$$

$$q_z = \frac{2\pi}{\lambda}(sin(2\theta - \omega) \cdot cos(\nu) + sin(\omega)). \tag{3.18}$$

A sketch of the symmetric and asymmetric coplanar geometries is shown in figure 3.3.

3.4.2 Non coplanar grazing incidence geometry

Grazing incidence geometry [42] consists in a combination of out-of-plane reflectivity and in-plane Bragg diffraction [117]. In order to control the depth resolution, the incident and exit beams are kept at small angles with respect to the sample surface, close to the angle for total

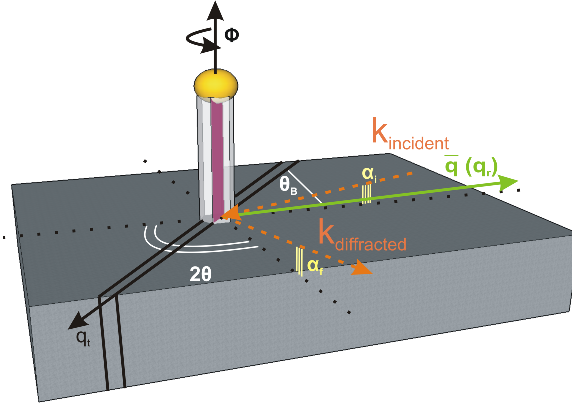

Figure 3.4: Sketch of the non coplanar GID geometry.

external reflection [42]

$$\alpha_c = \sqrt{2\delta} = \frac{\sqrt{4\pi\rho_e r_0}}{k}, \tag{3.19}$$

where δ expresses the refraction of the X-ray wave in the formula of the refraction index ($n_{refraction} = 1 - \delta + i\beta$, with β absorption parameter); ρ_e is the electron density; and r_0 is the classical electron radius. An evanescent wave is generated below the surface; it has a penetration depth $\frac{1}{e}$ ranging from tens to hundreds of nm [117] depending on the incident angle. A rotation of the sample around the surface normal allows the selection of a set of planes perpendicular to the sample surface, which satisfy the Bragg condition with wave vector transfer almost parallel to the surface. In addition, due to the small incident angle α_i (0.25° for GaAs) the technique probes the sample with constant penetration depth and is sensitive to the near surface region (depending as well on the used energy and the absorption of the material); as it suppresses the strong signal originating from the substrate. The incident nano-beam gives a large footprint onto the sample surface: in case of the measurement of a single NW, this makes object selection very challenging, as explained in section 3.4.4. In addition, as a selected part of the NW is illuminated, the complete measurement requires a scan of the X-ray beam along the NW growth axis. The components of the wave vector transfer (in the plane whose normal is parallel to the growth axis), q_r and q_t, are defined respectively parallel and perpendicular to the normal of the selected family of planes, as shown in figure 3.4.

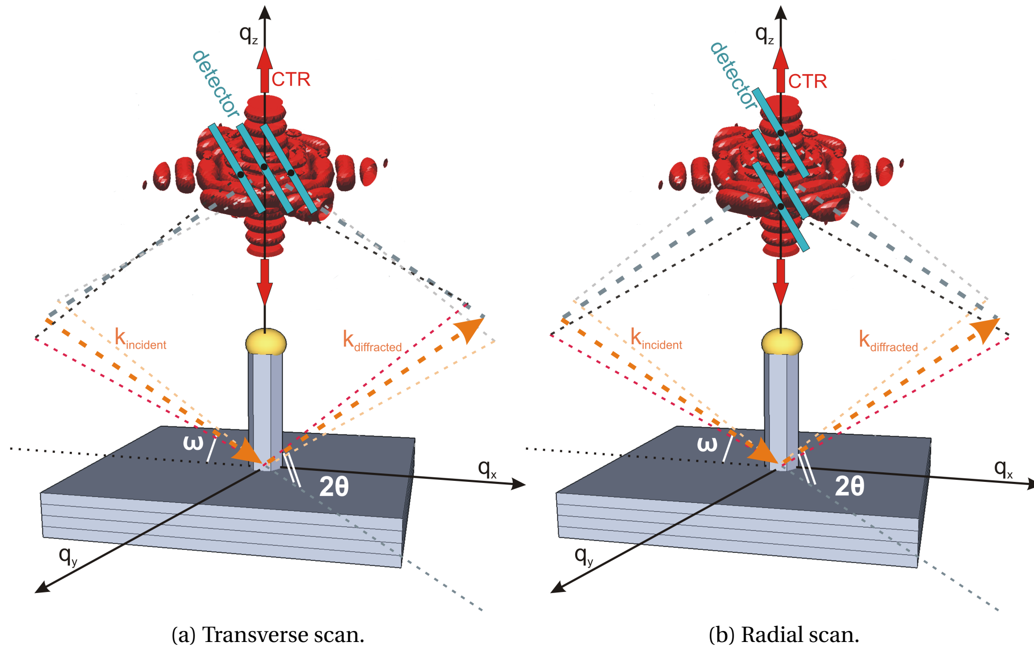

(a) Transverse scan.

(b) Radial scan.

Figure 3.5: Radial and transverse scan in XRD on a single NW in coplanar symmetric geometry.

3.4.3 Maps in reciprocal space

In all the presented experiments, the use of a 2 dimensional detector allowed the collection of two dimensional cuts in reciprocal space, with the simultaneous collection of intensity in small ranges of δ and ν (figure 3.1), whose size varies according to the sample to detector distance. A variation of the incident angle ω (and if needed 2θ) allowed the collection of the scattered intensity in function of the three components of the wavevector transfer for the reconstruction of three dimensional Reciprocal Space Maps (RSMs). A transverse ('rocking' scan, where ω changes) and a radial scan ('$\omega-2\theta$' scan, where both angles vary simultaneously) are presented in figure 3.5 for the coplanar symmetric geometry.

3.4.4 Specific sample configuration in the diffraction from a single nanowire

In X-ray nano-Diffraction (n-XRD), the illumination of a single nano-object is very challenging. As the footprint of the incident X-ray beam on the sample surface is large, the selection of a single NW is impossible in samples with a high number density (for example $10^8 cm^{-2}$). Samples suitable for single NW diffraction have to be well prepared. A low number density

is the first requirement in case of coplanar diffraction. An additional challenge steps in if a *specific* object has to be identified on the surface. In this case, micrometer-sized markers can be deposited or grown onto the surface. They can be easily identified with the help of an optical microscope mounted on the diffractometer above the sample surface (figure 3.2(a)), giving a first view of the area to be probed. Subsequently scanning X-ray diffraction microscopy in real space is used to identify the object under Bragg condition (K-map method [19]). Moreover, a controlled arrangement of the nanostructures onto the substrate is desirable, for example in GID geometry. In this case only a single nano-object has to be illuminated by a tens of μm sized X-ray beam. Also the combination of XRD with other ex-situ characterization techniques (see chapter 5) requires controlled positioning of the NWs on the substrate, unique condition to find again *the same* object.

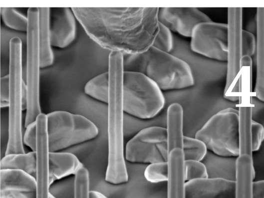

4 Grazing incidence X-ray diffraction of single GaAs nanowires

This chapter is centred on the X-ray diffraction measurements in GID geometry of single GaAs nanowires grown on a (111)-oriented GaAs substrate. The controlled arrangement of the NWs by Au implantation, in combination with a nanofocused X-ray beam, allowed the in-plane lattice parameter of single NWs to be probed, in particular to collect reciprocal space maps at different heights along the NW. This is not possible, in in-plane GID geometry, for randomly grown NWs. At the same time, substrate areas with different distances from the Au-implanted spots below the NWs were under observation, and the data suggested the presence of a compressive strain. Most of the elements (text and figures) presented hereafter are published in **Bussone *et al.*, *Journal of Applied Crystallography*, 46:887, 2013.**

4.1 Probing the in-plane strain in single GaAs nanowires

As stated in chapter 2, in present applications the control on the crystal structure of GaAs nanowires is very important, as they have to be homogeneous and free of defects. In addition, the control of their size and their exact location on the substrate is necessary. Those qualities strongly depend on the growth process. For many practical devices, an arrangement of the NWs at intentional sites, for example in regular arrays, is required. In order to control the position of the wires accurately, diverse techniques exist. Techniques, such as electron beam lithography [109] and nano-imprinting lithography [110], require the use of a photoresist on

the epi-ready monocrystalline surface, which represents a potential contamination source and cannot always be removed by cleaning. Therefore, the direct implantation of Au using a focused ion beam system [50] is preferable. It consists of a complete ultra-high-vacuum process, which includes layer growth, lateral structuration and subsequent NW growth. Previous characterization on single NWs in symmetric and asymmetric diffraction geometries allowed the determination of their morphology, structural composition and residual strain, by combining the use of a focused X-ray beam with coherent diffraction imaging [39, 11]. However, additional details about the NW crystal structure can be obtained by probing the planes whose normal is perpendicular to the growth direction, along the height of the wire. This requires working under GID conditions (see section 3.4.2). In order to perform GID characterization on single NWs, their controlled arrangement is critical. For randomly grown NWs the wide footprint of the X-ray beam on the sample does not allow the selection and analysis of a single wire, and therefore only average properties can be accessed.

4.2 GaAs nanowires at locations defined by focused-ion beams

The measurement was performed on undoped pure GaAs nanowires, grown on a GaAs substrate, where the positions of the NWs were intentionally determined by a direct implantation of Au with focused ion beams. The sample was prepared at the University of Bochum, in Germany, in the group of Prof. Andreas Wieck. The growth method consisted in the Au-assisted vapor–liquid–solid MBE (see section 2.2), combined with the capability of a FIB system to implant Au ions masklessly as catalytic metal seeds at the desired sites. The GaAs nanowires were grown on (111)B GaAs substrates using a Riber EPINEAT V/III S MBE system, equipped with a Ga effusion cell and an As cracker source. First, the substrate surface was deoxidized at 913 K, and then a GaAs buffer layer was grown. Afterwards, the sample was transferred in vacuum to a FIB system, an Orsay Physics Canion 31-Z FIB column including an ExB mass filter. Single-charged Au ions were generated from an AuBeSi liquid alloy ion source. Defined dot patterns were implanted using an acceleration voltage of 30 kV. The typical penetration depth of the Au+ ions was estimated to be ~15nm with The Stopping and Range of Ions in Matter (SRIM) [13, 160]. It was observed that an ion fluence of around 10^6 ions per spot was needed to obtain the growth of only one NW per site, although occasionally no or multiple

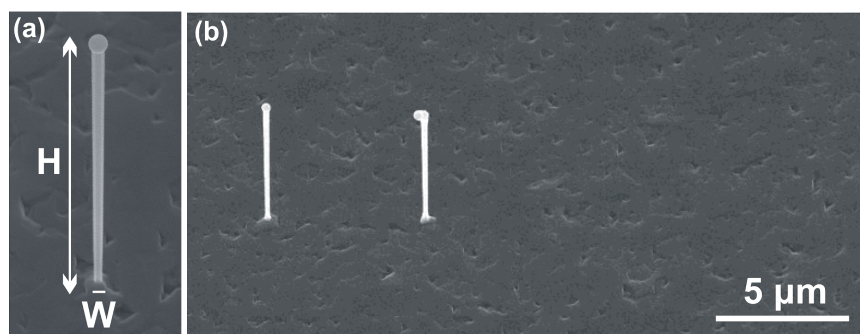

Figure 4.1: (a) SEM image of a single NW, with diameter W~150 nm and height H~6 μm. (b) SEM image of the rough substrate surface.

NWs have been obtained at one spot. The approximate size of the implantation spot in this case was ~200 nm. The sample was transferred back to the MBE system and heated to 823 K. Then the NW growth was initiated without delay and performed for 60 min with an As_4 flux to provide a constant V/III flux ratio of 13 and a Ga flux suitable for a two-dimensional growth rate of 0.2 nms^{-1} on GaAs(100). This resulted in (111)-oriented GaAs NWs with diameters of ~150 nm and a height of ~6 μm (figure 4.1(a)), which were located along a straight line, with a separation of 5 μm from each other. The chosen experimental geometry required a specific sample configuration and the presence of markers (numbers in this case). The orientation of the line of NWs with respect to the crystallographic directions of the substrate was chosen in such a way that the cubic (220) reflections of the NW and substrate could be accessed without intersection of the X-ray beam with more than one NW. The MBE growth parameters that were used for NWs and GaAs layers varied in temperature and As_4 flux. GaAs layers grown with NW growth conditions (substrate temperature: 823 K; V/III flux ratio: 13) get usually a rough surface morphology. As the layer growth does not stop while the NWs are growing, the (111)B surface between the NWs is typically fairly rough. This is clearly observed in the SEM characterization (figure 4.1(b)). In addition, the NW structure was determined with TEM, where a mixture of zinc-blende and wurtzite structures was observed and it is shown in figure 4.2. In HRTEM, the wurtzite structure is visible in figure 4.2(a). An HRTEM close-up with zincblende structure, twin planes and stacking faults, is shown as well in figure 4.2(c).

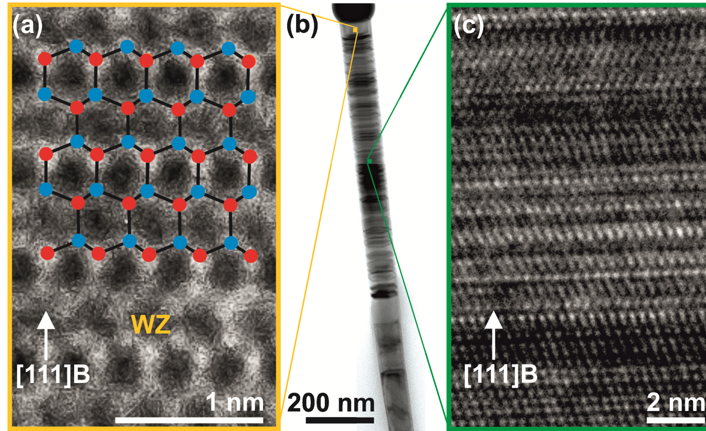

Figure 4.2: TEM image of the atomic stacking in a single NW: (a) HRTEM image of a pure wurtzite (WZ) structure region with superimposition of the atoms positions; (b) bright-field image of the top part of the NW; (c) HRTEM image of a zinc blende structure region.

4.3 The details about the experimental configuration

The NWs were investigated in grazing-incidence geometry with an 8 keV nanofocused X-ray beam, with measured focal size of 300 x 500 nm^2 (vertical x horizontal). Owing to the GID geometry, for an incident angle of 0.25° the footprint of the X-ray beam on the sample surface was 68 μm along the direction of the X-ray beam propagation. First, the sample was aligned at the symmetric (111) Bragg reflection in order to map out the intensity distribution in x and y directions on the sample. The NW was grown with a high content of the hexagonal wurtzite phase, which has a slightly larger out-of-plane lattice parameter compared with the substrate zinc-blende reflection [12]. Therefore, the scattering angles were fixed at the position expected for wurtzite (0002) and the sample was scanned along the x and y directions through the probing X-ray beam. Positions of increased diffracted intensity were identified as single NWs [39, 107]. A specific area on the sample was measured: it contained two markers and a row of single NWs spaced about 5 μm apart (figure 4.3). The markers were already visible in the available optical microscope (see section 3.4.4), whereas the NWs could be identified only by the increased X-ray intensity. Moreover, only a few of the arranged NWs are visible along the line. A few places are empty, either because of missing NW positions in the implanted pattern or because of a small misalignment of the NWs with respect to the substrate. Subsequently, the identified NWs were analyzed using GID, focusing the X-ray beam onto the identified x, y positions along the specimen. RSMs were collected around the ZB (220) reflection (equivalent

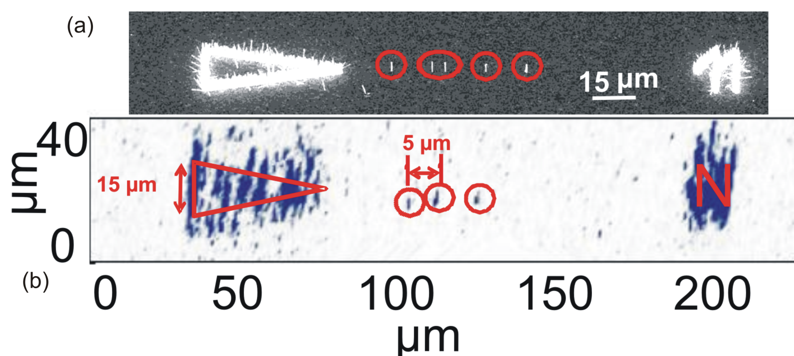

Figure 4.3: Comparison between the SEM image along a row of NWs (a) and a real space map (b) along a similar row under the diffraction condition for the GaAs symmetric (111) reflection. The diffraction signals of a triangular and a number-shaped marker (hard to identify in the RSM) are clearly visible. In the space between the markers, a few nanowires having the expected spacing of 5 μm can be distinguished and the positions of the NWs are marked with red circles.

to the WZ (2110) reflection) at different heights along the NW. Because the NW diameter was smaller than the X-ray beam and the absorption by the NW was negligible, most of the beam still hitted the substrate at different distances from the NW position. The components of the scattering vector $\vec{q}$, q_t and q_r, are defined as described in section 3.4.2. The complete two-dimensional region in reciprocal space around the diffraction peak was mapped. Reciprocal space maps were calculated by integrating the diffracted intensity along the whole range of the exit angle. For NWs grown epitaxially on a substrate, the lattice planes of both substrate and NW can be probed in the used geometry. If the NW and the substrate are constituted by two different materials, they diffract at different Bragg angles and their signals can easily be separated. In the present case, the NW and the substrate are both made of GaAs, i.e. they diffract at the same Bragg angle. However, by carefully examining the detector images, an additional signal, observed only for scans performed at NW positions and therefore attributed to the NW contribution, can be seen at a slightly different angular position along the rocking scan compared to the signal of the GaAs substrate. This allows the distinction between signals originating from the GaAs substrate and the rough surface layer, and the NW signal with much lower intensity, because of their different q_t positions, $\Delta q_t \sim 0.035\text{Å}^{-1}$. This separation is probably caused by a twist of the NW growth axis with respect to the substrate normal [74]. This may also explain the fact that other NWs could not be found at the expected position, if their misorientation exceeds a certain value. Figure 4.4 shows RSMs measured for selected

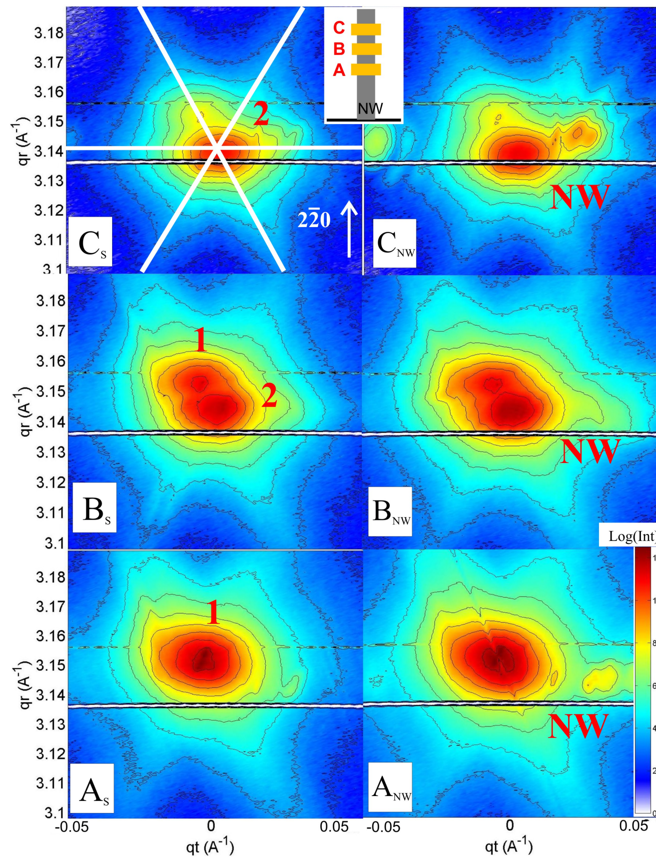

Figure 4.4: On the left, GID reciprocal space maps collected for three different regions of the substrate (A_S, B_S and C_S) at different distances from the NW. The strained and unstrained diffraction peaks are named 1 and 2, respectively. On the right, reciprocal space maps collected for regions A_{NW}, B_{NW} and C_{NW} along the NW. The NW signal, indicated in red as NW, is clearly visible on the right of the substrate peak.

regions on the samples: the graphs labelled A_S, B_S and C_S refer to a region free from NW growth; the graphs labelled A_{NW}, B_{NW} and C_{NW} are relative to one of the identified NW positions. The intensity of the substrate is much higher than that of the NWs due to the large difference in scattering volumes.

4.4 Determination of the in-plane strain

By changing the vertical position of the NW with respect to the incident beam, i.e. measuring at different heights along the NW, changes of the NW signal were hard to identify. However, as the position of the incident beam on the sample was simultaneously modified, major

changes were observed in the substrate signal. Figure 4.4 shows reciprocal space maps taken at different lateral positions on the substrate, marked as A_S, B_S and C_S, and corresponding to the three different positions of illumination along the NW long axis, A_{NW}, B_{NW} and C_{NW} (figure 4.5(a)). Considering steps of 2.5 μm in the vertical direction, the illuminated areas were separated laterally by 570 μm each, where position A is the closest and position C the most distant from the NW. The substrate signals show two different features partially overlapping for region B, at $q_r \sim 3.150\text{Å}^{-1}$ (indicated as 1 (A_S, B_S)) and at $\sim 3.142\text{Å}^{-1}$ (indicated as 2 (B_S, C_S)), and their intensity ratio is changing as a function of the illuminated position. At all positions, a *hexagonal star* (marked with white lines in (C_S)) was observed, probably originating from crystalline grains within the GaAs surface layer, growing simultaneously with the NWs. A few additional artefacts were visible close to the Bragg peaks, probably due to randomly oriented GaAs crystallites distributed on the substrate surface. They were also observed in SEM images and might have been created during the cleavage of the as-grown sample into smaller pieces. For quantitative evaluation, line profiles were extracted from the RSMs shown (A_S, B_S and C_S) along the radial direction q_r (figure 4.4). As mentioned above, two different peaks can be identified. For position A, peak 1 dominates. The two peaks show rather similar intensity at position B and peak 1 almost disappears at position C. The appearance of two different peak positions in q_r indicates the presence of a strained region. Considering peak 2 as the position of the unstrained GaAs, peak 1 indicates the presence of compressively strained GaAs in the vicinity of the implanted region. Indeed, the unstrained peak shows increasing intensity with increasing distance above the substrate (peaks relative to positions B_S and C_S). At first glance, this interpretation might contradict the expectation. As a result of Au implantation, a lattice expansion is expected because the atomic radius of Au is always larger than that of Ga and As. However, the induced lattice damage might be so large that this region does not contribute to the Bragg scattering signal. On the other hand, an increased lattice parameter in the implanted core must result in an outer laterally compressed region of GaAs, which explains this finding. This compressed part dominates while probing the region close to the NWs, and the compressive strain is expected to decay slowly over a large distance from the implanted area. Because of the large footprint of the X-ray beam on the sample surface, the strained peak measures a mean strain value, which was determined by fitting the measured diffraction profile with two Lorentzians, one for the uncompressed and one

for the compressed substrate contributions, shown by solid lines in figure 4.5. The data show a decrease of the in-plane lattice parameter: the region closer to the NW is compressed by -0.4% compared to the unstrained one. The NW signal is hardly accessible since the substrate is made of the same material; however there is evidence for the existence of NWs which can be further processed. A comparison between the different regions along one NW was carried out. As shown in figure 4.4 (A_{NW}, B_{NW} and C_{NW}), different regions along the NW were investigated by translating the sample along the growth axis with steps of 2.5 μm. In A_{NW}, the compressed substrate peak and the NW signal can be observed at similar q_r values, but with $\Delta q_t \sim 0.035$Å^{-1}. By extracting the line profile along q_r of a selected region of interest around the NW signal, it is observed that the signals coming from regions B_{NW} and C_{NW} along the NW are located at q_r positions similar to that found for the unstrained substrate. This means that the NW lattice is not strained. Conversely, the NW signal visible in A_{NW} appears shifted towards lower q_r by less than 0.03%; however an incomplete separation from the substrate cannot be excluded. The profiles of RSMs along q_r were processed for three different NWs measured in this experiment for the middle position B. The curves are the same within the uncertainties of the experiment. This proves that the intensity pattern of an individual NW could be extracted and separated from the substrate.

4.5 Summary

It is shown that individual as-grown GaAs NWs prepared by MBE after Au spot implantation by FIB into a GaAs substrate could be investigated by X-ray grazing-incidence diffraction using a nanofocused X-ray beam. The presence of two diffraction peaks was detected in different regions of the substrate. One corresponds to the unstrained substrate away from the NWs (more than 570 μm apart); the second peak originates both from the substrate deformation in the vicinity of the Au-implanted area and from the non deformed region in the substrate. The implanted region itself could not be accessed. From the relative peak shift observed in these two distinct regions in the substrate, it was concluded that the region close to the implanted area experiences an average lattice compression of -0.4% compared to the unstrained GaAs lattice. The detection of NWs grown within the implanted area was successful. For the first time, single NWs were investigated with n-XRD in GID geometry at different positions along

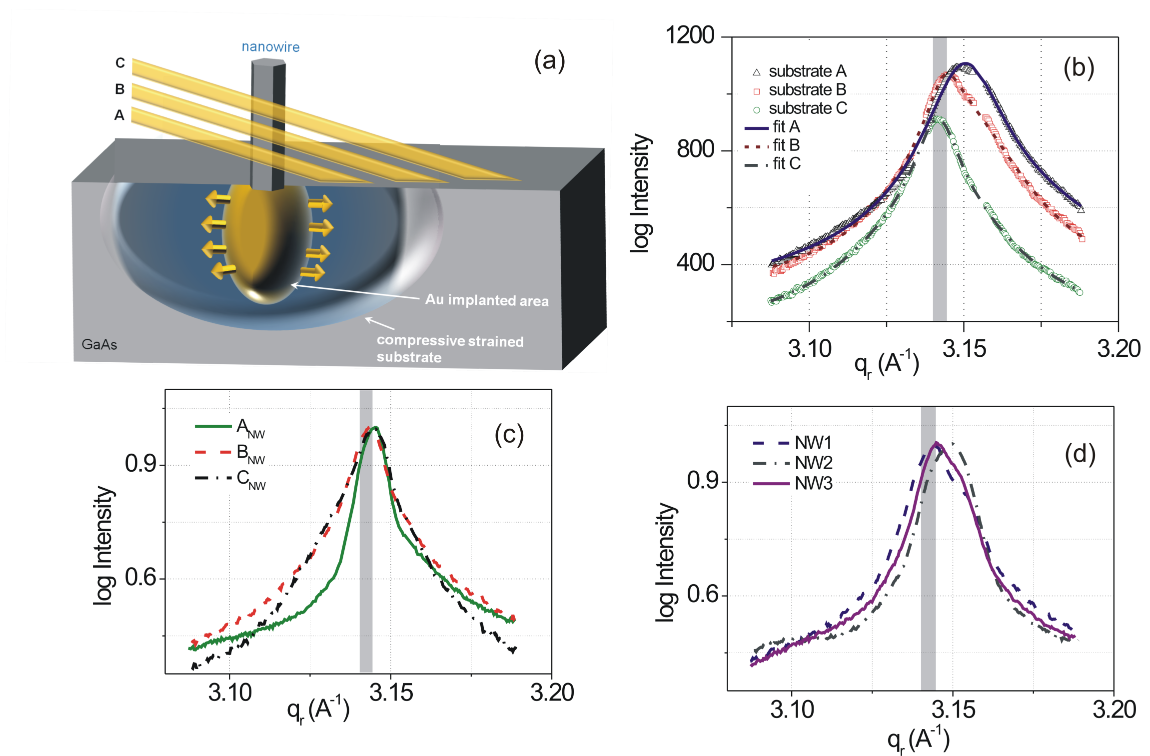

Figure 4.5: (a) A sketch of the NW and the substrate probed around the Au-implanted area. (b) Integrated diffracted intensity as a function of q_r for the three analysed regions in the substrate. Experimental and fitted data are shown. Here, and in the following graphs (c) and (d), the value of the estimated uncompressed GaAs is represented by a grey rectangular area. (c) Normalized integrated diffracted intensity as a function of q_r for three different positions (A, B and C) along the same NW. (d) Normalized integrated diffracted intensity as a function of q_r for three different NWs, at position B.

their height. Within the uncertainty of the experiment, the data showed that the lattice parameter of the NW equals that of the unstrained substrate. The wires exhibited a certain twist of the growth axis with respect to the substrate normal, which made their identification challenging.

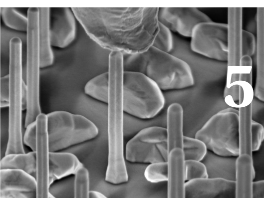

5 Correlation of electrical and structural properties in single GaAs nanowires

In chapter 5, the results of the study of the correlation between the electrical and structural properties of single GaAs nanowires measured in their as-grown geometry are presented. The chapter includes an overview of the Thermoionic Emission Theory and the Space Charge Limited Current model used in the analysis of the electrical data. The resistance and the effective charge carrier mobility were extracted for several nanowires, and subsequently the same nano-objects were investigated through X-ray diffraction. This revealed a number of perfectly stacked zinc-blende and twinned zinc-blende units separated by axial interfaces. Our results suggest a correlation between the electrical parameters and the number of intrinsic interfaces. The importance of such investigation has been emphasized in chapter 2 (in section 2.4) with examples and the description of recent technological applications where the control on the structure of semiconductor NWs revealed to be crucial. Most of the elements (text and figures) presented here are extracted from the manuscript
Bussone *et al.*, *Nano Letters*, 15(2):981, 2015.

5.1 Electrical measurement: the first attempts with an AFM

As a first attempt, the electrical characterization was performed using the X-AFM (see section 2.5) available in the Surface Science Laboratory (SSL) at the ESRF. Commonly a laser is used in combination with a photosensitive diode in an AFM system in order to determine the

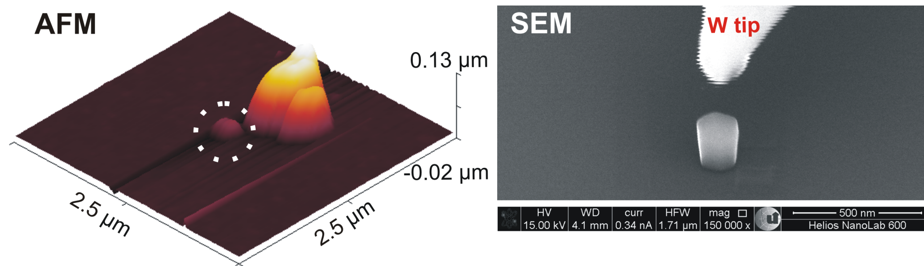

Figure 5.1: Comparison of an AFM (in the dotted white circle) and SEM image of two NWs on the same samples, collected before the electrical characterization.

deflection of the cantilever. However, in a system where an *optics free detection* [148] is required, a quartz tuning fork (TF) resonator is used. The TF oscillates with alternating signal at the resonance frequency and when the distance tip-to-surface is modified, the change can be related to a change in the interaction force. A tungsten tip was glued with Ag paste in electrical contact with the tuning fork. The tip approach to the sample surface was performed with the help of a camera, and the back contact was made on the back side of the Si wafer with Ag paste. The GaAs nanowires to be characterized were grown by self-assisted method in MBE on a Si substrate and etched in order to remove the Ga droplet from the NW top (via selective etching in HCl [15]). They were 30 nm high and had a diameter of 250 nm: those dimensions were chosen in order to minimize the damage induced by the scanning of the AFM tip, which on μm long NWs would likely break the nano-structures. In order to identify an object on the surface, the AFM was running in non contact mode. The images collected with the AFM showed immediately the instability of the system: due to the environmental noise and vibrations, which made the selection of a single nanowire very challenging. The AFM tip was then brought in contact to the NW top and a voltage from -5 V up to 5 V was applied, alternating with frequencies ranging from the 100 Hz to the kHz regime. From the comparison with the electrical signal collected with the open circuit, the V-I curve showed a poor signal-to-noise ratio. The first attempt highlighted the experimental aspects to be improved, and made clear the importance of a direct visualization of the object to be characterized. Afterwards, the electrical characterization was performed in a SEM-FIB vacuum chamber: this improved the quality of the Voltage-Current (V-I) curves with a reduction of the noise. As an example, figure 5.1 shows a comparison of the images for two NWs on the same sample, collected with AFM and with SEM.

5.2 The electrical and structural characterization of the same nanowire: samples and methods

For our study, (111)-oriented GaAs nanowires with diameters of 100 nm and height of about 1 μm were grown on a Si(111) substrate by self-assisted growth in MBE (see section 2.2) in the group of Dr. Lutz Geelhaar at Paul Drude Institute in Berlin, in Germany. In order to probe single NWs with the nano-focused X-ray beam, the substrate was patterned before the growth with a SiO_2 mask. Periodic openings in the mask with a pitch of 2 μm were fabricated by electron beam lithography [95], allowing the NWs to grow only at pre-defined positions across the substrate surface. NW growth took place at these openings; however island-type crystallites were also grown at many of the predefined places. Using a focused Ga^+-ion beam system, several of these parasitic islands were removed from the array by milling, in order to make single NW X-ray diffraction feasible. For this study, individual NWs were investigated electrically and structurally. The electrical characterization was performed in a FIB chamber using nanometer-sized tungsten needles with a mean radius of ~30 nm, driven by two piezo-manipulators (Kleindiek, MM3A-EM [77]) to contact the conducting substrate and the top of the single nanowire selected. The chosen nanowire was visualized inside the FIB chamber using SEM. The substrate contact was made on the surface, 10 to 20 μm away from the nanowire, by removing the SiO_2 layer from the surface and depositing a 6 μm diameter circular Pt-contact (1.5 μm thickness) using a Gas Injector System. Subsequently, with the SEM turned off, V-I characteristics with a voltage varying between -10 V and +10 V were measured using a semiconductor analyzer (Keithley 4200-SCS Parameter Analyzer [73]). Figure 5.2(a) shows a W-tip close to the top of a single nanowire. In order to identify nanowires previously characterized in the FIB chamber, Pt-markers (easily detectable with the optical microscope, as explained in section 3.4.4)) were deposited simultaneously in the chamber close to the position of interest. SEM images of the area close to the selected nanowires were then used for comparison with the nano-X-ray diffraction maps collected. The photon energy was 7.8 keV, and the X-ray beam was focused with a FZP down to a focal size of 400x700 nm² providing the spatial resolution required to achieve single nanowire inspection. A high degree of coherence was obtained by defining the illumination of the FZP with a slit opening of 0.1 mm (vertical) by 0.05 mm (horizontal), comparable to the transverse coherence length of

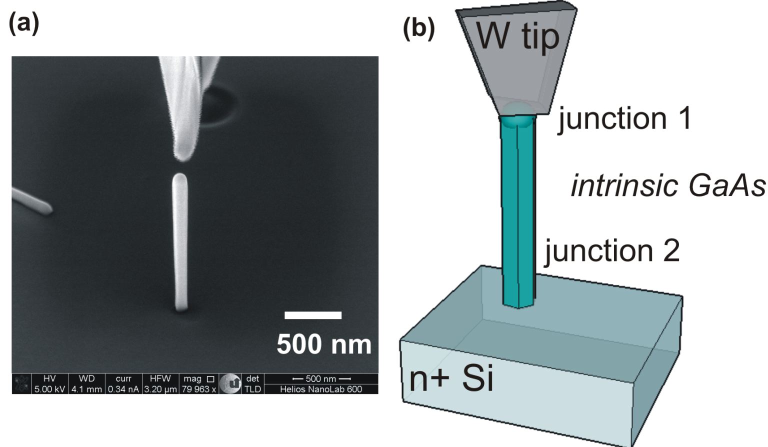

Figure 5.2: (a) SEM image of a W-tip close to the top of a single nanowire. The nanowire is 1 µm long and has a diameter of 100 nm. (b) A sketch of the contacted nanowire.

the beam at the energy chosen [101]. During the X-ray exposure, a constant nitrogen flux was blown on the sample, to protect the nanowires from possible radiation damage. Most notably, very fast mapping of a large area of the sample surface was performed using the K-map method, allowing a comparison with SEM images in order to find exactly the NW which had been characterized electrically. For accurate structural characterization, intensity maps as a function of the three components of the wave vector transfer (see section 3.4), i.e. RSMs, were collected for the structurally sensitive asymmetric (331), (422) and $(10\bar{1}5)$ reflections. For a fixed azimuthal orientation of the underlying Si substrate, one of the first two ZB reflections probes the ZB phase, the other one the TZB phase [11], and the third the WZ phase. In addition, we measured the structure of additional nanowires in their as-grown state, without the V-I measurements, to record the necessary reference.

5.3 The electrical characterization: theory and models

5.3.1 Contacts to a single nanowire

Extensive electrical characterization of NWs has been carried out on several semiconductor materials [143, 89], often after removal of the object from its original position on the substrate [132, 144, 31], and the deposition of two or four metal contacts via FIB [132]. However, as shown in paragraph 2.4, recent technological applications demand the use of NWs in their

as-grown geometry on the substrate. Studies of the electrical characterization of single NWs in their standing position on the substrate have been published in ref. [143, 48], and they make use of the same technique presented in paragraph 5.2. The quality of the electrical characteristics may be improved by coating the contact tip with a metal layer (for example with Au [143]) in order to obtain ohmic contacts both at the top (to a metal catalyst droplet) and bottom (to the substrate) of doped NWs. This simplifies the data treatment and allows the direct extraction of the electrical parameters, such as the resistance. In our case, the use of nominally undoped GaAs NWs, grown by self-assisted MBE, results in two MS junctions at the extremities of the nano-object. It is worth to mention that the coating of the W tip (with gold) has been performed as well and showed no significant improvements towards linear characteristics. The influence of the contacts could not be avoided in our case, and had to be taken into account in the data analysis, in order to provide a correct interpretation of the results.

5.3.2 Multiple regimes in a NW characteristic

According to Sze [140], a MS contact can assume a rectifying behaviour (Schottky contact) due to a barrier of potential induced by spatial charges in the semiconductor; or can assume a metallic (ohmic) behaviour with a resistance independent on the applied voltage. In presence of rectifying contacts, a bending of the band structure takes place at the MS interface. It produces a shift of the Fermi level due to the passage of one type of charge carriers across the junction. This introduces an electric field and leads to the formation of a depleted area, which includes the uncompensated donors. In this case, the minority carrier contribution can be neglected. In the case of a n-type semiconductor, the injection level (i.e. the applied voltage) determines the presence of different regimes, which can be treated by assuming a constant mobility and negligible diffusion of the charge carriers, and free and trapped carriers in quasi-thermal equilibrium (which implies a change in the Fermi level value) [18].

Current-voltage characteristics are classified depending on the type of contact. According to ref. [18], a typical characteristic of a n-type semiconductor may contain up to four different regimes: namely the regime of *ohmic conduction*, *Space Charge Limited Current (SCLC)*, *Trap Filled Limited Conduction (TFLC)* and *trap-free space charge limited current*. In the regime

of ohmic conduction the free carrier concentration is independent on the applied voltage: the Ohm's law is valid in this case and thermal electrons are dominating the conduction with respect to the injected ones. Ohm's law can be expressed as

$$J_{Ohm} = \sigma E \tag{5.1}$$

where J is the current density, σ is the conductivity of the material and E is the applied electric field. The SCLC regime occurs when the number of injected carriers exceeds the thermal carriers. A dependence of the current on the voltage square is observed for solid material, as a derivation from the Child's law for high vacuum diodes [26, 85], in the so called Mott-Gurney's law [108]

$$J_{Mott-Gurney} = \frac{9\epsilon\mu V^2}{8L^3} \tag{5.2}$$

where ϵ and L are the dielectric constant and thickness of the material, μ is the mobility of the charge carriers, and V is the applied voltage. This is valid in a free trap material by neglecting the diffusion current and the dependence of μ on the electric field. In this case the concentration of the free carriers depends on the applied voltage. In the TFLC regime trapped electrons lead the conduction and dominate the space charge at a constant voltage value (velocity saturation regime). At higher bias, in *trap-free space charge limited current* regime, the injected free electrons dominate again the space charge, and a dependence of the current on the square voltage is valid again (*ballistic* regime).

During the analysis of the collected Voltage-Current characteristics, a double regime was observed as well. In the log-log plot shown in figure 5.3, two consecutive regimes, characterized by different linear trends, can be observed. The first regime extends between approximatively 0V and +1V (between app. -1V and 0V in the negative voltage range, not shown here). In this case, the characteristic does not show an ohmic behaviour and the influence of the Schottky contacts dominates the observed trend (see section 5.4). This interval was fitted to the measured data in order to determine how the applied voltage is shared among the contacts and to extract the total resistance of the system. The second regime at voltages |V|> 1V is characterized by the formation of space charges due to the charge injection, which dominate

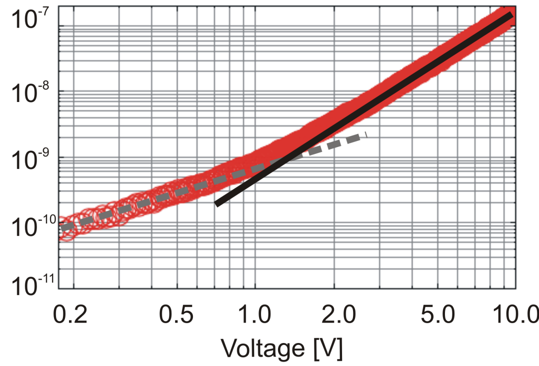

Figure 5.3: Log-log plot of one V-I curve: the different slopes correspond to the Back-to-Back Schottky diode regime (dashed gray line) and the Space Charge Limited Current regime (continuous black line).

the carrier transport (SCLC).

5.3.3 Thermoionic emission theory and Schottky model

At the interface of a Schottky diode, the band configuration has a particular structure. By assuming that only one type of charge carriers plays a role in the transport; when the two interfaces are in contact, the Fermi levels of metal and semiconductor will get at the same energy value according to the thermodynamic equilibrium. In a n-type semiconductor, this induces a bending of the conduction band with the formation of a barrier $q\Phi_B$ (known as Schottky barrier), which in the ideal case can be defined as:

$$q\Phi_{Bn} = q(\Phi_m - \chi) \tag{5.3}$$

and

$$q\Phi_{Bh} = E_g - q(\Phi_m - \chi) \tag{5.4}$$

for a p-type semiconductor

where q is the electron charge, Φ_m is the work function of the metal (which is the energy difference between the Fermi level and the vacuum level), and χ is the electron affinity of the

semiconductor (which is the difference between the upper limit of the conduction band and the vacuum level).

According to Sze [140] the electron concentration n in the semiconductor can be expressed as

$$n = N_c exp(-q(\Phi_B - V)/k_B T) \tag{5.5}$$

where N_c is the effective density of states, T is the temperature (in this case, 300 K), Φ_B is the height of the Schottky barrier, k_B is the Boltzmann constant, q is the magnitude of the electron charge and V is the voltage applied to the contact. According to Rhoderick [122] the current density J_{SM} for negative charge carriers passing the barrier from the semiconductor to the metal is

$$J_{SM} = \frac{pqn\vec{v}}{4} = \frac{pqN_c\vec{v}}{4} exp(-q(\Phi_B - V)/k_B T) \tag{5.6}$$

where p is the tunneling probability of the electrons through an hypothetical thin insulating layer at the interface; and accordingly to the model of isotropic velocity distribution of Maxwell [122], $\frac{n\vec{v}}{4}$ is the number of incident electrons (per area unit and per second) on the insulating layer with $\vec{v} = (8k_B T/\pi m_{eff})$ average thermal velocity of the electrons and m_{eff} effective mass of the electrons in the semiconductor. An opposite flux of current will flow from the metal into the semiconductor independent on the applied voltage

$$J_{MS} = \frac{pqN_c\vec{v}}{4} exp(-q\Phi_B/k_B T). \tag{5.7}$$

The resulting current is

$$J = J_{SM} - J_{MS}, \tag{5.8}$$

this can be rewritten as

$$J = A^* T^2 exp(\frac{-q\Phi_B}{k_B T})\{exp(\frac{qV}{k_B T}) - 1\} \quad (5.9)$$

with the Richardson constant

$$A^* = 4\pi m_{eff} q_B^2 / h^3 \quad (5.10)$$

with $p = 1$ for an infinitely thin insulating layer and $Nc = 2(2\pi m_{eff} k_B T / h^2)^{3/2}$, with h Planck constant.

In a real Schottky diode, Φ_B may be almost independent on the working function of the metal; instead, the surface states at the interfaces in the band gap usually influence the final height of the barrier by acting as donors or acceptors [140]. This effect is taken into account in the Bardeen theory [8]. Other lowering factors may be the image force [122], the existence of an insulating layer at the interface [159], and the field penetration [122]. The current flowing through the contacts described is mainly due to the motion of the majority charge carriers. At room temperature for slightly doped semiconductors (for example n-doped to a level of $10^{17} cm^{-3}$) the dominating transport mechanism is the thermoelectric emission of the majority charge carriers which pass the potential barrier. As shown in eq. 5.9 at the thermodynamic equilibrium two opposite equal fluxes of charge carriers result in no current. When a voltage is applied to the contact, for example in direct polarization, the barrier is reduced and the resulting current is not zero anymore. Similarly, an increasing of the barrier takes place in the case of inverse polarization. A V-I characteristic for a Schottky junction in thermoelectric condition can be expressed as

$$J = A^* T^2 exp(\frac{-q\Phi_B}{k_B T}) exp(\frac{qV}{n_{ideality} k_B T}) \quad (5.11)$$

for $V > \frac{3k_B T}{q}$, where $n_{ideality}$ is the ideality factor of the diode (1 in the ideal case, when the diode follows the ideal diode equation). In real diodes a resistance in series has usually to be

taken into account, and it modifies eq. 5.11 to

$$J = A^* T^2 exp(\frac{-q\Phi_B}{k_B T}) exp(\frac{q(V - R_s I)}{n_{ideality} k_B T}). \tag{5.12}$$

According to the method presented by Cheung [24] it is possible to extract the resistance in series of a Schottky diode via eq. 5.12, with

$$\frac{dV}{d(lnJ)} = R_s A_{eff} J + \frac{n_{ideality}}{(\frac{-q}{k_B T})} \tag{5.13}$$

where A_{eff} is the cross section of the contact. Eq. 5.13 provides a linear relationship between the quantity $\frac{dV}{d(lnJ)}$ and the current density J.

Thermoionic emission theory is not the dominant mechanism when tunneling through the barrier becomes significant. The quantum-mechanical tunneling can occur in two different cases [115]. In the first case, the Field Emission theory (FE), the tunneling in forward bias takes place in case of a metal in contact with a degenerate semiconductor at low temperature. Here the energy of the tunneling electrons corresponds to the Fermi level in the semiconductor. In the second case, the Thermoionic Field Emission theory (TFE), an increasing of temperature increases the energy of the electrons above the Fermi level, together with the probability of tunneling. However, the number of excited electrons becomes lower, so only a certain number of charge carriers will have energy above the bottom of the conduction band. At very high temperature, all the electrons will pass over the barrier, leading to a free-tunneling regime towards pure Thermoionic Emission Theory. At room temperature the tunneling becomes relevant again in reverse bias at low doping level ($10^{17} cm^{-3}$) [150]. In our case, for nominally undoped NWs, in first approximation both mechanisms may be excluded. Only in reverse bias, TFE may play a role. According to Rhoderick [122] this is included in eq. 5.11, and consists in a deviation from ideality (i.e. $n_{ideality} > 1$).

5.4 Back-to-back Schottky model: the data analysis (method A)

The theoretical elements presented have been used in a Back-to-back Schottky diode model [2, 63] in order to extract the resistance of our measured system. The presence of defects

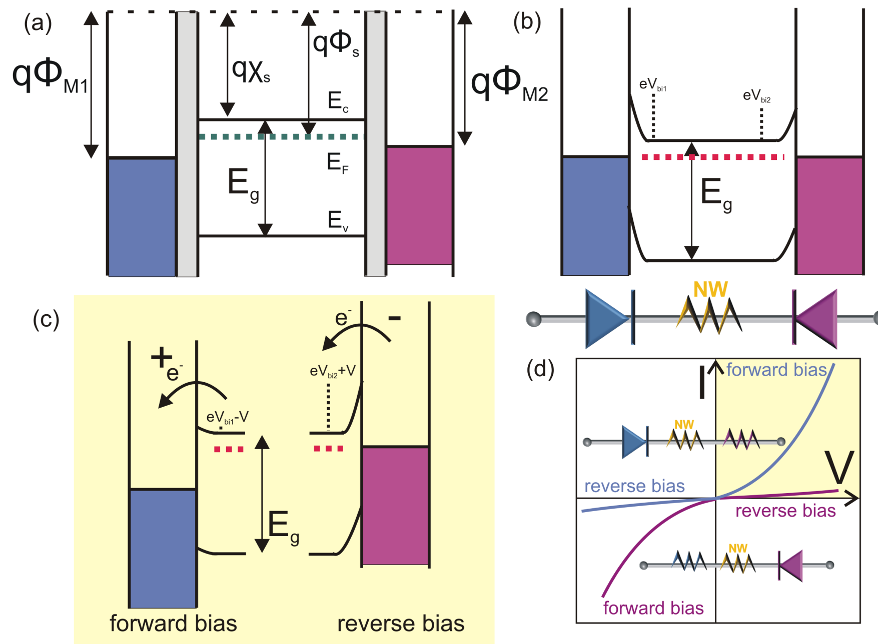

Figure 5.4: Sketch of the back-to-back diode band configuration of a metal(1, blue)/semiconductor/metal(2, purple) system. In the shown example, the semiconductor is n-doped and the two metals have work functions $\Phi_{m1} > \Phi_{m2} > \Phi_s$. (a) shows the constituents of the junction before the contact; (b) shows the condition at the thermodynamic equilibrium; and (c) shows the system under forward and reverse bias. The contributions of the back-to-back diode components to the electrical characteristic can be found in (d). Here, the area of the plot with yellow background corresponds to the two contributions shown in (c).

and surface states modifies the nominal undoped character of the NWs, whose transport can be therfore treated by Thermoionic Emission Theory. The measured system can in first approximation be described by two Schottky barriers embedding the NW. The two MS junctions are NW/W-tip and NW/highly n+ doped Si substrate ($10^{19} cm^{-3}$ Sb doping). The last junction is treated as a semiconductor/metal contact [86], considering the fact that the high doping level of the substrate results in a metal-like behavior. This assumption reduces the contact between the Si substrate and the Pt contact (to the surface) to a simple metal/metal contact. According to the double Schottky diode model, the Schottky contact will be active at either the first or the second junction, depending on the sign of the applied voltage. When not active, one of the two Schottky diodes will have a resistive behavior (as observed in the case of low doped semiconductor, $10^{16} cm^{-3}$, with small values of the Schottky barrier (figure 5.4)), in series with the resistance of substrate, the active diode and the nanowire itself. Hereafter the extraction of the total resistance in series R_s is presented. Consistent with this model,

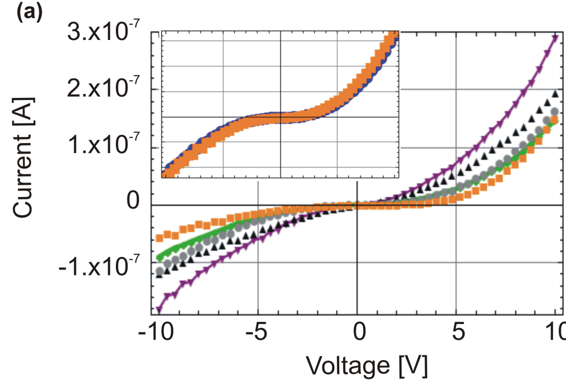

Figure 5.5: Voltage-Current characteristics of several NWs. The different trends in the non-linear curves are visible. (Inset) Current as a function of voltage, with axes ranging from -10 V to 10 V and from -1 10^{-7}A to 1.5 10^{-7}A for voltage and current respectively. An example of the curves collected for a single NW for two consecutive contacting procedures is shown: the curves are superimposed and no significant difference is observed.

the curves in figure 5.5 display for both positive and negative voltages a typical non-linear Schottky behavior. The shapes of the curves are different in the two voltage ranges, which is explained by differences in deviation from the ideal Schottky behavior between the top and bottom contacts. The total current density for the two diodes (diode 1 and diode 2), from eq. 5.11 is the same in first approximation

$$J = J_1 = J_2 = \frac{J_1 + J_2}{2} \tag{5.14}$$

and can be written as

$$J = \frac{1}{2}(A^* T^2 exp(\frac{-q\Phi_{B1}}{k_B T})exp(\frac{qV_1}{n_{ideality_1} k_B T}) - A^* T^2 exp(\frac{-q\Phi_{B2}}{k_B T})exp(-\frac{qV_2}{n_{ideality_2} k_B T})) \tag{5.15}$$

where the applied voltage V is distributed between the two contacts, having values V_1 and V_2. A weighting parameter α ($0 < \alpha < 1$) was introduced, such that $V_1 = V(1-\alpha)$ and $V_2 = V\alpha$, in order to quantify how the total voltage V is shared. As a first step of method A, the experimental curves were fitted to eq. 5.15 (figure 5.6) in order to extract the α parameter and to determine the effective voltage applied to the two contacts. The parameters used in the fit had the

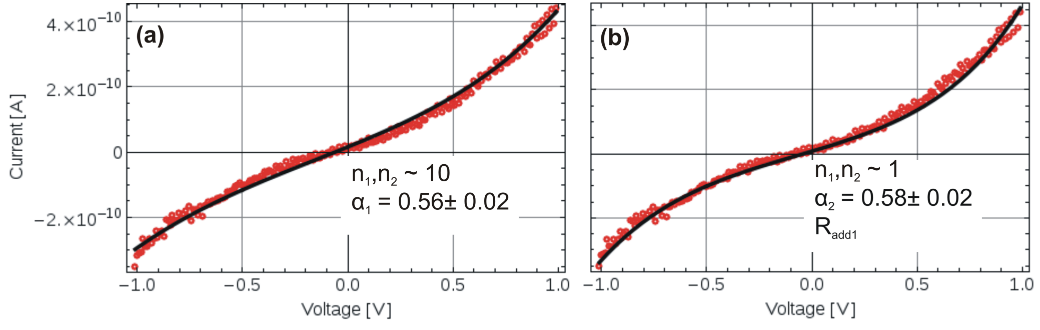

Figure 5.6: The results of the fitting of the electrical characteristic for a single GaAs NW in the range -1 V to +1 V are shown (original data in red and fit in black). The reported n_1 and n_2 are the ideality factors of the two diodes.

following values: $A^* = 4.4\ 10^{-4} Am^{-2}K^{-2}$ [140] (fixed); T= 300 K (fixed); Φ_{B1}= 0.2 eV (variation range ±0.2); Φ_{B2}= 0.2 eV (variation range ±0.2); and the current density J was calculated with the diameter extracted from the XRD analysis. The fitting procedure was executed in two different ways. As a first approach, the curve was fitted with eq. 5.15 with the ideality factor as a free parameter. This provided an ideality factor of the order of 10 for the different NWs and a weighting parameter α_1 equal to (0.56 ± 0.02) as shown in figure 5.6. The value of the ideality factors (not close to ideality) can be attributed to the presence of a resistance in series with the active Schottky diode. Therefore, an alternative fitting procedure of the experimental curves was performed by introducing an additional series resistance R_{add_1} [24] of the order of 10^8 to 10^9 Ohm, which is necessary to fit the experimental curves, with the ideality factor n ~1. The introduction of R_{add_1} in eq. 5.15 complicates the fitting procedure because it requires the use of a recursive fitting algorithm, due to the presence of I in both terms of the equation. The new equation requires the use of additional free parameters, and reduces the reliability of the fit. However, it was observed that the introduction of R_{add_1} corresponds in first approximation to a reduction of the voltage by a factor 10. Therefore the original V data have been modified to take into account the effect of R_{add_1}. The weighting parameter extracted α_2 becomes equal to (0.58 ± 0.02), as shown in figure 5.6, and it is comparable with the value of α_1. It is worth noticing that the extracted value of α is independent on the value of n obtained in the procedures described.

As a second step of method A, the actual voltages V_1 and V_2 on the active diodes were used to evaluate the total series resistance R_s for the negative and positive slopes of the curve through

eq. 5.13, by considering a diode and a resistor in series. The data were treated for V_1 and V_2 separately, and the mean value of R_s (from the positive and negative sides of the characteristic) was calculated. As mentioned before, the total resistance of the system is equal to

$$R_s = R_{add} + R_{NW} \tag{5.16}$$

where

$$R_{add} = R_{substrate} + R_{OhmicContact} + R_{SchottkyDiode}. \tag{5.17}$$

R_{add} is supposed to be the same for different NWs grown on the same substrate. This assumption is supported, for the top junction, by the fact that the repetition of the top contact on the same NW, with slightly different configurations, gave reproducible characteristics. An example is shown in the inset of figure 5.5. This difference will be then used as uncertainty of the extracted parameters for each NW. The dependence of the resistive behaviour on the size of the bottom contact has been analyzed as well and shows that a dependence on the diameter of the bottom contact (for ± 10 nm) can be excluded. The electrical characteristics for one NW (indicated as NWδ) have been modelled through equation 5.15 by varying the size of the bottom contact A_{eff_1} (figure 5.7 (a)). R_{add_1} was taken into account using the voltage correction introduced before, with $n_{1,2}$ ~1. The diameter of the bottom contact has been changed from 100 nm diameter to 90 nm and 110 nm. This variation is also compatible with the nominal resolution of the e-beam lithographic technique used to control the growth position of the NWs [95]. A deviation can be observed on only one side of the characteristic. In figure 5.7(b) the original and simulated curves for two NWs (NWδ and NWγ) are shown. The electrical characteristics have been modelled as explained above, with equal size of the bottom and top contacts ($A_{eff_1} = A_{eff_2}$). For comparison, the purple square and the blue star symbols in figure 5.7(b) indicate the maximum deviations, respectively, of the modelled curves shown in figure 5.7(a) for NWδ. They are incompatible with the experimental data, where mirrored differences among the NWs can be observed on both sides of the characteristics in figure 5.7(b) for positive and negative voltages. The simulated curves for NWδ, with a different size of the bottom contact, do not reproduce (not even qualitatively) the trend observed in NWγ.

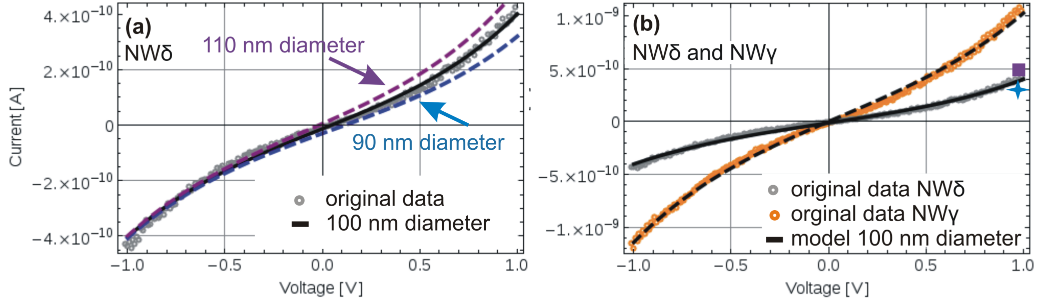

Figure 5.7: (a) Modelled electrical characteristics for different diameters of the bottom contact of one NW (NWδ): 110 nm (purple dashed line); 100 nm (black line); 90 nm (blue dashed line); and experimental data (grey). (b) Comparison of modelled curves and original data for two different NWs (NWδ and NWγ). The purple square and the blue star symbols indicate the maximum deviations of the modeled curves for NWδ shown in (a).

This suggests an independence of the electrical characteristics on the diameter of the bottom contact.

The measured variation of R_s among the different NWs can be therefore associated with differences of R_{NW}. In order to check the reproducibility of the measurements, the same nanowire was contacted several times, by subsequently approaching the W tip to the top of the NW and applying different but not further specified pressure. The current-voltage curves collected were compared to quantify the influence of the contacting procedure. The inset in figure 5.5 shows two characteristics for the same NW obtained by two subsequent tip approaches, and it displays only minor deviations (similar behaviour was also observed by Korte [20]). The remaining difference is smaller than the differences measured between diverse nanowires, and that is used as the uncertainty of the parameters extracted. In most cases the estimated uncertainty is three times lower than the effective difference between extracted R_s of different NWs. The total values of R_s and R_{NW} are estimated both to be of the order of 10^8 Ω: this shows a dominance of R_{NW} in the resistive behaviour, compared to the other term of eq. 5.16. In recent literature, various values of resistance have been published for GaAs NWs. Among them, Korte [78] reported on the resistance in the order of kΩ for $10^{18} cm^{-3}$ doped GaAs NWs (length ~ 8 µm, diameter ~ 100 nm). Casadei [17] measured a resistance per unit length of ~ 10^2 kΩ/μm for GaAs NWs with a similar doping level (diameter ~ 70 nm). The resistance of our intrinsic NWs revealed to be three orders of magnitude higher (~ 10^2 MΩ/μm). The mean values of R_s for each NW are reported in table 5.1. As explained

before, an experimental uncertainty was firstly determined for each NW by measuring several VI characteristics under slightly different pressures. Secondly, a statistical uncertainty was calculated for the mean value of R_s, as the standard deviation of the average value from the positive and negative sides of the characteristic. As the experimental uncertainty was larger than the statistical one, the average between the experimental uncertainties for the positive and negative sides of the characteristic was finally chosen as error of the measurement. (The uncertainties for the effective mobility extracted using method B are similarly determined.)

5.5 Space Charge Limited Current model: the data analysis (method B)

Subsequently the second range of data, measured from |1| V up to |10|V, has been treated via SCLC model [142, 127]. This regime implies the formation of a space charge region within the NWs which influences the charge carrier transport. The model allows the extraction of the effective charge carrier mobility, whose trend is the inverse of the resistance values extracted by method A. The equation for bulk GaAs was used to fit the experimental data (eq. 5.2) (figure 5.8) and extract the value of the effective charge carrier mobility μ (see table 5.1). In a recent work, Joyce et al. [72] reported on the basis of THz spectroscopy experiments a GaAs NW mobility in the order of 1000 cm^2/Vs (NWs length ~2 μm, diameter 30 to 80 nm) for nominally undoped wires. The difference in the values could arise from the dimensions and the different crystal purity of Joyce's NWs. Commonly, a lower mobility compared to bulk values (electron mobility 8500 cm^2/Vs and hole mobility 400 $cm^2V^{-1}s^{-1}$ [140]) is observed, probably arising from charge carrier scattering at the nanowire surfaces. The large aspect ratio of the NW geometry and the high surface recombination velocity, due to the surface states at the midgap of GaAs, are a source of traps in the NWs and are responsible for the pinning of the Fermi level within the bandgap. This induces the formation of a depletion region, and has an influence on the mobility [132]. As an example, a surface charge trap density of the order of $10^{12} cm^{-2}$ is reported in reference [35] for a depletion thickness of 50 nm. As shown in [17], passivation of the side walls can be used to increase the mobility.

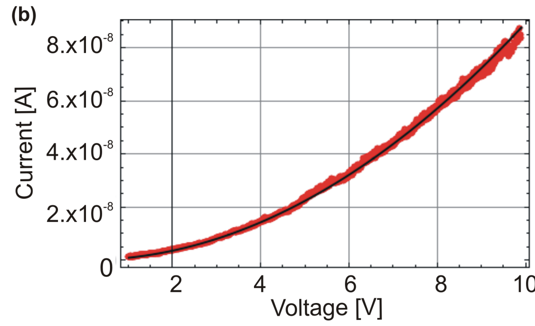

Figure 5.8: (a) Simulated V-I curve following the SCLC model (in black) and experimental data (in red) for one of the nanowires measured.

Table 5.1: Electrical parameters.

Nanowire	$R_s(M\Omega)$	$\pm Error(M\Omega)$	Mobility $\mu(cm^2/Vs)$	$\pm Error(cm^2/Vs)$
NW1	662	117	15	2
NW2	292	56	32	1
NW3	480	61	23	3
NW4	69	14	82	6
NW5	357	14	27	7
NW6	279	43	33	7

5.6 Total series resistance, effective mobility and charge carrier density

The calculated R_s and effective μ are shown in table 5.1. The extracted values of $R_s \sim 10^8\Omega$ and effective mobility $\mu \sim 10\ cm^2/Vs$ both fit to the same electrical characteristic assuming a certain charge carrier density ($n_{density}$). Considering majority charge carriers only, the charge carrier density can be calculated at the intersection of the two regimes (5.3.2), using the following equation [140]

$$n_{density} = \frac{L}{qA(\mu R_s)} \tag{5.18}$$

where A and L are the hexagonal section (extracted from the structural analysis) and nominal length of the nanowire, respectively; and q is the electron charge. The dispersion of the

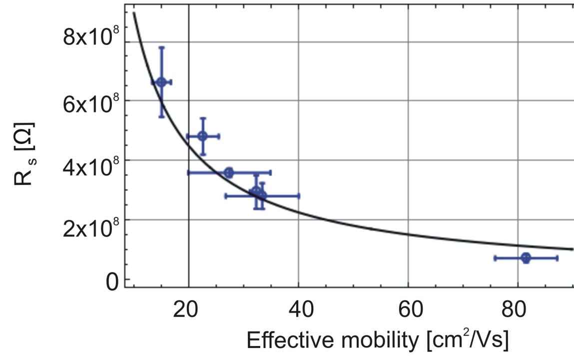

Figure 5.9: The dispersion graph of R_s as a function of the effective μ is shown. The fit (black curve) enabled the extraction of $n_{density} \sim 10^{16} cm^{-3}$.

measured resistivity R_s (method A) and effective μ (method B) fits to $n_{density} \sim 10^{16} cm^{-3}$ (figure 5.9). This value is much higher than the nominal charge carrier density for intrinsic bulk GaAs, and probably arises from the high nanowire aspect ratio and its related surface effects.

5.7 The structural characterization

In order to find if the cause of the observed electrical behavior lies in the NW crystal structure, a thorough X-ray nano-diffraction analysis of the same NWs has been performed. N-XRD has already proven to be an incomparable tool for assessing single object properties in relation to their structural properties [62] and, in this work, the analysis of the same single NWs was performed after their electrical characterization. An example of the analysis for one NW will be presented hereafter. The same procedure was followed for all the measured objects. For every NW, the ZB-sensitive (331), (422) and the WZ-sensitive ($10\bar{1}5$) reflections were measured. For WZ, no intensity was detected in the corresponding area of reciprocal space, from which we deduce the low content of this phase in the NW structure. Instead diffraction signals have been collected for ZB and TZB. As an example, figure 5.10 shows a 3D intensity map in the vicinity of the (331) reflection of GaAs. At $q_z \sim 4.58$ Å^{-1} two diffraction peaks can be distinguished, separated by a distance of ~0.02 Å^{-1} along the q_y axis. Both peaks are accompanied by thickness oscillations visible as equally spaced peaks along q_z. The period of the thickness oscillations differs between the peaks, indicating that these peaks arise from two independent crystalline segments of the NW at different heights along the growth direction.

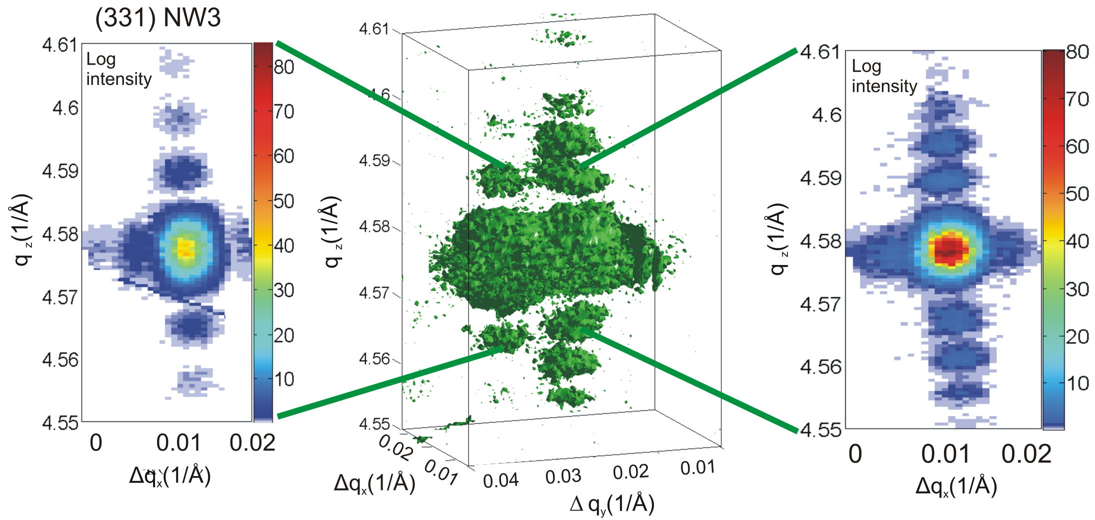

Figure 5.10: 3D reciprocal space map of NW3 for reflection (331): two peaks and their fringes are visible along the q_z axis. On the left and right of the 3D image, the projection of the two peaks on the $q_x q_z$ plane is shown. Due to the colour scale chosen to emphasize the vertical fringes, horizontal fringes are hardly visible in this image.

This may be related to the presence of several extended segments of pure ZB inside the same nanowire structure. The projections of the 3D map onto the $q_x q_z$ plane in figure 5.10 contain the finite size oscillations, which are visible in this case along the vertical components of the momentum transfer. Horizontal fringes along the direction perpendicular to q_z have been observed as well. Those fringes carry information about the height (H) and diameter (D) of the segments probed within the NW (see equ. 3.5). As a first approach, the dimensions can be extracted through $H = 2\pi/\Delta q_z$, and $D = 2\pi/\Delta q_{x,y}$, with Δq_z, $\Delta q_{x,y}$ being the distances of adjacent maxima along the respective directions. However, sometimes multiple sets of fringes were observed around a single peak along the q_z axis (figure 5.11 (a)). In order to extract information from such a complex system, the experimental data were modelled by calculating the diffracted intensity for one or more segments of pure ZB (with a certain distance between each other along the growth axis) in order to obtain the size of the diffracting elements. The simulation was carried out in Matlab [102] by building up the whole atomic structure of the crystal of the zinc-blende stacking of (111) planes inside the nanowire, and by calculating the diffracted intensity with respect to the desired q-space values.

First of all the positions of the Ga and As atoms in a portion of NW (with a diameter up to 100 nm) have been calculated [11]. The spatial coordinates (X and Y) in the A, B and C planes

(see section 2.1.1) were determined for Ga and As. Then the atomic stacking along the [111] direction was built as a repetition of the three types of planes; and the same for As with an additional translation from the Ga positions $\Delta Z_{As} = \Delta Z_{Ga} + a_{cubic}\frac{\sqrt{3}}{4}$. The total amplitude was then calculated for each nth atom in the crystal with respect to the selected range in reciprocal space, around the desired reflection with a modification of eq. 3.11

$$A(\vec{q}) \propto \sum_n f_n(\vec{q}) e^{i\vec{q}\cdot\vec{r}_n} = \sum_n f_n(\vec{q}) e^{i\vec{q}_{XY}\cdot\vec{r}_{XY}} e^{i\vec{q}_Z\cdot\vec{r}_Z}. \tag{5.19}$$

According to the translational properties of the crystal, $e^{i\vec{q}_{XY}\cdot\vec{r}_{XY}}$ was calculated only once for the A, B and C planes with respect to q_x and q_y; and then $e^{i\vec{q}_Z\cdot\vec{r}_Z}$ was determined for the different positions along Z (varying according to the chosen segment length) with respect to the chosen q_z range. The factors $f_n(\vec{q})$ were derived for each $\vec{q}$ value from the formula in ref. [129]. In the end, the two complex values obtained for Ga and As have been summed up and the intensity was obtained with the modulus square (eq. 3.18). The intensity signal as function of the q_z values allowed the quantification of the periodicity of the thickness oscillation fringes, originating for the simulated segment inside the NW. Multiple set of fringes were simulated by introducing one or more phase shifts between diffracting units vertically stacked inside the NW.

The (422) reflection was also measured for the same NW (figure 5.10 (b)) as it carries information about the TZB content. The procedure described was applied for both reflections of all the NWs measured, and the structural parameters are listed in table 5.2. As an example, the extracted phase structure of one NW (NW3) is shown in figure 5.11 (b). It displays structural units of different lengths (within the uncertainty of the simulation of ± 1 nm) but the same diameter of about (95$\pm$10) nm. The grey units correspond to that ZB phase whose azimuth is the same as the substrate (reflection (331)); the yellow segment is twinned by 60°with respect to the substrate setting (reflection (422)).

5.7.1 The effect of the tip contact on the NW structure

Diffraction signals, similar to the ones shown in figure 5.10 (a), were found for all the NWs. Their radial displacement pointing towards q_x or q_y was not always the same. Due to the

Table 5.2: Structural parameters.

Segments length (±1 nm)	NW1	NW2	NW3	NW4	NW5	NW6
TZB (422) refl. [nm]	181; 251; 14; 69	220; 205	95	128	124; 120	57
ZB (331) refl. [nm]	72; 330; 107	52; 206; 260	16; 82; 16; 75	209	210	98; 105
Sheared portion (422) refl. [nm]	/	/	≥ 810	≥ 470	/	≥ 255
Sheared portion (331) refl. [nm]	/	/	/	/	≥ 380	≥ 380
Total length (including the sheared portions) [nm]	1024	943	≥ 1094	≥ 807	≥ 834	≥ 895
Number of segments (including the sheared portions)	7	5	6	3	4	5

differences observed, it cannot be excluded that a few sub-peaks may be located outside the observation window.

To investigate the origin of the peak splitting, structural characterization was performed at untouched NWs as well. Also in this case, as for the contacted NWs, we found ZB and TZB units, both accompanied by oscillation fringes. However, there was a significant difference in the diffraction signal of the untouched NWs: the peak splitting was always found along the [111] direction (not shown), whereas the peak splitting for the contacted NWs was along the q_x or q_y directions. This is probably a signature of stacking faults present along the growth axis [49] between two or more ZB and TZB units. In contrast, no trace of additional splitting appears in the plane perpendicular to the growth direction. The in-plane peak splitting for the electrically probed NWs could instead be a result of the contact procedure, and measure a small plastic deformation within their structure. A recent work of Jacques et al. [68] studies the formation of defects after controlled compression of InSb nanopillars. In their work, (213)-oriented structures are chosen, thus leading to the activation of only one type of parallel slip planes. In our case, a compression along the [111] growth axis would lead to more complex deformation of the crystal structure due to the simultaneous activation of several secant {111}

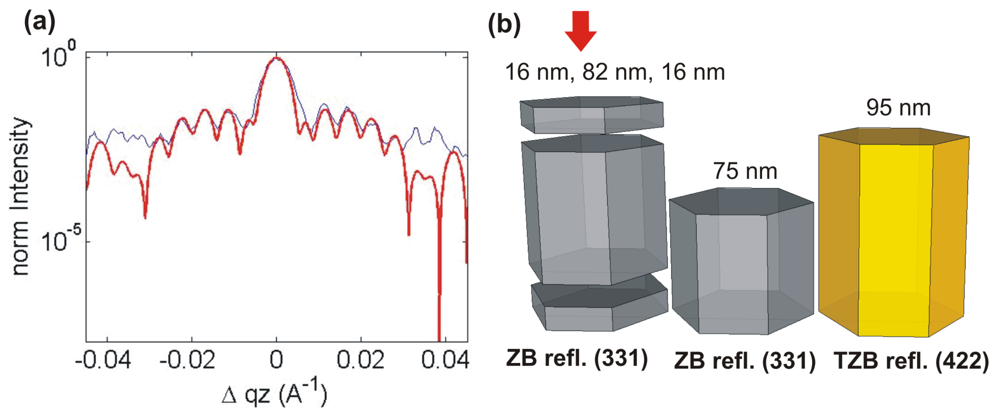

Figure 5.11: (a) The profile along q_z of multiple sets of fringes of one of the (331) signals from NW3 is shown. The experimental data (blue curve) and the model (red curve) are visible. (b) Phase structure obtained by modelling the periodicity of the fringes measured for one nanowire (NW3): the grey and yellow segments indicate ZB and TZB units, respectively. The red arrow shows the ZB units extracted from the periodicity of the fringes in (a).

glide planes. The shear stress applied mechanically during the contacting procedure results in initiation of glide systems and, therefore, may change the nature of the phase boundaries, enhancing the number of stacking faults. Another possibility, as the position of the W tip on the nanowire top surface cannot be precisely controlled at the nanometre scale, is a bending of the nanowire structure with a tilt of the ZB and TZB units with respect to each other. The sum of the total length of structural units with well measurable thickness oscillations reproduces the nominal length of the NW (about 1 μm) for NW1 and NW2 only. The other NWs show additional elongated diffraction signals (stripes) in reciprocal space without measureable thickness oscillations (figure 5.10 (b)). The extension of these stripes along q_x or q_y (with typical value ~0.02 Å^{-1}, and exceptionally ~0.06 Å^{-1} only for NW3) are much longer than $2\pi/d_{NW}$ (where d_{NW} is the nominal diameter of the NW). Therefore, these features may originate from shearing and twisting of structural sub-units as an additional result of the plastic deformation (figure 5.11 (c)). As a rough estimate of the volume affected by shear, we measured the length of these features along the in-plane components with respect to the nominal diameter of the NW, multiplied by the size of the feature along q_z. A comparison of the integrated intensities revealed to be extremely challenging due to the complex shape of the signal, which makes a clear distinction impossible. However this was successfully done for NW3 (figure 5.10), by comparing the intensity of signals 1 and 2, and gave ~ 10% difference compared to the method previously described. We suppose that each of these sheared units

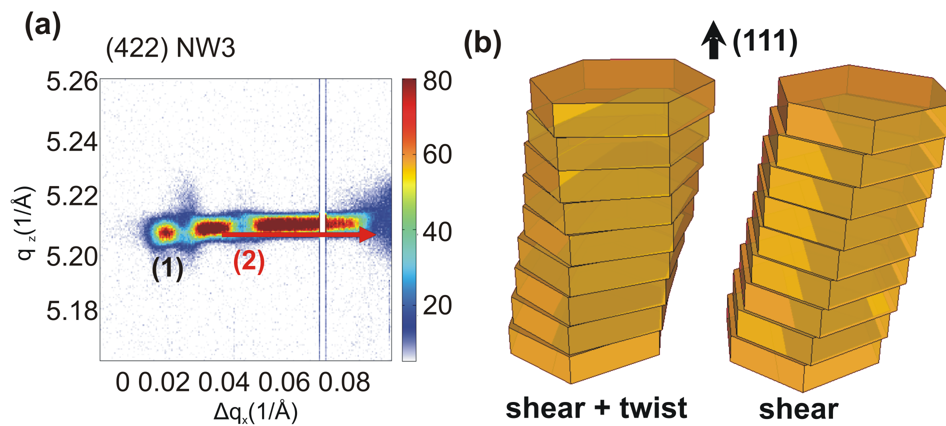

Figure 5.12: (a) RSM of NW3 for reflection (422): a defined diffraction peak (1) and an elongated diffraction signal along the q_x direction (2) without measureable thickness oscillations are visible. Feature (2) might originate from shearing and/or twisting of structural sub-units as a result of the plastic deformation. (b) Example of a pure ZB or TZB portion in sheared/twisted and sheared configurations.

is composed only of ZB or TZB sub-units respectively, according to the analyzed reflection. This gives the minimum length of the additional portion which matches fairly well the missing length of the respective NWs. The results of the presented analysis are shown in table 5.2 as *sheared portion* for the respective reflections.

5.8 The correlation

The structure and electrical information for several NWs was extracted in order to correlate the results of the V-I characterization and the X-ray analysis. The main result observed is that R_s and effective mobility μ are related to the composition of the respective NWs. In more detail, figure 5.13 shows R_s and μ as functions of the number of segments evaluated (figure 5.13 (a)) (i.e. of the number of interfaces) and of the mean length of those segments (figure 5.13 (b)). The resistance shows a monotonic increase with increasing number of segments in the NW, while no clear dependence was observed as a function of the segment length. Therefore, one may conclude that at the phase boundaries within the NWs, between the ZB and TZB units, multiple stacking faults may occur, mainly induced by the contacting procedure, and act as scattering centers for the electrical current. Figure 5.13 shows that the values extracted by methods A and B follow the same trend, and that the final result does not depend on the model

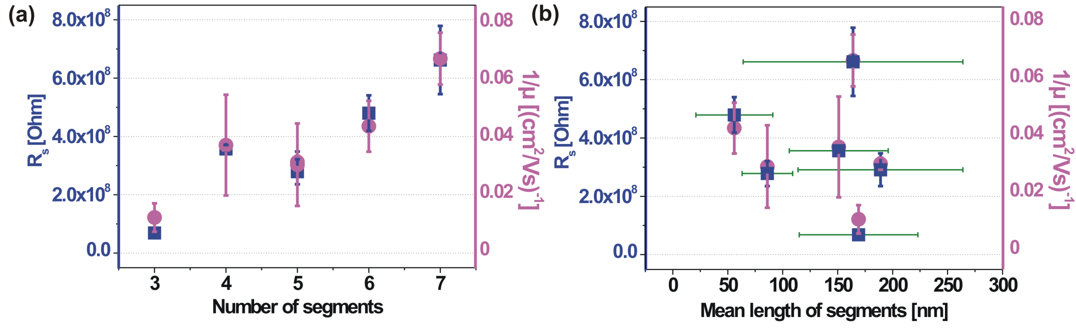

Figure 5.13: Total extracted resistance R_s and the inverse of effective mobility $1/\mu$, as functions of the number of segments (number of interfaces) (a) and the mean length of the perfect units inside the nanowires (b).

used. The trend suggested is clear in the case of NW1 and NW2. It may become questionable in the NWs including a sheared portion, as those units may be composed of several ZB and TZB units, increasing the number of active interfaces. As for most of the NWs *continuous* sheared portions were observed, either at ZB or TZB reflections, the sheared units may not contain additional structural interfaces. Nevertheless, as strain is known to affect mobility, the influence of the sheared segments on the electrical transport is open to further investigations.

5.9 Discussion on the present results and summary

The results shown here represent a successful attempt to study the correlation between structure and electrical properties of a series of single as-grown NWs made on the same objects. The method presented is a promising route for finding relationships between structure to properties of single nano-objects, where the V-I characteristics are an example. It is particularly suitable for the characterization of NWs with different sizes, phase compositions and defective crystal structures. The combination of X-ray nano-diffraction with electrical characterization allows investigation of the same as-grown nanowires. However, measurement of the same NWs in the FIB chamber and at a synchrotron beamline requires careful sample preparation, such as the setting of markers and other visible indicators for the recognition of the nano-objects. The electrical characterization shows different trends and gives different electrical parameters among the various NWs. The values presented, extracted according to the procedures described and under specific boundary conditions, do not pretend to be

absolute. As the main objective of this work was to correlate electrical and structural quantities within the measured NWs, the interpretation of the results focused on the difference in the values of resistance and effective mobility (figure 5.13). Several questions are still open and require further investigations; among them, the influence of surface states [35] and the presence of a possible piezoelectric effect during the contacting procedure [137]. The ability to detect structural damage induced by the contacting procedure in nano-objects is not trivial and has been revealed to be crucial for the overall interpretation of the electrical properties. Here, the plastic deformation detected in the structure analyzed is likely to have originated from the action of the W tip on the GaAs NW. A perturbation to the system under investigation induced by the probing device and contacting procedure is an issue to be taken into account in real devices. The impact of the plastic deformation on R_s can be estimated from the error bars of the individual points shown in figure 5.13. As a result of the structural investigation, the combination of diffraction patterns from different Bragg reflections allowed the structural composition of the different NWs to be quantified. The nano-objects inspected were composed of several ZB segments alternating between the two possible ZB orientations; and accompanied in some cases by a continuous plastically deformed portion. An additional challenge is to develop characterization methods which are non-destructive at the nano-scale, and which do not influence the measurement itself. This is to limit the inter-relations of data originating from two or more different types of measurements of the same object.

5.10 The last attempts with STM

After the X-ray measurement, an additional attempt to characterize electrically the same NWs was performed in a STM chamber in the Synchrotron Radiation Research group of Prof. Anders Mikkelsen at the University of Lund in Sweden; with the aim to reproduce the previous results. The details about the experimental configuration can be found in ref. [145]. The experimental procedure revealed to be particularly challenging. The direct identification of the nano-objects in STM mode requires a conductive surface to be probed. The mentioned condition was not satisfied, due to the insulating layer on the sample surface. In addition, as shown in figure 5.2(a), a *self consumption of the Ga droplet* at the NW top was performed during the catalyst-free MBE growth.

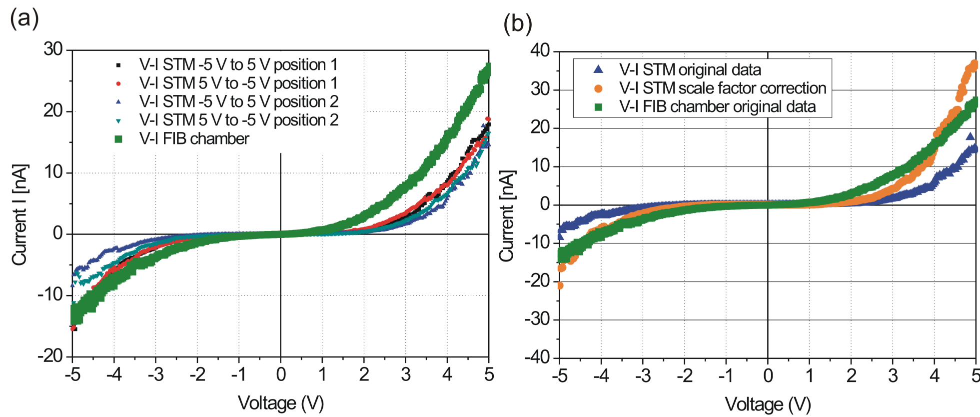

Figure 5.14: (a) The V-I curves collected with STM are compared visually with the characteristic measured in the FIB chamber (green curve) for the same NW. (b) In the shown example, the green (FIB) and blue (STM) curves follow the same trend apart from a scale factor, in this case 2.5 (orange curve).

The sample was glued with liquid indium (constituting the back contact) in an AFM/STM chamber. The sample was aligned with an AFM tungsten tip in non-contact mode, with an offset in height of ~ 600 nm above the sample surface, in order to identify the single objects without destroying them. For this purpose, a sample surface perfectly parallel to the direction of the AFM scan is required. One of the objects was successfully identified; and its top surface was scanned in STM mode to collect the tunnelling current. The tip was then approached and kept fixed on the surface by applying different pressures (not exactly quantified) during the collection of V-I curves. The pressure, likely related to the quality of the contact, was optimized until reproducible characteristics could be obtained in a range of voltage between -5 V and +5 V. Contrary to the characterization in the FIB chamber, it was possible to resolve different positions across the top section (with minimum distance ~50 nm from each other) of the same NW. The corresponding curves revealed different trends in terms of maximum current (figure 5.14(a)). However, a qualitative agreement was observed between the shape of the curves measured with STM and in the FIB chamber. For negative voltage, the curves follow the same trend (figure 5.14(b)). Only a scaling factor is required to bring them into alignment, as confirmed by the superimposition of the orange and green curves in the example shown in figure 5.14(b). For positive voltage, the agreement is less pronounced. It is worth to mention that in those types of measurements a crucial role is played by the quality of the STM tip, which may influence the final data acquisition; therefore a proof for the local dependence

of the electrical response, for example on the inner (internal core) or outer (external shell) regions of the NW, requires additional characterizations.

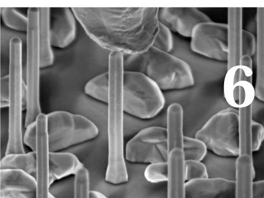

6 Strain impact of BCB polymer curing on embedded semiconductor nanostructures

In chapter 6, the XRD ensemble measurements of GaAs nanostructures embedded in a BCB based polymer matrix are presented. The presence of elastic strain in the organic polymer is revealed and associated to the thermal annealing performed during the sample preparation. The measured compressive strain can be attributed to the different thermal expansion coefficients of polymer and semiconductor. In addition it will be shown how the effect of X-ray radiation combined with the application of an external electric field results in the split of the BCB polymer chains and the polarization of the polar sub-molecules generated. This process leads to a local release of the pre-compression in the polymer with resulting strain decrease in the embedded nanostructures. Most of the elements (text and figures) presented hereafter are published in

Bussone *et al.*,*Physica Status Solidi RRL*, 8(12):1007, 2014.

6.1 BCB, an organic polymer for the planarization of nanostructures

As stated in chapter 2, in the last years, organic polymers, such as Benzocyclobutene (BCB) [97], poly(methyl) methacrylate (PMMA), and SU-8, have been commonly used as embedding media in modern electronic applications [80, 146, 44]. In particular they are suitable for large area planarization and subsequent metallization of ensembles of nanowires. Efforts have

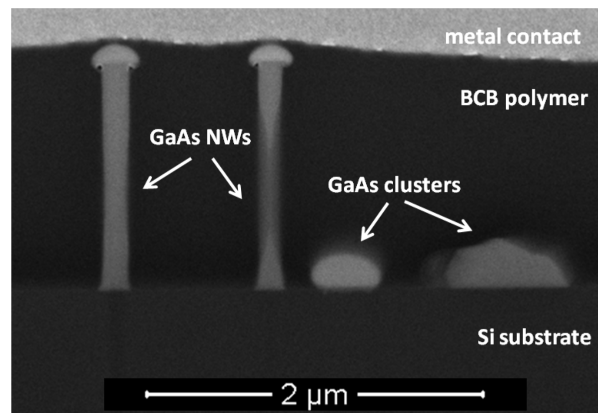

Figure 6.1: SEM image of GaAs NWs and parasitic clusters on the growth substrate, embedded in a BCB polymer layer, and covered by a metallic contact.

been invested to find the best embedding media. The performance of modern devices is nowadays limited by the signal transmission in the device itself [46]. Crucial is the dielectric constant of the chosen materials, its square root has an inverse proportionality to the velocity of the pulse propagation. Great importance was therefore attached to the development of low dielectric constant media [98]. Furthermore the chosen polymer has to withstand high temperature processes [121] with no significant degradation. From comparative studies [25] of several polymers, with the aim of determining the quality of the embedding means after the preparation process and the response to external perturbations, BCB-based polymers have been revealed to be the most suitable from structural and electrical points of view. They allow the preparation of planarized NW ensembles with a low number of voids and increased break-down voltage. However, a critical parameter that has not been considered so far is the difference in thermal expansion coefficients of BCB and the embedded semiconductor, which may give rise to strain and to degradation of the device performance.

6.2 Samples and experimental method

The BCB-based polymer belongs to the series CYCLOTENE 4000 from Dow Chemical [104]. It is a good dielectric material, with low dielectric constant ($\epsilon = 2.65$), low curing temperature, low moisture absorption, high planarization properties and wide application in GaAs electronic circuits. The synthesizing process is described in ref. [154]. It is a negative photoresist composed of a resin, a photoactive compound and a casting solvent. As shown in figure 6.1,

GaAs (111)-oriented NWs grown by MBE on a highly n-doped Si substrate (with a resistivity of $10^{-3}\Omega/cm$) are used as planarized objects. The nanowires, with mean height and diameter respectively of 1.5 μm and 150 nm, have a number density of $10^{8}cm^{-2}$. Among the NWs, the parasitic growth of GaAs clusters takes place as well (figure 6.1). The planarization procedure is described in ref. [41]; it includes the spin coating of the fluid polymer, a UV exposure of 1.3 s duration and a final thermal annealing for 30 min at 525 K. The resultant resin is insoluble in the region exposed to UV light, as the radiation leads to crosslinking of the polymer chain and an increase in the molecular weight. The last curing is crucial for the hardening of the polymer, due to further crosslinking of the polymer chain, which makes it suitable for electronic applications. Contrary to the suggested procedure [41], the etching and sonication steps were omitted, to keep the thickness of the deposited spin coated polymer ~40 nm higher than the mean length of the NWs, in order to avoid a direct electrical contact and breakdown current. Then two 10 nm Ti/150 nm Au contacts were deposited onto the front and back sides of the sample. The contact on the front side had a 0.5 mm to 1 mm diameter and the contact on the back side was covering the whole surface. X-ray investigation of the polymer-embedded nanostructures was performed on the sample, to quantify the strain state of the amorphous polymer indirectly by measuring the strain of the crystalline NWs. The prepared sample was measured using a monochromatic beam with an energy of 9 keV and 15 keV in two separated experiments with the initial aim to measure the piezoelectric effect (see section 2.4.2). The beam size was fixed to 300x300 μm^2 using a pair of motorized slits in front of the sample. The strain induced by the BCB polymer was probed at the symmetric (333), (444) and the asymmetric (422) reflections of the GaAs NWs. From the obtained RSMs, the peak profile along the wave vector transfer parallel to the [111] surface normal (q_z) was extracted to visualize the strain along the direction of growth. Furthermore, during the measurement, a static electric field was applied to the sample, in order to measure the piezo-response of the wires to an external electric field. A special sample holder in Teflon (shown in figure 6.2) was prepared in order to ensure the electrical insulation of the sample from the structure of the diffractometer. It allows the fixation of an additional Printed Circuit Board (PCB) holder (Cu coated) connected via flexible connectors to side pads, for an intuitive contacting of the top contacts of the sample.

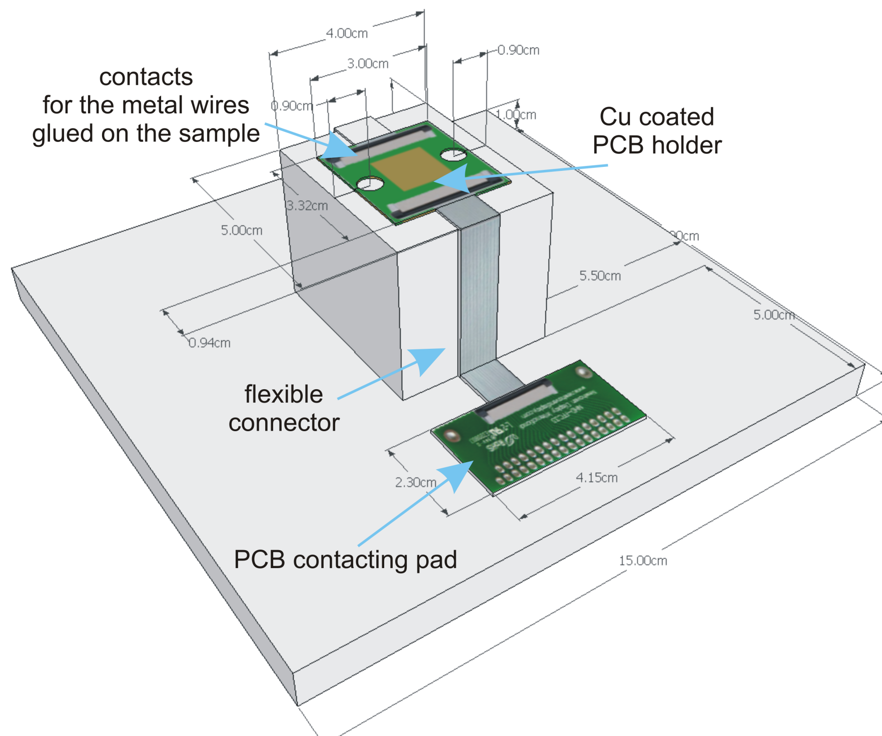

Figure 6.2: Teflon sample holder.

6.3 Elastic strain inherent to the thermal history of the fabrication method

The X-ray diffraction results suggest the presence of structural changes in the NWs, with respect to their as-grown state, due to the polymer curing. Figure 6.3 shows 2D reciprocal space maps of samples at different steps of the preparation process. Three reciprocal space maps around the (333) reflection are shown: one for the as-grown nanowires, a second for the embedded sample without the last annealing step at 525 K, and a third for an embedded sample after complete preparation; all of them in the absence of an external electric field. The most intense peak in each map corresponds to the (333) Bragg peak at $q_z = (5.780 \pm 0.002)$ Å^{-1} of the GaAs NWs. The corresponding lattice parameter is given by a ∼ 5.65 Å according to eq. 3.1 and eq. 3.5, which indicates that the NWs are fully relaxed.

Interestingly, in the third map in figure 6.3, a second diffraction signal is observed at larger q_z values ($\Delta q_z \sim 0.02$ Å^{-1}), suggesting the presence of a structural modification in the fully processed NWs. The measurement of symmetric and asymmetric reflections allows the feature

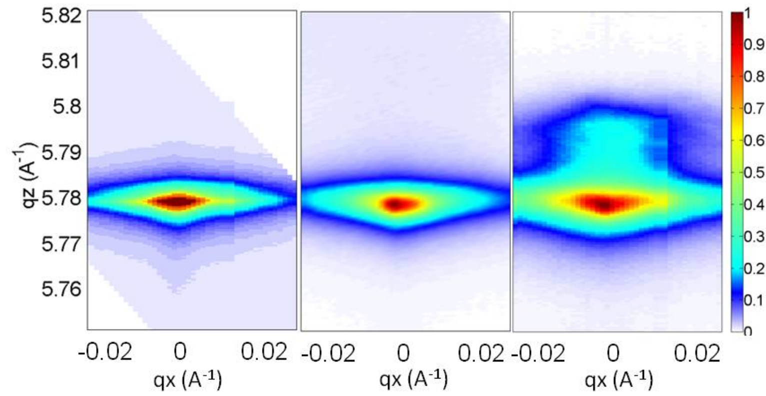

Figure 6.3: From left to right, comparison of reciprocal space intensity maps for: as-grown NWs, embedded NWs before and after last curing step. The intensity is normalized to the respective maximum in each map.

to be identified as a compressive uniaxial strain of the NW along the (111) growth direction. The peaks were deconvolved and fitted with two Lorentzians in order to determine their peak centres, $q_{z_{unstrained}}$ and $q_{z_{strained}}$, respectively. The corresponding interplanar distances $d_{z_{unstrained}}$ and $d_{z_{strained}}$ were then calculated according to eq. 3.5. In the approximation of kinematic scattering (see section 3.2), the diffracted intensity is proportional to the volume square. Therefore, the comparison of the integrated intensities of the unstrained and strained signals showed that the strained signal corresponds to less than 4% of the total scattering volume. This depends on the inhomogeneous nature of the sample, consisting of a mixture of nanowires with variable heights and crystalline clusters; and the fact that a X-ray beam with size of hundreds of μm measures average properties. In some areas of the sample, SEM measurements reveal that only 15% of the structures are actually standing NWs; and among them bent NWs and NWs emerging from the polymer layer are visible (figure 6.6). The value of strain was calculated according to eq. 3.15; it was measured at three different positions on the sample and varies between -0.1% and -0.3% (as shown in figure 6.4) before the application of the external electric field. The inhomogeneous thickness of the BCB layer and/or number density of the NWs in the different regions under the contacts explains the strain difference $\Delta\epsilon \sim 0.2\%$ of the data sets indicated as *pos1* and *pos2* in figure 6.4.

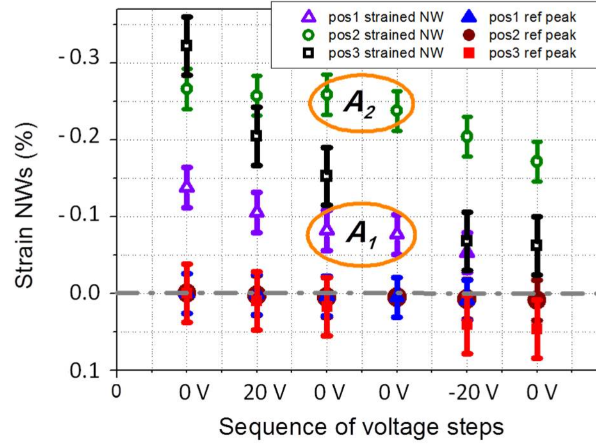

Figure 6.4: Strains values extracted from the X-ray diffraction data in three different areas on the sample. The data sets (pos 1,2,3 ref) around the zero value are calculated from the Bragg peak position of the unstrained GaAs NWs. The remaining data sets (pos 1,2,3 strained NW), calculated from the Bragg peak position of the strained NWs, show a decrease in the absolute strain during the application of the voltage cycle.

6.4 Thermal expansion coefficients and polymer curing: the FEM simulation

The strain measured in the annealed sample is induced in the nanostructures during the curing step and arises from the different thermal expansion coefficients of the polymer ($\alpha_{BCB} \sim 52{\cdot}10^{-6}/K$) and the GaAs ($\alpha_{GaAs} \sim 5.73{\cdot}10^{-6}/K$), and the subsequent change in the volume of the polymer. This is confirmed by Finite Element Modelling (FEM) simulations that have been performed to predict the strain induced by the thermal process in a (111)-oriented NW and a GaAs cluster.

The FEM simulations have been performed with COMSOL Multiphysics [30]. The used geometries represent a vertical GaAs NW with diameter 150 nm and lenght 1.5 μm, and a GaAs cluster with diameter 500 nm and height 200 nm. They were both embedded in a BCB polymer parallelepiped having base 25 μm by 25 μm and height 40 nm higher than the NW. The crystal orientation of the GaAs nano-structures was defined vertically along the [111] direction with the related oriented elasticity matrix for isotropic materials (see section 3.14). In first approach, as the interesting strain component will be along the growth axis (ϵ_{33}), no corrections for the presence of twinned ZB orientation was considered. Moreover, the absence of WZ was con-

firmed by the XRD data. In addition, SEM images showed no significant tapering in the NWs, whose diameter is kept uniform all along the NW height. The following boundary conditions have been applied: a *fixed constraint* at the bottom surface of the polymer block and the NW, due to the presence of the substrate; a *roller* at the four lateral sides of the BCB block, in order to take into account the presence of additional material free to expand or contract. The effects of the thermal expansion coefficients of the two linear elastic materials (GaAs and BCB) were simulated with the Solid Mechanics module according to equation [113]

$$\epsilon_{ij} = \alpha_{ij}\Delta T \tag{6.1}$$

where ϵ_{ij} are the strain components, ΔT is the variation of temperature and α_{ij} are the thermal expansion coefficients of the material, which according to [1] are

$$\begin{bmatrix} \alpha_{11} & 0 & 0 \\ 0 & \alpha_{11} & 0 \\ 0 & 0 & \alpha_{11} \end{bmatrix} \tag{6.2}$$

for a cubic system, with $\alpha_{11} = \alpha_{GaAs}$. The variation of the thermal coefficient of GaAs due to temperature is neglected in first approximation ($\alpha_{GaAs} = 6.5 \cdot 10^{-6}/K$ at 503 K [83]), as well as the temperature dependence of α_{BCB} (in a similar resin, CYCLOTENE 4026-46, the coefficient can get up to $60 \cdot 10^{-6}/K$ at 473 K [43]).

A first intuitive calculation, considering the one dimensional strain ϵ (see section 3.15), allows the calculation of its maximum expected value due to the different linear thermal expansion coefficients of the materials

$$\epsilon_{GaAs} - \epsilon_{BCB} = \Delta T\{\alpha_{GaAs} - \alpha_{BCB}\} \sim -0.9\%. \tag{6.3}$$

Higher reliability can be assigned to the FEM simulations, which take into account the crystallographic orientation of the material, the actual shape of the NWs and parasitic clusters, and include a two step process. A temperature variation in two consecutive steps is simulated: from 300 K (Room Temperature (RT)) to 525 K and from 525 K to 300 K (RT). The first heating

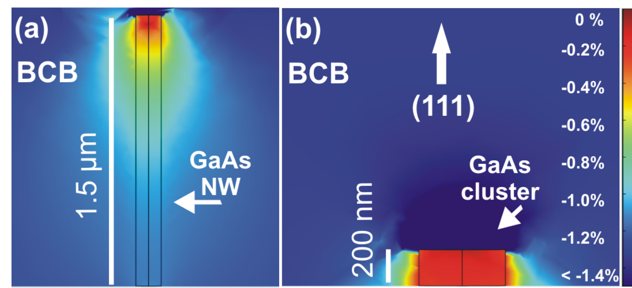

Figure 6.5: Strain distribution, along the growth axis of the NW, obtained by FEM simulations in a NW (a) and in a GaAs cluster (b).

step results in an expansion of the polymer and a consequent tensile strain along the [111] direction in the NW. The results of the first step were then used as starting values for the following one. The second cooling step originates a contraction of the polymer and results in a compressive strain along the NW growth direction (figure 6.5 (a)), in the order of $\epsilon_{sim_{NW}}$ = -0.9% (mean value). The strain gradient visible in figure 6.5 (a) is originated from the shrinkage of the polymer matrix close to the side facets of the top of the NW, which results in a relaxation of the GaAs lattice along the vertical axis. This effect is not visible in the GaAs clusters (figure 6.5 (b)), where the strain is uniform and estimated in the order of $\epsilon_{sim_{cluster}}$ = -0.1%. A value of ~ -0.3% strain is obtained with a weighted arithmetic mean, based on the observed content of 15% NWs and 85% clusters. This value is comparable to the measured strain, and the difference is likely related to the non-uniform nature of the sample. Thus bending of individual NWs (figure 6.6), voids close to the nanowire side walls and the surface, as well as the heterogeneous size distribution of the parasitic islands, change the actual geometry. The assumptions made, for the sake of simplicity, do not include the mentioned issues.

6.5 Application of an external static electric field

As second step, an external voltage was applied to the contacted regions on the cured sample and the areas were probed again with X-rays, while the voltage was changed in a cycle between V= 0 V and V= +20 V followed by a variation between V= 0 V and V= -20 V. Considering the sample thickness, the applied voltage resulted in an effective electric field ranging between $6.6 \cdot 10^5$ V/m and $1.3 \cdot 10^7$ V/m. The variation in strain as function of the applied voltage is shown in figure 6.4: the absolute strain always decreases and it is independent of the sign of

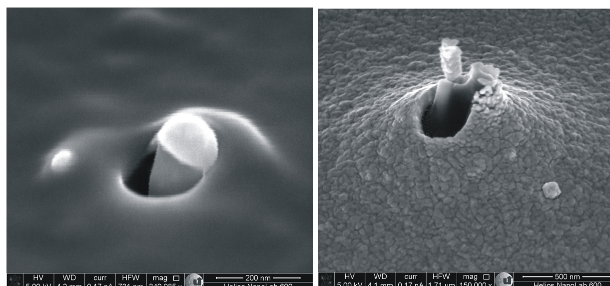

Figure 6.6: GaAs NWs emerging from the BCB polymer layer and the metal contact. Their structure is likely bent.

the electric field. Instead, a time dependence is observed by comparing the data sets *pos2* and *pos3 strained NWs*, where the calculated strain changes are (0.02±0.01) / *voltage step* for *pos2* and (0.04±0.01) / *voltage step* for *pos3*. In the present case, the strain before the application of the electric field is the same for the two cases; but the X-ray exposure time was doubled for *pos3* ($t_{exp3} = 12.6 \cdot 10^3\,s$) compared to *pos2* (and *pos1*, where $t_{exp1,2} = 6.7 \cdot 10^3\,s$). As shown in the complete voltage cycle in figure 6.4, the combined effect of X-ray radiation and the application of an electric field leads to a release of strain that is independent of the sign of the applied voltage. This can be explained as an effect of absorption that leads to radiation damage of the BCB matrix. As reported by Coffey [27], bond breaking of polymer chains is a well-known effect under soft X-ray radiation and is accompanied by a loss of mass. Here, the hard X-rays used are responsible for the breaking of C double-bonds within the non-polar BCB molecule [114], that leads to a conrotatory ring-opening reaction and the formation of polar submolecules [128, 55, 71]. If the aromaticity of the BCB benzene ring is broken, a reverse reaction is highly favored [104], and that results in a self-healing of the polymer damage induced by X-rays. The processes of X-ray induced damage and recombination take place on a very fast time scale, therefore they do not result in a change of the polymer structure. In contrast, a change in the polymer structure and its elastic properties occur when an electric field is applied simultaneously under X-ray irradiation. Consequently, the electric field is responsible for the reorientation of the decomposed polymer chains and acts against the preferred crosslinking. The damage caused by X-rays and the dipole orientation, due to the electric field, affects the hardness of the polymer, and for that reason reduces the compressive stress acting at the NWs structure. When the electric field is brought back to zero, the strain remains constant (as can be observed in figure 6.4 at position A1 and A2 of the *pos1* and *pos2*

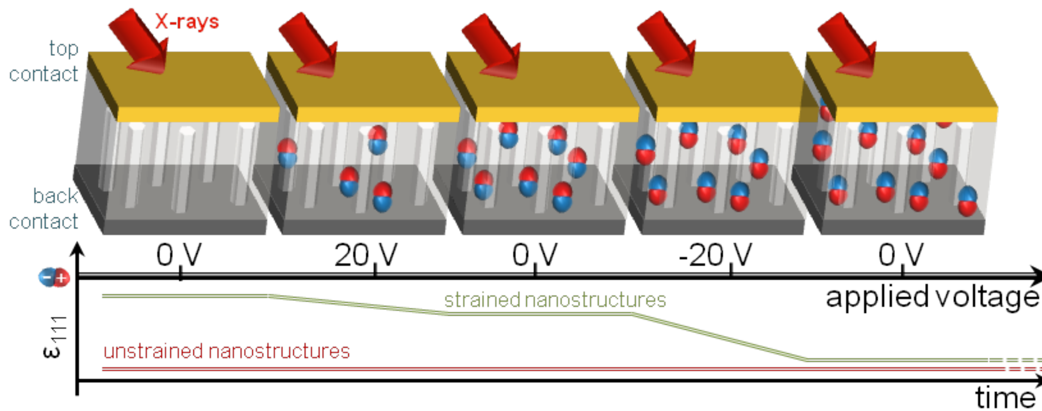

Figure 6.7: Sketch of the evolution of the strain state in the BCB embedded NWs under X-ray illumination and in function of the applied voltage and time.

strained NWs data sets). This behaviour is consistent with existing reports about the electret features of BCB thin films [133], known for their ability to keep the polarization state. Finally, the direction of the polarizing field does not affect the strain release. With a reversed field, the orientation of the dipoles is inverted, but the recombination of the polar submolecules is still unfavorable (figure 6.7). This effect was found to persist for up to five hours. Additional characterization is needed to understand whether the polymer changes are reversible or not. The decoupled application of an electric field and an extended exposure to X-rays have been tested as well, and revealed no measurable effects. Within this context, we can exclude the possibility of detecting lattice expansion due to the piezoelectric effect, which is expected to be one order of magnitude smaller than the strain state detected.

6.6 Summary

The thermal processing of the BCB-based polymer up to 525 K is responsible for the presence of an initial strain in the nanostructures probed via X-ray diffraction. The local release of the pre-compression in the polymer with resulting strain decrease in the embedded NWs was observed under the effect of X-ray radiation, combined with the application of a static external electric field. It originates from the split of the BCB polymer chains and the polarization of the polar sub-molecules generated.

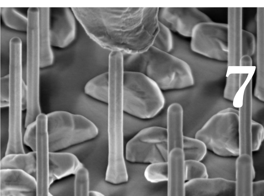

7 Conclusions

The conclusions can be resumed in three main outcomes.

The scientific life of a NW starts with its growth.

The arrangement of single nanowires on their growth substrate is nowadays required in electronic and optical devices. Gold implantation by FIB was confirmed to be an effective method for the growth and positioning of GaAs nanowires on GaAs substrates. The measurement of single GaAs nanowires was successfully carried out using n-XRD in non-coplanar GID geometry for the first time. Despite the strong influence of parasitic growth on the sample surface, the NWs exhibited a twist about the growth axis with respect to the substrate, and showed no significant strain state along the height of the NW. Moreover the technique, sensitive to the top few layers near the surface, revealed the presence of a gradual in-plane compressive strain in the substrate, on average -0.4%, measured at different distances from the area subject to Au implantation. This provides valuable information about the growth; and highlights the potential of the characterization technique used, which constitutes a new source of information.

Afterwards, the investigation of the physical response at the nano-scale becomes relevant.

A correlation was found at the nanoscale between the electrical response and the structure of single GaAs nanowires in their as-grown geometry for the first time. N-XRD revealed the polytype composition of single NWs, which were shown to be composed of different numbers

of ZB and TZB units stacked above each other along the growth axis. The electrical characteristic of the same NWs were measured in a SEM-FIB chamber, showing significant differences among them. A careful analysis of the role played by the contacts was carried out, and allowed the extraction of electrical parameters such as the resistance and the effective mobility. The difference of those parameters in the NWs measured was then correlated with the number of interfaces along the NW growth axis. Those interfaces were revealed to be scattering points for the current flowing into the device. The successful combination of the two experimental techniques had to deal with the damage induced in the NW structure, due to the indentation of the contacting tip on the top of the nanowire. This resulted in a complex slip, shear and twist deformation, whose marks have been observed in the diffraction data. The combination of the techniques presented is a powerful tool, which may be applied in the characterization of different materials and NWs heterostructures.

In the end, the NWs arrive at the final stage of their scientific path: their application in real devices.

The embedding of GaAs nanostructures in a polymer matrix is nowadays very common in electronic devices. XRD on ensemble NWs indirectly revealed the presence of a strain state in the amorphous polymer due to the thermal processing. The nano-structures were shown to be affected by a compressive strain of the order of -0.3%. This was in line with the FEM simulations, which, in the ideal case, predict a strain of the same order of magnitude (-0.9%). In addition, the sample was contacted and the application of a static electric field was carried out *in-situ* under X-ray illumination in order to investigate the indirect piezo-electric response in the GaAs nanostructure. Unfortunately, the investigation was not possible in the present state, as the procedure mentioned turned out to be responsible for a change in the initial strain state one order of magnitude greater than the piezo-electric response expected. The modification detected was due to the split and reorientation of the polymer into polar sub-molecules, which resulted in a release of the strain state.

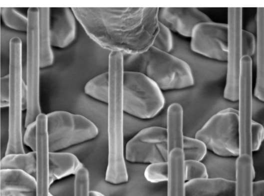

Bibliography

[1] S. Adachi. *Physical Properties of III-V Semiconductor Compounds*. Wiley-Interscience publication. Wiley, 1992.

[2] M. Ahmetoglu and S.K. Akay. Determination of the parameters for the back-to-back switched schottky barrier structures. *Current Applied Physics*, 10(2):652, 2010.

[3] J. Als-Nielsen and D. McMorrow. *Elements of modern x-ray physics*. Wiley, New York, NY, 2001.

[4] S. Ambrosini, M. Fanetti, V. Grillo, A. Franciosi, and S. Rubini. Vapor-liquid-solid and vapor-solid growth of self-catalyzed GaAs nanowires. *AIP Advances*, 1(4):042142, 2011.

[5] G. Arlt and P. Quadflieg. Piezoelectricity in III-V compounds with a phenomenological analysis of the piezoelectric effect. *Physica Status Solidi (b)*, 25(1):323, 1968.

[6] A. Authier. *Dynamical Theory of X-ray Diffraction*. IUCr Crystallographic Symposia Series. Oxford University Press, 2001.

[7] T. Ba Hoang, A. F. Moses, L. Ahtapodov, H. Zhou, D. L. Dheeraj, A. T. J. van Helvoort, B.-O. Fimland, and H. Weman. Engineering parallel and perpendicular polarized photoluminescence from a single semiconductor nanowire by crystal phase control. *Nano Letters*, 10(8):2927, 2010.

[8] J. Bardeen. Surface States and Rectification at a Metal Semi-Conductor Contact. *Physical Review*, 71:717, 1947.

[9] J. Baruchel, J.-L. Hodeau, M.S. Lehmann, J.-R. Regnard, and C. Schlenker. *Neutron and Synchrotron Radiation for Condensed Matter Studies*. Les Editions de Physique, Les Ulis, 1994.

[10] D. C. Bell, Y. Wu, C. J. Barrelet, S. Gradečak, J. Xiang, B. P. Timko, and C. M. Lieber. Imaging and analysis of nanowires. *Microscopy Research and Technique*, 64(5-6):373, 2004.

[11] A. Biermanns, S. Breuer, A. Davydok, L. Geelhaar, and U. Pietsch. Structural polytypism and residual strain in GaAs nanowires grown on Si(111) probed by single-nanowire X-ray diffraction. *Journal of Applied Crystallography*, 45(2):239, 2012.

[12] A. Biermanns, A. Davydok, H. Paetzelt, A. Diaz, V. Gottschalch, T.l H. Metzger, and U. Pietsch. Individual GaAs nanorods imaged by coherent X-ray diffraction. *Journal of Synchrotron Radiation*, 16(6):796, 2009.

[13] J.P. Biersack and L.G. Haggmark. A monte carlo computer program for the transport of energetic ions in amorphous targets. *Nuclear Instruments and Methods*, 174(1–2):257, 1980.

[14] J. S. Blakemore. Semiconducting and other major properties of gallium arsenide. *Journal of Applied Physics*, 53:123, 1982.

[15] S. Breuer. *Molecular Beam Epitaxy of GaAs nanowires and their suitability for optoelectronic applications*. PhD thesis, Humboldt-Universität zu Berlin, 2011.

[16] S. Cahangirov and S. Ciraci. A first-principles systematic study of GaAs nanowires. *Arxiv*, 2010.

[17] A. Casadei, J. Schwender, E. Russo-Averchi, D. Rüffer, M. Heiss, E. Alarcó-Lladó, F. Jabeen, M. Ramezani, K. Nielsch, and A. Fontcuberta i Morral. Electrical transport in C-doped GaAs nanowires: surface effects. *Physica Status Solidi (RRL) – Rapid Research Letters*, 7(10):890, 2013.

[18] A. Cavallini and L. Polenta. 3 - Electrical characterization of nanostructures. In Carlo Lamberti, editor, *Characterization of Semiconductor Heterostructures and Nanostructures*, page 55. Elsevier, Amsterdam, 2008.

[19] G. A. Chahine, M.-I. Richard, R. A. Homs-Regojo, T. N. Tran-Caliste, D. Carbone, V. L. R. Jacques, R. Grifone, P. Boesecke, J. Katzer, I. Costina, H. Djazouli, T. Schroeder, and T. U. Schülli. Imaging of strain and lattice orientation by quick scanning X-ray microscopy combined with three-dimensional reciprocal space mapping. *Journal of Applied Crystallography*, 47(2):762, 2014.

[20] C. J. Chang-Hasnain. Nanolasers grown on silicon. In *Optical Fiber Communication Conference*, page OW1G.1. Optical Society of America, 2012.

[21] T. Cheiwchanchamnangij, T. Birkel, W. R. L. Lambrecht, and Efros A. L. Optical dielectric functions of III-V semiconductors in wurtzite phase. *Materials Science Forum Vols.*, 717-720:565, 2012.

[22] J. Chen, G. Conache, M.-E. Pistol, S. M. Gray, M.s T. Borgstrom, H. Xu, H. Q. Xu, L. Samuelson, and U. Håkanson. Probing strain in bent semiconductor nanowires with Raman spectroscopy. *Nano Letters*, 10(4):1280, 2010.

[23] Z.-G. Chen, G. Han, L. Yang, L. Cheng, and J. Zou. Nanostructured thermoelectric materials: Current research and future challenge. *Progress in Natural Science: Materials International*, 22(6):535, 2012.

[24] S.K. Cheung and N. W. Cheung. Extraction of schottky diode parameters from forward current voltage characteristics. *Applied Physics Letters*, 49(2):85, 1986.

[25] A. C. E. Chia and R. R. LaPierre. Contact planarization of ensemble nanowires. *Nanotechnology*, 22(24):245304, 2011.

[26] C. D. Child. Discharge From Hot CaO. *Phys. Rev. (Series I)*, 32:492, 1911.

[27] T. Coffey, S.G. Urquhart, and H. Ade. Characterization of the effects of soft X-ray irradiation on polymers . *Journal of Electron Spectroscopy and Related Phenomena*, 122(1):65, 2002.

[28] C. Colombo, M. Heiβ, M. Gratzel, and A. Fontcuberta i Morral. Gallium arsenide pin radial structures for photovoltaic applications. *Applied Physics Letters*, 94(17):173108, 2009.

[29] C. Colombo, D. Spirkoska, M. Frimmer, G. Abstreiter, and A. Fontcuberta i Morral. Ga-assisted catalyst-free growth mechanism of GaAs nanowires by molecular beam epitaxy. *Phys. Rev. B*, 77:155326, 2008.

[30] Inc. Comsol. Comsol multiphysics, http://www.comsol.it/, 2014.

[31] S.N. Das, J. P. Kar, J.H. Choi, K.J. Moon, T.I Lee, and J.M. Myoung. Electrical characterization of single nanowire based ZnO Schottky diodes. In *Nanoelectronics Conference (INEC), 2010 3rd International*, page 1197, 2010.

[32] A. De and C.E. Pryor. Optical dielectric functions of III-V semiconductors in wurtzite phase. *Phys. Rev. B*, 81:155210, 2012.

[33] A. De and Craig E. Pryor. Predicted band structures of III-V semiconductors in the wurtzite phase. *Phys. Rev. B*, 81:155210, 2010.

[34] M. De Luca, G. Lavenuta, A. Polimeni, S. Rubini, V. Grillo, F. Mura, A. Miriametro, M. Capizzi, and F. Martelli. Excitonic recombination and absorption in $In_xGa_{1-x}As/GaAs$ heterostructure nanowires. *Phys. Rev. B*, 87:235304, 2013.

[35] O. Demichel, M. Heiss, J.l Bleuse, H. Mariette, and A. Fontcuberta i Morral. Impact of surfaces on the optical properties of GaAs nanowires. *Applied Physics Letters*, 97(20):201907, 2010.

[36] D. L. Dheeraj, G. Patriarche, H. Zhou, T. B. Hoang, A. F. Moses, S. Grønsberg, A. T. J. van Helvoort, B.-O. Fimland, and H. Weman. Growth and characterization of wurtzite GaAs nanowires with defect-free zinc blende GaAsSb inserts. *Nano Letters*, 8(12):4459, 2008.

[37] D.L. Dheeraj, G. Patriarche, H. Zhou, J.C. Harmand, H. Weman, and B.O. Fimland. Growth and structural characterization of GaAs/GaAsSb axial heterostructured nanowires. *Journal of Crystal Growth*, 311(7):1847, 2009.

[38] A. Diaz, C. Mocuta, J. Stangl, M. Keplinger, T. Weitkamp, F. Pfeiffer, C. David, T. H. Metzger, and G. Bauer. Coherence and wavefront characterization of Si-111 monochromators using double-grating interferometry. *Journal of Synchrotron Radiation*, 17(3):299, 2010.

[39] A. Diaz, C. Mocuta, J. Stangl, B. Mandl, C. David, J. Vila-Comamala, V. Chamard, T. H. Metzger, and G. Bauer. Coherent diffraction imaging of a single epitaxial InAs nanowire using a focused x-ray beam. *Phys. Rev. B*, 79:125324, 2009.

[40] K. A. Dick, C. Thelander, L. Samuelson, and P. Caroff. Crystal Phase Engineering in Single InAs Nanowires. *Nano Letters*, 10(9):3494, 2010.

[41] E. Dimakis, U. Jahn, M. Ramsteiner, A. Tahraoui, J. Grandal, X. Kong, O. Marquardt, A. Trampert, H. Riechert, and L. Geelhaar. Coaxial Multishell (In,Ga)As/GaAs Nanowires for Near-Infrared Emission on Si Substrates. *Nano Letters*, 14(5):2604, 2014.

[42] H. Dosch, B. W. Batterman, and D. C. Wack. Depth-controlled grazing-incidence diffraction of synchrotron X radiation. *Phys. Rev. Lett.*, 56:1144, 1986.

[43] Dow. CYCLOTENE* 4026-46 Resin Temperature Dependent CTE, http://www.dow.com/cyclotene/solution/ctetemp.htm, 2014.

[44] X. Duan, Y. Huang, R. Agarwal, and C. M. Lieber. Single-nanowire electrically driven lasers. *Nature*, 421:241–245, 2003.

[45] Dubrovskii, V. G. and Sibirev, N. V. and Harmand, J. C. and Glas, F. Growth kinetics and crystal structure of semiconductor nanowires. *Phys. Rev. B*, 78:235301, 2008.

[46] N.R.C.C.P.S. Engineering. *Polymer Science and Engineering: The Shifting Research Frontiers.* National Academy Press, 1994.

[47] P. P. Ewald. Introduction to the dynamical theory of X-ray diffraction. *Acta Crystallographica Section A*, 25(1):103, 1969.

[48] V. T. Fauske, D. C. Kim, A. M. Munshi, D. L. Dheeraj, B.-O. Fimland, H. Weman, and A. T. J. van Helvoort. In-situ electrical and structural characterization of individual GaAs nanowires. *Journal of Physics: Conference Series*, 522(1):012080, 2014.

[49] V. Favre-Nicolin, F. Mastropietro, J. Eymery, D. Camacho, Y. M. Niquet, B. M. Borg, M. E. Messing, L.-E. Wernersson, R. E. Algra, E. P. A. M. Bakkers, T. H. Metzger, R. Harder, and I. K. Robinson. Analysis of strain and stacking faults in single nanowires using Bragg coherent diffraction imaging. *New Journal of Physics*, 12(3):035013, 2010.

[50] J. Gierak, A. Madouri, E. Bourhis, L. Travers, D. Lucot, and J. C. Harmand. Focused gold ions beam for localized epitaxy of semiconductor nanowires. *Microelectron. Eng.*, 87(5-8):1386, 2010.

[51] F. Glas, J. C. Harmand, and G. Patriarche. Why does wurtzite form in nanowires of III-V zinc blende semiconductors? *Physical Review Letters*, 99(14):146101, 2007.

[52] M. J. Gordon, T. Baron, F. Dhalluin, P. Gentile, and P. Ferret. Size effects in mechanical deformation and fracture of cantilevered silicon nanowires. *Nano Letters*, 9(2):525, 2009.

[53] A. Guinier. *X-ray Diffraction in Crystals, Imperfect Crystals, and Amorphous Bodies*. Dover Books on Physics Series. Dover, 1994.

[54] R. N. Hall. Electron-hole recombination in germanium. *Phys. Rev.*, 87:387, 1952.

[55] B. Halton. From small rings to big things: benzocyclobutenes and high performance polymers. *Chemistry in New Zealand*, page 155, 2008.

[56] K. Haraguchi, T. Katsuyama, and K. Hiruma. Polarization dependence of light emitted from GaAs pn junctions in quantum wire crystals. *Journal of Applied Physics*, 75(8), 1994.

[57] J. C. Harmand, G. Patriarche, N. Péré-Laperne, M-N. Mérat-Combes, L. Travers, and F. Glas. Analysis of vapor-liquid-solid mechanism in Au-assisted GaAs nanowire growth. *Appl. Phys. Lett.*, 87:203101, 2005.

[58] P. Harrison. *Quantum Wells, Wires and Dots: Theoretical and Computational Physics of Semiconductor Nanostructures*. Wiley, 2005.

[59] P. Hiralal, H. E. Unalan, and G. A. J. Amaratunga. Nanowires for energy generation. *Nanotechnology*, 23(19):194002, 2012.

[60] M. Hjort, S. Lehmann, J. Knutsson, R. Timm, D. Jacobsson, E. Lundgren, K.A. Dick, and A. Mikkelsen. Direct Imaging of Atomic Scale Structure and Electronic Properties of GaAs Wurtzite and Zinc Blende Nanowire Surfaces. *Nano Letters*, 13(9):4492, 2013.

[61] M. Hocevar, L. T. Thanh Giang, R. Songmuang, M. den Hertog, L. Besombes, J. Bleuse, Y.-M. Niquet, and N. T. Pelekanos. Residual strain and piezoelectric effects in passivated GaAs/AlGaAs core-shell nanowires. *Applied Physics Letters*, 102(19), 2013.

[62] N. Hrauda, J. Zhang, E. Wintersberger, T. Etzelstorfer, B. Mandl, J. Stangl, D. Carbone, V. Holy, V. Jovanovic, C. Biasotto, L. K. Nanver, J. Moers, D. Grutzmacher, and G. Bauer. X-ray Nanodiffraction on a Single SiGe Quantum Dot inside a Functioning Field-Effect Transistor. *Nano Letters*, 11(7):2875, 2011.

[63] C.-H. Hsu, Q. Wang, X. Tao, and Y. Gu. Electrostatics and electrical transport in semiconductor nanowire schottky diodes. *Applied Physics Letters*, 101(18):183103, 2012.

[64] M. H. Huang, S. Mao, H. Feick, H. Yan, Y. Wu, H. Kind, E. Weber, R. Russo, and P. Yang. Room-temperature ultraviolet nanowire nanolasers. *Science*, 292:1897, 2001.

[65] ID01-ESRF. Upgrade program - Phase I - UPBL conceptual desing report. UPBL1: Diffraction imaging for nano-analysis. Technical report, ESRF, 2010.

[66] Ioffe. Gaas, http://www.ioffe.ru/sva/nsm/semicond/gaas/, 2014.

[67] IUCr. Report of the Executive Committee for 1991. *Acta Crystallographica Section A*, 48(6):922, 1992.

[68] V. L. R. Jacques, D. Carbone, R. Ghisleni, and L. Thilly. Counting dislocations in microcrystals by coherent x-ray diffraction. *Phys. Rev. Lett.*, 111:065503, 2013.

[69] U. Jahn, J. Lähnemann, C. Pfüller, O. Brandt, S. Breuer, B. Jenichen, M. Ramsteiner, L. Geelhaar, and H. Riechert. Luminescence of GaAs nanowires consisting of wurtzite and zinc-blende segments. *Physical Review B: Solid State*, 85:045323, 2012.

[70] K. Jefimovs, O. Bunk, F. Pfeiffer, D. Grolimund, J.F. van der Veen, and C. David. Fabrication of fresnel zone plates for hard x-rays. *Microelectronic Engineering*, 84(5–8):1467, 2007.

[71] F. R. Jensen and W. E. Coleman. Unsaturated four-membered ring compounds. ii. 1,2-diphenylbenzocyclobutene, a compound having unusual reactivity. *Journal of the American Chemical Society*, 80(22):6149, 1958.

[72] H. J. Joyce, C. J. Docherty, Q. Gao, H. H. Tan, C. Jagadish, J. Lloyd-Hughes, L. M. Herz, and M. B. Johnston. Electronic properties of GaAs, InAs and InP nanowires studied by terahertz spectroscopy. *Nanotechnology*, 24(21):214006, 2013.

[73] A Tektronix Company Keithley. 4200-scs parameter analyzer, http://www.keithley.com/products/dcac/currentvoltage/4200scs/, 2014.

[74] M. Keplinger, T. Mårtensson, J. Stangl, E. Wintersberger, B. Mandl, D. Kriegner, V. Holý, G. Bauer, K. Deppert, and L. Samuelson. Structural investigations of coreshell nanowires using grazing incidence x-ray diffraction. *Nano Letters*, 9(5):1877, 2009.

[75] B. Ketterer, M. Heiss, E. Uccelli, J. Arbiol, and A. Fontcuberta i Morral. Untangling the electronic band structure of wurtzite GaAs nanowires by resonant Raman spectroscopy. *ACS Nano*, 5(9):7585, 2011.

[76] C. Kirchlechner, P.J. Imrich, W. Grosinger, M.W. Kapp, J. Keckes, J.S. Micha, O. Ulrich, O. Thomas, S. Labat, C. Motz, and G. Dehm. Expected and unexpected plastic behavior at the micron scale: An in situ laue tensile study. *Acta Materialia*, 60(3):1252, 2012.

[77] Nanotechnik Kleindiek. Micromanipulator for electron microscopy, http://www.nanotechnik.com/mm3a-em.html, 2014.

[78] S. Korte, M. Steidl, W. Prost, V. Cherepanov, B. Voigtländer, W. Zhao, P. Kleinschmidt, and T. Hannappel. Resistance and dopant profiling along freestanding GaAs nanowires. *Applied Physics Letters*, 103(14):143104, 2013.

[79] D. Kriegner, C. Panse, B. Mandl, K. A. Dick, M. Keplinger, J. M. Persson, P. Caroff, D. Ercolani, L. Sorba, F. Bechstedt, J. Stangl, and G. Bauer. Unit Cell Structure of Crystal Polytypes in InAs and InSb Nanowires. *Nano Letters*, 11(4):1483, 2011.

[80] H. I. Krogstrup, P. Jørgensen, M. Heiss, O. Demichel, J. V Holm, M. Aagesen, J. Nygard, and A. Fontcuberta i Morral. Single-nanowire solar cells beyond the shockley-queisser limit. *Nature Photonics*, 7(4):306, 2013.

[81] P. Krogstrup, R. Popovitz-Biro, E. Johnson, M. H.l Madsen, J. Nygård, and H. Shtrikman. Structural Phase Control in Self-Catalyzed Growth of GaAs Nanowires on Silicon (111). *Nano Letters*, 10(11):4475, 2010.

[82] P. Kusch, S. Breuer, M. Ramsteiner, L. Geelhaar, H. Riechert, and S. Reich. Band gap of wurtzite GaAs: A resonant Raman study. *Phys. Rev. B*, 86:075317, 2012.

[83] National Physical Laboratory. Thermal expansion, http://www.kayelaby.npl.co.uk/general_physics/2_3/2_3_5.html, 2014.

[84] T. Lafford. Simple guide to writing and presenting in English, https:// simpleguideto-english.worpdpress.com, 2014.

[85] I. Langmuir. The effect of space charge and residual gases on thermionic currents in high vacuum. *Phys. Rev.*, 2:450, 1913.

[86] R.R. LaPierre. Numerical model of current-voltage characteristics and efficiency of GaAs nanowire solar cells. *Journal of Applied Physics*, 109(3):034311, 2011.

[87] Y. H. Lee, L. Fu, Z. Li, S. Breuer, P. Parkinson, H. Tan, and C. Jagadish. Nanowire solar cells for next-generation photovoltaics. *SPIE*, 2013.

[88] R. Leitsmann and F. Bechstedt. Surface inuence on stability and structure of hexagon-shaped III-V semiconductor nanorods. *Journal of Applied Physics*, 102(8):063528, 2007.

[89] F. Leonard and A. A. Talin. Electrical contacts to one- and two-dimensional nanomaterials. *Nat Nano*, 6(12):773, 2011.

[90] F. Leonard, A. A. Talin, B. S. Swartzentruber, and S. T. Picraux. Diameter-dependent electronic transport properties of Au-catalyst/Ge-nanowire schottky diodes. *Phys. Rev. Lett.*, 102:106805, 2009.

[91] T. Li, L. Gao, W. Lei, L. Guo, T. Yang, Y. Chen, and Z. Wang. Raman study on zinc-blende single InAs nanowire grown on Si (111) substrate. *Nanoscale Research Letters*, 8(1):27, 2013.

[92] F. Lu, T.-T. D. Tran, W. S. Ko, K. W. Ng, R. Chen, and C. Chang-Hasnain. Nanolasers grown on silicon-based mosfets. *Opt. Express*, 20(11):12171, 2012.

[93] E. Luna, J. Grandal, E. Gallardo, J. M. Calleja, M. Á. Sánchez-García, E. Calleja, and A. Trampert. Investigation of III–V nanowires by plan-view transmission electron microscopy: InN case study. *Microscopy and Microanalysis*, 20:1471, 2014.

[94] O. Madelung. *Semiconductors: Data HandbookSpringer.* 2004.

[95] V. R. Manfrinato, L. Zhang, D. Su, H. Duan, R. G. Hobbs, E. A. Stach, and K. K. Berggren. Resolution limits of electron-beam lithography toward the atomic scale. *Nano Letters*, 13(4):1555, 2013.

[96] S. O. Mariager, S. L. Lauridsen, Sørensen C. B., A. Dohn, P. R. Willmott, J. Nygård, and R. Feidenhans'l. Stages in molecular beam epitaxy growth of GaAs nanowires studied by x-ray diffraction. *Nanotechnology*, 21(11):115603, 2010.

[97] G. Mariani, A. C. Scofield, C.-H. Hung, and D. L. Huffaker. GaAs nanopillar-array solar cells employing in situ surface passivation. *Nat Commun*, 4:1497, 2013.

[98] S. J. Martin, J. P. Godschalx, M. E. Mills, E. O. Shaffer, and P. H. Townsend. Development of a low-dielectric-constant polymer for the fabrication of integrated circuit interconnect. *Advanced Materials*, 12(23):1769, 2000.

[99] G. Martínez-Criado, A. Homs, B. Alén, J. A. Sans, J. Segura-Ruiz, A. Molina-Sánchez, J. Susini, J. Yoo, and G.-C. Yi. Probing quantum confinement within single core–multishell nanowires. *Nano Letters*, 12(11):5829, 2012.

[100] G. Martínez-Criado, J. Segura-Ruiz, B. Alén, J. Eymery, A. Rogalev, R. Tucoulou, and A. Homs. Exploring single semiconductor nanowires with a multimodal hard x-ray nanoprobe. *Advanced Materials*, 2014.

[101] F. Mastropietro. *Imagerie de Nanofils Uniques par Diffraction Cohèrente des Rayons X.* PhD thesis, Université de Grenoble, 2012.

[102] MathWorks. Matlab, http://www.mathworks.fr/products/matlab/, 2014.

[103] B. Mayer, D.l Rudolph, J. Schnell, S. Morkötter, J. Winnerl, J. Treu, K. Müller, G. Bracher, G. Abstreiter, G. Koblmüller, and J. J. Finley. Lasing from individual GaAs-AlGaAs core-shell nanowires up to room temperature. *Nature Communications*, 4:2931, 2013.

[104] G. Mehta and S. Kotha. Recent chemistry of benzocyclobutenes. *Tetrahedron*, 57(4):625, 2001.

[105] M. A. Migliorato, D. Powell, A. G. Cullis, T. Hammerschmidt, and G. P. Srivastava. Composition and strain dependence of the piezoelectric coefficients in In_xGa_1-xAs alloys. *Phys. Rev. B*, 74:245332, 2006.

[106] M. Minary-Jolandan, R. A. Bernal, I. Kuljanishvili, V. Parpoil, and H. D. Espinosa. Individual GaN Nanowires Exhibit Strong Piezoelectricity in 3D. *Nano Letters*, 12:970, 2012.

[107] C. Mocuta, J. Stangl, K. Mundboth, T. H. Metzger, G. Bauer, I. A. Vartanyants, M. Schmidbauer, and T. Boeck. Beyond the ensemble average: X-ray microdiffraction analysis of single SiGe islands. *Phys. Rev. B*, 77:245425, 2008.

[108] N.F. Mott and R.W. Gurney. *Electronic Processes in Ionic Crystals - Second Edition*. International Series of Monographs on Physics. Oxford, 1948.

[109] T. Mårtensson, W. Borgstrom, M.and Seifert, B. J. Ohlsson, and L. Samuelson. Fabrication of individually seeded nanowire arrays by vapour–liquid–solid growth. *Nanotechnology*, 14:1255, 2003.

[110] T. Mårtensson, P. Carlberg, M. Borgström, L. Montelius, W. Seifert, and L. Samuelson. Nanowire arrays defined by nanoimprint lithography. *Nano Letters*, 4(4):699, 2004.

[111] S. Muensit. *Piezoelectric coefficients of gallium arsenide, gallium nitride and aluminium nitride*. PhD thesis, Australia, Macquarie University, 1999.

[112] S. B. Nam, D. C. Reynolds, C. W. Litton, R. J. Almassy, T. C. Collins, and C. M. Wolfe. Free-exciton energy spectrum in GaAs. *Phys. Rev. B*, 13:761, 1976.

[113] J.F. Nye. *Physical properties of crystals: their representation by tensors and matrices*. Clarendon Press, 1972.

[114] K. Nygård, S. Gorelick, J. Vila-Comamala, E. Färm, A. Bergamaschi, A. Cervellino, F. Gozzo, B. D. Patterson, M. Ritala, and C. David. Beam-induced damage on diffractive hard X-ray optics. *Journal of Synchrotron Radiation*, 17(6):786, 2010.

[115] F. A. Padovani and R. Stratton. Field and thermionic-field emission in Schottky barriers. *Solid State Electronics*, 9:695, 1966.

[116] C. Panse, D. Kriegner, and F. Bechstedt. Polytypism of GaAs, InP, InAs, and InSb: An ab initio study. *Phys. Rev. B*, 84:075217, 2011.

[117] U. Pietsch, V. Holy, and T. Baumbach. *High-Resolution X-Ray Scattering: From Thin Films to Lateral Nanostructures.* Advanced Texts in Physics. Springer, 2004.

[118] F. A. Ponce and D. P. Bour. Nitride-based semiconductors for blue and green light-emitting devices. *Nature*, 386:351, 1997.

[119] C. Ponchut, J. M. Rigal, J. Clément, E. Papillon, A. Homs, and S. Petitdemange. MAXIPIX, a fast readout photon-counting X-ray area detector for synchrotron applications. *Journal of Instrumentation*, 6(01):C01069, 2011.

[120] E. Price. *International tables for crystallography volume C: Mathematical, physical and chemical tables.* Springer Netherlands, 2004.

[121] G. Rabilloud. *High-Performance Polymer.* Editions Technip, 1999.

[122] E.H. Rhoderick and R.H. Williams. *Metal-semiconductor contacts.* Monographs in electrical and electronic engineering. Clarendon Press, 1988.

[123] T. Rieger, M. Luysberg, T. Schäpers, D. Grützmacher, and M.I . Lepsa. Molecular beam epitaxy growth of GaAs/InAs core-shell nanowires and fabrication of InAs nanotubes. *Nano letters*, 12(11):5559, 2012.

[124] L. Rigutti, G. Jacopin, L. Largeau, E. Galopin, A. De Luna Bugallo, F. H. Julien, J.-C. Harmand, F. Glas, and M. Tchernycheva. Correlation of optical and structural properties of GaN/AlN core-shell nanowires. *Phys. Rev. B*, 83:155320, 2011.

[125] I. Robinson. Nanoparticle structure by coherent x-ray diffraction. *Journal of the Physical Society of Japan*, 82(2):021012, 2013.

[126] I. K. Robinson. Crystal truncation rods and surface roughness. *Phys. Rev. B*, 33:3830, 1986.

[127] A. Rose. Space-charge-limited currents in solids. *Phys. Rev.*, 97:1538, 1955.

[128] H. D. Rudolph, K. Walzer, and I. Krutzik. Microwave spectrum, barrier for methyl rotation, methyl conformation, and dipole moment of ortho-xylene. *Journal of Molecular Spectroscopy*, 47:314, 1973.

[129] B. Rupp. Calculation of atomic scattering factors, http://www.ruppweb.org/Xray/comp/scatfac.htm, 2014.

[130] T. Scheler, M. Rodrigues, T. W. Cornelius, C. Mocuta, A. Malachias, Magalh aes Paniago, F. Comin, J. Chevrier, and T. H. Metzger. Probing the elastic properties of individual nanostructures by combining in situ atomic force microscopy and micro-x-ray diffraction. *Applied Physics Letters*, 94(2):023109, 2009.

[131] V. Schmidt, J. V. Wittemann, S. Senz, and U. Gösele. Silicon nanowires: A review on aspects of their growth and their electrical properties. *Advanced Materials*, 21(25-26):2681, 2009.

[132] A. D. Schricker, F. M. Davidson III, R. J. Wiacek, and B. A. Korgel. Space charge limited currents and trap concentrations in GaAs nanowires. *Nanotechnology*, 17(10):2681, 2006.

[133] R. Schwödiauer, G. S. Neugschwandtner, S. Bauer-Gogonea, S. Bauer, and W. Wirges. Low-dielectric-constant cross-linking polymers: Film electrets with excellent charge stability. *Applied Physics Letters*, 75(25):3998, 1999.

[134] J. Segura-Ruiz, G. Martínez-Criado, C. Denker, J. Malindretos, and A. Rizzi. Phase Separation in Single InxGa1–xN Nanowires Revealed through a Hard X-ray Synchrotron Nanoprobe. *Nano Letters*, 14(3):1300, 2014.

[135] G. Signorello, E. Lörtscher, P. A. Khomyakov, S. Karg, D. L. Dheeraj, B. Gotsmann, H. Weman, and H. Riel. Inducing a direct-to-pseudodirect bandgap transition in wurtzite GaAs nanowires with uniaxial stress. *Nat Commun*, 5:3655, 2014.

[136] M. Soini, I. Zardo, E. Uccelli, S. Funk, G. Koblmüller, A. Fontcuberta i Morral, and G. Abstreiter. Thermal conductivity of GaAs nanowires studied by micro-Raman spectroscopy combined with laser heating. *Applied Physics Letters*, 97(26):263107, 2010.

[137] I. P. Soshnikov, D. E. Afanas'Ev, V. A. Petrov, G. E. Cirlin, A. D. Bouravlev, Y. B. Samsonenko, A. Khrebtov, E. M. Tanklevskaya, and I. A. Seleznev. Piezoelectric effect in GaAs nanowires. *Semiconductors*, 45:1082, 2011.

[138] D. Spirkoska, J. Arbiol, A. Gustafsson, S. Conesa-Boj, F. Glas, I. Zardo, M. Heigoldt, M. H. Gass, A. L. Bleloch, S. Estrade, M. Kaniber, J. Rossler, F. Peiro, J. R. Morante, G. Abstreiter, L. Samuelson, and A. Fontcuberta i Morral. Structural and optical properties of high quality zinc-blende/wurtzite GaAs nanowire heterostructures. *Phys. Rev. B*, 80:245325, 2009.

[139] J. Stangl, C. Mocuta, V. Chamard, and D. Carbone. *Nanobeam X-Ray Scattering: Probing Matter at the Nanoscale*. Wiley, 2013.

[140] S.M. Sze and K.K. Ng. *Physics of Semiconductor Devices*. Wiley, 2006.

[141] H. Takato, K. Sunouchi, N. Okabe, A. Nitayama, K. Hieda, F. Horiguchi, and F. Masuoka. Impact of surrounding gate transistor (SGT) for ultra-high-density LSI's. *Electron Devices, IEEE Transactions on*, 38(3):573, 1991.

[142] A. A. Talin, F. Léonard, B. S. Swartzentruber, X. Wang, and S. D. Hersee. Unusually strong space-charge-limited current in thin wires. *Phys. Rev. Lett.*, 101:076802, 2008.

[143] A. A. Talin, F. Léonard, A. M. Katzenmeyer, B. S. Swartzentruber, S. T. Picraux, M. E. Toimil-Molares, J. G. Cederberg, X. Wang, S. D. Hersee, and A. Rishinaramangalum. Transport characterization in nanowires using an electrical nanoprobe. *Semiconductor Science and Technology*, 25(2):024015, 2010.

[144] C. Thelander, P. Caroff, S. Plissard, A. W. Dey, and K. A. Dick. Effects of Crystal Phase Mixing on the Electrical Properties of InAs Nanowires. *Nano Letters*, 11(6):2424, 2011.

[145] R. Timm, O. Persson, D. L. J. Engberg, A. Fian, J. L. Webb, J. Wallentin, A. Jönsson, M. T. Borgström, L. Samuelson, and A. Mikkelsen. Current–Voltage characterization of individual as-grown nanowires using a Scanning Tunneling Microscope. *Nano Letters*, 13(11):5182, 2013.

[146] K. Tomioka, M. Yoshimura, and T. Fukui. A III-V nanowire channel on silicon for high-performance vertical transistors. *Nature*, 488:189, 2012.

[147] J.Y. Tsao. *Materials Fundamentals of Molecular Beam Epitaxy.* Elsevier Science, 1993.

[148] N. Venant, A. Niguès, F. Marchi, M. Hrouzek, F. Comin, J.l Chevrier, and J.-L. Florens. Multi-sensorial interface for 3d teleoperations at micro and nanoscale. In A. M.L. Kappers, J.B.F. van Erp, W.M. Bergmann Tiest, and F.C.T. van der Helm, editors, *Haptics: generating and perceiving tangible sensations*, volume 6191 of *Lecture notes in computer science*, page 35. Springer Berlin Heidelberg, 2010.

[149] R. S. Wagner and W. C. Ellis. Vapor-liquid-solid mechanism of single crystal growth. *Appl. Phys. Lett.*, 4:89, 1964.

[150] Y. Wang. *Extraordinary Electro- and Opto- Conductance in III-V Semiconductor Metal Hybrid Structures.* Washington University in St. Louis, 2008.

[151] Z. L. Wang, R. P. Gao, Z. W. Pan, and Z. R. Dai. Nano-scale mechanics of nanotubes, nanowires, and nanobelts. *Advanced Engineering Materials*, 3(9):657, 2001.

[152] B. E. Warren. *X-ray diffraction.* Dover Publication Inc., 1990.

[153] R. Wiesendanger. *Scanning Probe Microscopy and Spectroscopy.* Cambridge University Press, 1994.

[154] M. Woehrmann and M. Toepper. *Polymerization of Thin Film Polymers, New Polymers for Special Applications.* InTech, 2012.

[155] P. Yang, R. Yan, and M. Fardy. Semiconductor nanowire: What's next? *Nano Letters*, 10(5):1529, 2010.

[156] M. Yao, N. Huang, S. Cong, C.-Y. Chi, M. A. Seyedi, Y.-T. Lin, Y. Cao, M. L. Povinelli, P. D.l Dapkus, and C. Zhou. GaAs nanowire array solar cells with axial p–i–n junctions. *Nano Letters*, 14(6):3293, 2014.

[157] S. Yazji, I. Zardo, M. Soini, P. Postorino, A. Fontcuberta i Morral, and G. Abstreiter. Local modification of GaAs nanowires induced by laser heating. *Nanotechnology*, 22(32):325701, 2011.

[158] C.-Y. Yeh, Z. W. Lu, S. Froyen, and A. Zunger. Zinc-blende-wurtzite polytypism in semiconductors. *Phys. Rev. B*, 46:10086, 1992.

[159] Z. Zhang, K. Yao, Y. Liu, C. Jin, X. Liang, Q. Chen, and L.-M. Peng. Quantitative analysis of current–voltage characteristics of semiconducting nanowires: Decoupling of contact effects. *Advanced Functional Materials*, 17(14):2478, 2007.

[160] J.F. Ziegler, J.P. Biersack, and U. Littmark. *The stopping and range of ions in solids*. 1985.

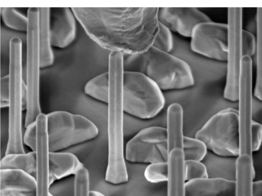

Acknowledgements

The work presented is the result of an international collaboration between the University of Siegen (in Germany) and the ESRF (in France); and originated as a project between my academic supervisor Prof. Ullrich Pietsch, head of the Solid State Physics group at the University of Siegen, and my co-supervisor Dr. Tobias Schülli, beamline scientist in charge at ID01 at the ESRF. I am grateful to both of them for offering me the valuable opportunity to carry out this research.

First of all, I would like to thank Prof. Pietsch for his support and his guidance. He supervised my work constantly, giving me at the same time the necessary freedom to develop my own working rhythm, leading to the successful outcomes presented here. His taste for discovery and his ambitious view towards science have been models of inspiration to me throughout these years.

I would also like to thank Dr. Schülli: his spirit of innovation and his competitive approach played a crucial role in my scientific development. He was the first to introduce me to the experimental sphere of the beamline and to reveal to me the great potential of n-XRD.

Beyond my two supervisors, many other scientists and colleagues contributed to my research: I would like to express my gratitude to all of them. Here, I list some of them, grouped according to their division, institute and/or university.

Solid State Physics group at the University of Siegen (Germany). I would like to thank Dr. Andreas Biermanns-Föth, who shared with me his experimental talents and knowledge. His advices on the treatment, analysis and interpretation of data have been extremely useful. *Vielen Dank* Andreas, for teaching me literally *how to find my way in reciprocal space.* Many

thanks as well to a good friend and colleague, Dr. Anton Davydok, now at IM2NP in Marseille (France), who gave me helpful hints during the first years of my research. Many thanks to Dr. Semën Gorfman and Mohammed Al Taani, for their introduction to the field of piezoelectricity from theoretical and experimental points of view. Many thanks to Arman Davtyan and Hyeok-min Choe who took part in my beamtimes in 2012 and 2013. I would like to thank Eduard Mikayelyan, Dr. Souren Grigorian, Dr. Behnam Khanbabaee, and all the other group members, whose friendship has been an honour for me during my stays in Siegen.

ESRF, Grenoble (France). Many thanks to the former and present members of beamline ID01: Dr. Vincent Jacques, Dr. Francesca Mastropietro, Dr. Jan Hilhorst, Dr. Peter Boesecke, Dr. Gilbert Chahine, Dr. Marta Elzo-Aizarna and Dr. Marie-Ingrid Richard. *Un grand merci* to Hamid Djazouli, who took great care of the experimental station, providing for all of us fully efficient experimental conditions. A heartfelt *grazie!* to Dr. Dina Carbone, initially my 'co-co-supervisor' and now at MAX IV in Lund (Sweden), whose guidance and fruitful advice, in terms of data analysis, physical interpretation and work organization, have been indispensable throughout my scientific experience. Many thanks to Dr. Thomas Cornelius (now at IM2NP in Marseille) and Dr. Joël Eymery (from CEA Grenoble), for their advice about sample preparation. I am also grateful to Dr. Harald Müller and Dr. Irina Snigireva from the Chemistry and Microimaging Laboratory; and to Dr. Mario Rodrigues, Anthony Vial, Dr. Luca Costa and Dr. Fabio Comin from the Science Surface Laboratory (SSL): their support and teaching have been essential in orienting my first steps in the world of AFM.

Thanks as well to my dear friend Dr. Tamzin Lafford, who cross-checked and refined the English content of all my manuscripts. She has written a *Simple Guide to Writing and Presenting in English*, which can be found in ref. [84].

University of Bochum and Paul Drude Institute (PDI) in Berlin (Germany). I would like to thank Rüdiger Schott, Dr. Dirk Reuter and Prof. Andreas Wieck from the University of Bochum, and Dr. Emmanouil Dimakis, Dr. Abbes Tahraoui, Dr. Claudio Somaschini and Dr. Lutz Geelhaar from the PDI, for the growth and preparation of the nanowire samples and for their help in the interpretation of the results.

Lehrstuhl Höchstfrequenztechnik und Quantenelektronik at the University of Siegen (Germany). Many thanks to Dr. Heiko Schäfer-Eberwein: his outstanding experience with the FIB-SEM equipment and his great teaching capability made it possible for me to measure the electrical characteristics of single nanostructures. Many thanks as well to Daniel Stock for his contribution in the treatment of the data and to Prof. Peter Haring Bolívar for his support and his help with the interpretation of the results.

Synchrotron Radiation Research division at the University of Lund (Sweden). Many thanks to Dr. Rainer Timm, Olof Persson and Prof. Anders Mikkelsen, for welcoming me to Lund and showing me the potential of the STM and X-ray Photoemission Spectroscopy (XPS) systems available in their group and at beamline I311 at the MAX II synchrotron.

Electronics group of the Physics department at the University of Siegen (Germany). Many thanks to Stefan Heidbrink, Marco Vogt, and Dr. Michael Ziolkowski for their help with the electrical contact of the polymer-embedded nanowires.

Beamline I07 at the Diamond synchrotron (UK) and beamline P08 at Petra III in Hamburg (Germany). Many thanks to Dr. Chris Nicklin (Diamond), Dr. Oliver Seeck (Petra III) and all the beamline staff for their support during beamtime.

Finally, I would like to thank my husband Raphael for his constant scientific support, his encouragement and his precious love.

This research was supported partially by the ESRF and by the Deutsche Forschungsgemeinschaft (DFG) under contracts Pi217/38 and Ge2224/2.